Time-Resolved Diffraction Studies of Structural Dynamics in Solids

Wang, Xiaocui

2019

Document Version:
Publisher's PDF, also known as Version of record

Time-Resolved Diffraction Studies of Structural Dynamics in Solids

XIAOCUI WANG
FACULTY OF ENGINEERING | LUND UNIVERSITY

Time-Resolved Diffraction Studies of Structural Dynamics in Solids

Time-Resolved Diffraction Studies of Structural Dynamics in Solids

Xiaocui Wang

LUND
UNIVERSITY

Thesis for the degree of Doctor of Philosophy
Thesis advisors: Prof. Jörgen Larsson, Dr. Henrik Enquist
Faculty opponent: Dr. Marco Cammarata

To be presented, with the permission of the Faculty of Engineering, LTH of Lund University, for public criticism in Rydberg lecture hall (Rydbergsalen) at the Department of Physics on Wednesday, the 12th of June 2019 at 09:15.

Organization
LUND UNIVERSITY

Division of Atomic Physics
Department of Physics
P.O. Box 118
SE-221 00 Lund, Sweden

Author
Xiaocui Wang

Document name
DOCTORAL DISSERTATION

Date of disputation
2019-06-12

Sponsoring organization

Title and subtitle
Time-Resolved Diffraction Studies of Structural Dynamics in Solids

Abstract
Studies of the structural dynamics of solids can improve our understanding of atomic motion in materials, and may thus help in the manufacture of new devices or the development of materials with novel structures and properties. Ultrashort laser pulses, a few tens of femtoseconds long, can deliver high energies (mJ–kJ). This energy is absorbed by the electrons in a solid material, leading to a rapid increase in the electron temperature within the duration of the laser pulse. The energy will then be transferred to the crystal lattice, resulting in an increase in the lattice temperature, which triggers lattice motion such as vibrations (phonons) and disordering (melting of solids). The distance between neighboring atoms in solids is on the order of 10^{-10} m (Ångström). Since the wavelength of X-rays is in the range of nanometers to Ångströms, which is of the same order as the interatomic distances in solids, X-rays can be used to detect structural changes in solids. The structural dynamics in solids can then be monitored as a function of time by combining ultrashort laser pulses with X-ray techniques.

This thesis focuses on the structural dynamics of solids on the time scale of femtoseconds to picoseconds. The studies described in this thesis were divided into two categories based on the laser excitation fluence: below the damage threshold of the sample, and above the damage threshold of the sample. The electron diffusion in a Ni film was studied at fluences below the damage threshold, using a Ni/InSb photo-acoustic transducer. An X-ray switch based on a Au/InSb photo-acoustic transducer was designed and tested as part of the commissioning of the FemtoMAX beamline at the MAX IV Laboratory in Lund. Using fluences above the damage threshold, pressure waves were generated in an Al/InSb photo-acoustic transducer due to the melting of the Al film. The pressure waves were probed and characterized in the InSb substrate. The pressure was in the region of the phase diagram where phase transition could occur. Pressure waves with a similar amplitude were also generated and characterized in graphite. Non-thermal melting was also studied in InSb at fluences above the damage threshold.

The findings presented in this thesis contribute to both applications of physics for the manufacture of new devices, and to fundamental physics, by improving our understanding of hydrodynamic pressure waves and phase transitions. The study involving the Ni/InSb photo-acoustic transducer demonstrated an alternative method of characterizing the basic physical properties of a metallic film, while the Au/InSb switch provides a potential means of generating short X-ray pulses at storage rings. The characterization of the pressure waves in the Al/InSb photo-acoustic transducer and graphite extend the current knowledge on the generation of short pressure pulses in solids on the picosecond time scale, which attracts more attention to understand the phase transition process on the ultrafast time scale. The study of non-thermal melting provided new approaches for timing diagnostics at free-electron laser facilities.

Key words:
Time-resolved X-ray diffraction, phonons, photo-acoustic transducer, electron diffusion, pressure wave, non-thermal melting

Classification system and/or index terms (if any)
43.38.Zp, 61.10.−i, 61.82.Fk, 62.50.+p, 63.20.−e, 64.60.−i

Supplementary bibliographical information

Language
English

ISSN and key title
ISSN 0281-2762, Lund Reports on Atomic Physics, LRAP-558

ISBN
978-91-7895-125-3 (print)
978-91-7895-126-0 (pdf)

Recipient's notes

Number of pages
145

Price

Security classification

Signature: Xiaocui Wang Date: 2019-05-02

Time-Resolved Diffraction Studies of Structural Dynamics in Solids

Xiaocui Wang

LUND
UNIVERSITY

TIME-RESOLVED DIFFRACTION STUDIES OF STRUCTURAL DYNAMICS IN SOLIDS

Funding information: This project has received funding from the European Union's Horizon 2020 research and innovation program under the Marie Skłodowska-Curie grant agreement No. 637295.

Division of Atomic Physics
Department of Physics
Faculty of Engineering, LTH
Lund University

Lund Reports on Atomic Physics, LRAP 558 (2019)

ISBN: 978-91-7895-125-3 (print)
ISBN: 978-91-7895-126-0 (pdf)
ISSN: 0281-2762

Printed in Sweden by Media-Tryck, Lund University, Lund 2019

Dedicated to my family

献给我的家人

Contents

Abstract

Studies of the structural dynamics of solids can improve our understanding of atomic motion in materials, and may thus help in the manufacture of new devices or the development of materials with novel structures and properties. Ultrashort laser pulses, a few tens of femtoseconds long, can deliver high energies (mJ–kJ). This energy is absorbed by the electrons in a solid material, leading to a rapid increase in the electron temperature within the duration of the laser pulse. The energy will then be transferred to the crystal lattice, resulting in an increase in the lattice temperature, which triggers lattice motion such as vibrations (phonons) and disordering (melting of solids). The distance between neighboring atoms in solids is on the order of 10^{-10} m (Ångström). Since the wavelength of X-rays is in the range of nanometers to Ångströms, which is of the same order as the interatomic distances in solids, X-rays can be used to detect structural changes in solids. The structural dynamics in solids can then be monitored as a function of time by combining ultrashort laser pulses with X-ray techniques.

This thesis focuses on the structural dynamics of solids on the time scale of femtoseconds to picoseconds. The studies described in this thesis were divided into two categories based on the laser excitation fluence: below the damage threshold of the sample, and above the damage threshold of the sample. The electron diffusion in a Ni film was studied at fluences below the damage threshold, using a Ni/InSb photo-acoustic transducer. An X-ray switch based on a Au/InSb photo-acoustic transducer was designed and tested as part of the commissioning of the FemtoMAX beamline at the MAX IV Laboratory in Lund. Using fluences above the damage threshold, pressure waves were generated in an Al/InSb photo-acoustic transducer due to the melting of the Al film. The pressure waves were probed and characterized in the InSb substrate. The pressure was in the region of the phase diagram where phase transition could occur. Pressure waves with a similar amplitude were also generated and characterized in graphite. Non-thermal melting was also studied in InSb at fluences above the damage threshold.

The findings presented in this thesis contribute to both applications of physics for the manufacture of new devices, and to fundamental physics, by improving our understanding of hydrodynamic pressure waves and phase transitions. The study involving the Ni/InSb photo-acoustic transducer demonstrated an alternative method of characterizing the basic physical properties of a metallic film, while the Au/InSb switch provides a potential means of generating short X-ray pulses at storage rings. The characterization of the pressure waves in the Al/InSb photo-acoustic transducer and graphite extend the current knowledge on the generation of short pressure pulses in solids on the picosecond time scale, which attracts more attention to understand

the phase transition process on the ultrafast time scale. The study of non-thermal melting provided new approaches for timing diagnostics at free-electron laser facilities.

Popular Scientific Summary

Our curiosity about the world in which we live, and the universe surrounding it, has inspired the development of new techniques and the discovery of new phenomena. We use telescopes to observe the stars, and microscopes to see cells, while moving objects are captured using cameras. In the work described in this thesis, techniques have been used to investigate the structural dynamics of solids on the atomic scale ($\sim 10^{-10}$ m), during very short times ($\sim 10^{-15}$ s). This can be compared with taking pictures of very small objects with a very fast shutter speed.

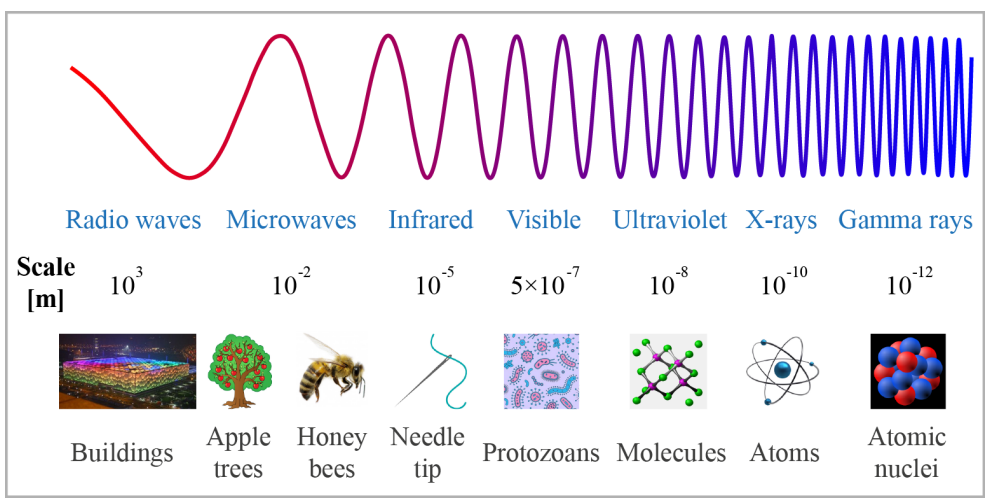

Illustration of the electromagnetic spectrum, and objects with corresponding dimensions.

To measure the physical length of an object, we use a ruler with a scale of the same order of magnitude as the object. For example, we can use a meter ruler to measure the dimensions of a table, but we cannot use the same ruler to measure the diameter of a human hair. An instrument capable of measurements on a smaller scale, such as a microscope, must be used to measure the thickness of hair, which is about 100 micrometers. In classical physics, all matter, including solids, liquids and gases, consists of atoms. The atoms in solids are arranged uniformly, and the distance between them is on the order of Ångström, which is 10^{-10} m. The ratio between 1 Ångström and 1 m is like the ratio between the thickness of a mobile phone ($\sim$4 mm) and the circumference of the earth at the equator ($\sim$40 000 km). To study the motion

of atoms in solids, an instrument is needed that has the same scale as the interatomic distance. From the illustration of the electromagnetic spectrum above, it can be seen that the wavelength of X-rays is on the scale of Ångstroms. This makes X-rays an excellent tool for studying the motion of atoms in solids. The X-rays scattered from the atoms in a solid will interfere with each other if the difference in their propagation path is equal to a multiple of the X-ray wavelength. This means that the uniform arrangement of atoms in solids can give rise to an X-ray scattering pattern.

The advent of digital cameras has allowed us to take good photographs of moving objects. However, it is still impossible to capture the movement of an object if it is moving faster than the shutter speed of the camera, regardless of how well the focus of the camera is adjusted. The shutter speed of mobile phone cameras is nowadays about a few milliseconds (10^{-3} s). As mentioned above, the distance between neighboring atoms is a few Ångströms, and the velocity of the atoms in solids at room temperature is usually on the order of few Ångströms per picosecond (10^{-12} s), which is equivalent to a few hundred meters per second. The time taken for atoms to move a few Ångströms can be estimated to be a few hundred femtoseconds (10^{-15} s), so none of the cameras available today, not even high-speed specialized cameras, can capture the motion of atoms. Since the wavelength of X-rays is similar to the distance between neighboring atoms, ultrashort X-ray pulses can be used to study atomic motion in solids on an ultrafast time scale.

The work described in this thesis was focused on studying ultrafast structural changes in solids. At a given temperature, for example, room temperature, the atoms in solids vibrate around their equilibrium positions. A change in the structure of solids can be induced by giving the atoms extra energy, so that they deviate from their equilibrium positions. During the last few decades, laser techniques have been developed allowing pulses to be generated on the femtosecond time scale. The most commonly used femtosecond laser system is the Ti:sapphire laser. In this work, a Ti:sapphire laser was used to provide the ultrashort pulses triggering structural changes in solids. Since the laser pulses deliver extra energy to the atoms, they will have greater vibrational amplitude than when they are at thermal equilibrium. The different vibrational modes of the atoms in solids are called phonons, and the materials retain their solid form. If the atoms gain higher energy, they will deviate significantly from their equilibrium position, and the bonds between them can be broken, or new bonds can be formed. In this case, the material will undergo a phase change, such as a solid–solid phase transition or a solid–liquid phase transition, normally called melting.

科普总结

基于对我们所生活的世界和周围宇宙的好奇心，人类不断地被启发并由此发展新的技术发现新的现象。例如，我们发明望远镜来观察宇宙中的星星，发明显微镜来观察细胞，发明相机给运动的物体照相。这篇论文工作使用前沿技术在原子尺度上（$\sim 10^{-10}$米）探讨了极短时间内（$\sim 10^{-15}$秒）发生的固体结构动力学现象。这就像是用很短的快门时间给很小的物体照相。

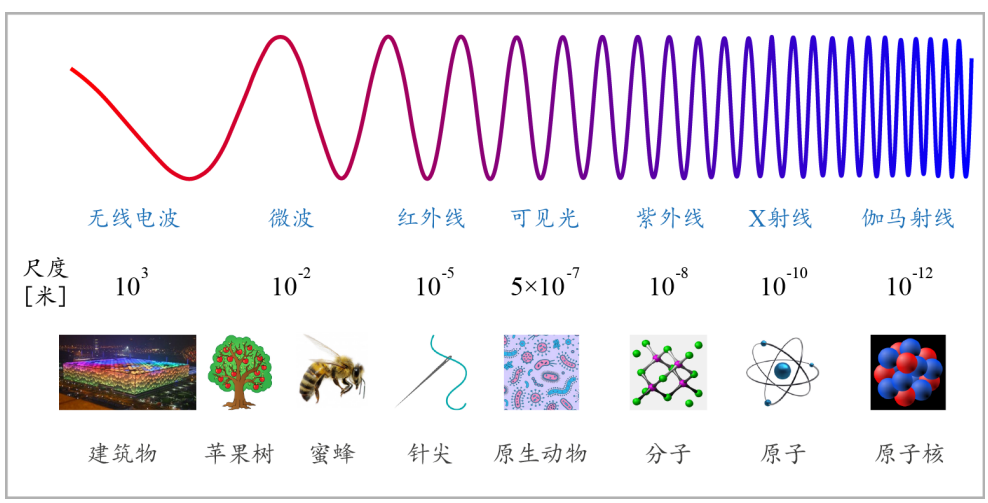

电磁波谱和相应尺度的物体。

为了测量一个物体的长度，我们需要一把具有与这个物体相似尺度的尺子。比如，我们可以用一把米尺去测量一个桌子的尺寸，但是我们不能用同样的米尺来测量头发的直径。由于头发的直径大约是100微米，因此我们需要一台可以在更小的尺度上进行测量的仪器，比如显微镜。在传统的物理图像中，固体液体和气体这些物质是由原子组成的。固体中的原子整齐地排列在一起，原子之间的距离在埃数量级上，也就是10^{-10}米。一埃和一米的比例就像是一部手机的厚度（$\sim$4毫米）和地球在赤道位置的周长（$\sim$40000千米）的比例。为了研究固体中原子的运动，我们需要一个具有和原子间距相同尺度的工具。从电磁波谱上我们可以发现X射线的波长是在埃数量级上。这使得X射线成为研究固体中原子运动的极好工具。如果固体中每个原子散射的X射线的传播路径差等于X射线波长的整数倍，那么这些散射的X射线就会相干叠加。这就意味着固体中整齐排列的原子可以产生X射线散射图案。

数码相机的发明使得我们可以给运动的物体拍摄高质量的照片。然而，无论相机聚焦得如何完美，我们依然无法记录物体在短于相机快门时间内的位移。如今，手机相机的快门时间通常是几毫秒（10^{-3}秒）。之前我们提到，相邻原子之间的距离是几埃。在室温下固体中原子的速度通常是每皮秒（10^{-12}秒）几埃，相当于每秒几百米。由此，我们可以估算出原子移动几埃所需的时间是几百飞秒（10^{-15}秒）。现如今，包括高速专业相机在内，没有相机可以在如此短的时间内记录原子的运动。由于X射线的波长和固体中相邻原子的间距相似，因此我们可以使用超短X射线脉冲在超快时间尺度上研究固体中原子的运动。

这篇论文工作的要点是研究固体中超快的结构变化。在给定的温度环境中（比如室温），固体中的原子在它们的平衡位置附近振动。如果这些原子获得额外的能量，那么它们将偏离平衡位置，从而引发固体的结构变化。在过去的几十年里，激光领域的巨大发展使产生飞秒激光脉冲成为可能。其中最为广泛使用的激光系统是钛宝石激光器。在这篇论文提到的工作中，钛宝石激光器提供了激发固体结构变化的超短激光脉冲。由于激光脉冲给固体材料提供了额外的能量，因此固体中原子的振动幅度比它们在热平衡状态下的振动幅度要大。固体中原子的不同振动模式被称为声子，在这种情形下材料依然保持它们的固体形态。如果固体中的原子获得足够大的能量，它们将会明显偏离平衡位置，从而可能导致原子间的化学键断裂或者新的化学键形成。在这种情形下，材料会发生相变，例如固体–固体相变或者固体–液体相变（熔化）。

List of Publications

This thesis is based on the following publications:

I **FemtoMAX – an X-ray beamline for structural dynamics at the short-pulse facility of MAX IV**

Henrik Enquist, Andrius Jurgilaitis, Amelie Jarnac, Åsa U. J. Bengtsson, Matthias Burza, Francesca Curbis, Christian Disch, J. Carl Ekström, Maher Harb, Lennart Isaksson, Marija Kotur, David Kroon, Filip Lindau, Erik Mansten, Jesper Nygaard, Anna I. H. Persson, Van Thai Pham, Michael Rissi, Sara Thorin, Chien-Ming Tu, Erik Wallén, Xiaocui Wang, Sverker Werin, Jörgen Larsson

J. Synchrotron Rad. **25**, 570–579 (2018)

II **Studies of electron diffusion in photo-excited Ni using time-resolved X-ray diffraction**

A. I. H. Persson, A. Jarnac, Xiaocui Wang, H. Enquist, A. Jurgilaitis, J. Larsson

Appl. Phys. Lett. **109**, 203115 (2016)

III **Communication: Demonstration of a 20 ps X-ray switch based on a photoacoustic transducer**

A. Jarnac, Xiaocui Wang, Å. U. J. Bengtsson, J. C. Ekström, H. Enquist, A. Jurgilaitis, D. Kroon, A. I. H. Persson, V.-T. Pham, C. M. Tu, J. Larsson

Struct. Dyn. **4**, 051102 (2017)

IV **Stabilizing a high-pressure phase in InSb at ambient conditions with a laser-driven pressure pulse**

A. Jarnac, Xiaocui Wang, Å. U. J. Bengtsson, M. Burza, J. C. Ekström, H. Enquist, A. Jurgilaitis, N. Kretzschmar, A. I. H. Persson, C. M. Tu, M. Wulff, F. Dorchies, J. Larsson
manuscript in preparation.

V **Generation of a large compressive strain wave in graphite by ultrashort-pulse laser irradiation**

Xiaocui Wang, A. Jarnac, J. C. Ekström, Å. U. J. Bengtsson, F. Dorchies, H. Enquist, A. Jurgilaitis, M. N. Pedersen, C. -M. Tu, M. Wulff, J. Larsson
Struct. Dyn. **6**, 024501 (2019)

Abbreviations

CPA	Chirped Pulse Amplification
FEL	Free-Electron Laser
FWHM	Full Width at Half Maximum
GIXS	Grazing Incidence X-ray Scattering
ID	Insertion Device
InSb	Indium Antimonide
IR	Infrared
LCLS	Linac Coherent Light Source
MCP	Microchannel plate
RF	Radio Frequency
SPPS	Sub-Picosecond Pulse Source
TRED	Time-Resolved Electron Diffraction
TRXD	Time-Resolved X-ray Diffraction
UV	Ultraviolet

Part I

Overview

Chapter 1

Introduction

The development of mode-locked lasers [1] and chirped pulse amplification (CPA) [2] has allowed bursts of light to be produced with pulse energies up to a few kJ, and a duration of femtoseconds [3]. Excitation with short, highly intense laser pulses can lead to extreme states of matter [4]. Probing the evolution of these extreme states will extend our knowledge concerning the fundamental processes taking place in materials [5]. Structural probes, like X-rays with a wavelength similar to the interatomic distance in materials, can be used to image atomic motion in real time [6–8].

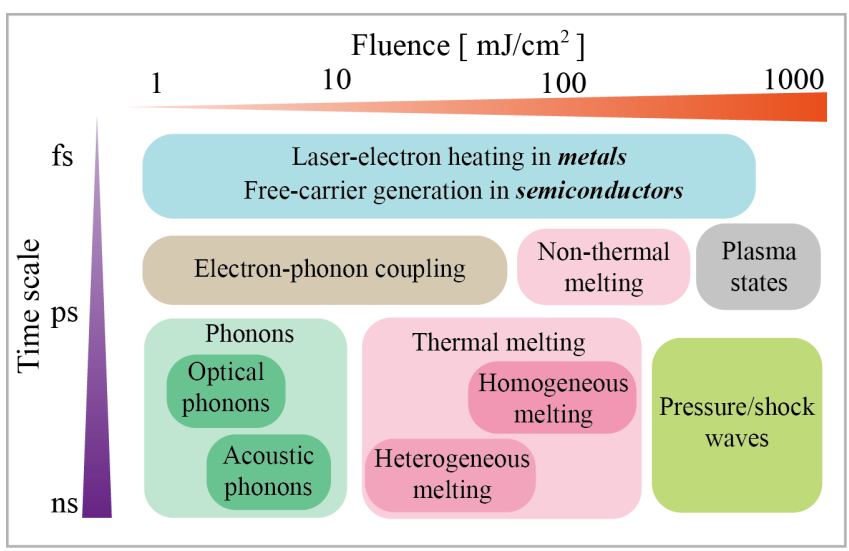

Figure 1.1: Typical time scales and fluence ranges of the dynamics in solids after ultrashort laser excitation.

This thesis focuses on the structural dynamics in solids, i.e., the atomic motion of the crystal lattice. Figure 1.1 shows the typical time scale and the laser excitation fluence required to elicit ultrafast structural dynamics in solids. In this thesis, the term "fluence", expressed as the energy per unit area (mJ/cm^2), is used to describe

the strength of the laser excitation. Upon laser excitation, the energy of the laser radiation will be absorbed by electrons in the solid, resulting in electron heating in metals, and electron-hole generation in semiconductors. The excitation process generally takes place within the duration of the laser pulse. Carrier-carrier scattering causes a Fermi distribution to be established in the electron system on the order of tens of femtoseconds [4, 5].

In the low-fluence regime (a few mJ/cm^2), the energy absorbed by the electrons will be transferred to the lattice via electron-phonon coupling, and thus excite various phonon modes [9–12]. Optical phonons involve concerted atomic motion within a unit cell, whereas acoustic phonons involve motion in which adjacent unit cells move in phase. The frequency of optical phonons is on the order of THz, which corresponds to a period of a few hundred femtoseconds to a few picoseconds. Due to the coherent motion of atoms, the period of acoustic phonons is longer than that of optical phonons, especially for those that are close to the center of the Brillouin zone [13].

Increasing the laser excitation fluence will lead to excessive energy being delivered to the lattice system, which will elevate the lattice temperature, causing melting in solids. Since this melting process is caused by the heating of the lattice, it is called thermal melting, which includes heterogeneous melting and homogeneous melting [14–17]. If the density of laser-excited carriers reaches 10% or more, the potential energy surface of the lattice will be significantly perturbed, which can induce bond softening and atomic disordering [18, 19]. This process takes place on the femtosecond time scale, and is called non-thermal melting, since there is no lattice heating on this fast time scale. In the extreme-high-fluence regime ($>$ few hundreds of mJ/cm^2), the ultrashort laser pulses will create plasma states, leading to the development of pressure/shock waves on the picosecond time scale.

Since the wavelength of X-rays is of the same order as the interatomic distance (a few Ångströms), time-resolved X-ray diffraction (TRXD) is commonly used to directly visualize atomic-scale motion in solids [7, 8]. The development of various X-ray sources (laser plasma sources, storage rings and free-electron lasers) offers the opportunity to study structural dynamics with a time resolution as short as tens of femtoseconds.

1.1 Aims of the work

The aim of the work presented in this thesis was to study the ultrafast structural dynamics that take place on the time scale from hundreds of femtoseconds to hundreds of picoseconds using TRXD, including phonon dynamics, pressure waves and non-thermal melting. The study of these dynamic processes will improve our understanding of fundamental processes in matter, such as electron-phonon coupling and phase transitions.

The work carried out during commissioning of the FemtoMAX beamline at the MAX IV Laboratory in Lund is presented in Paper I. Two of the experiments included in this thesis were carried out at the FemtoMAX beamline. Paper II describes how electron diffusion in a metallic film (Ni) was studied by analyzing the onset of phonon dynamics. An X-ray switch based on a Au/InSb photo-acoustic transducer, which has the capability to shorten the X-ray pulses generated in synchrotron storage rings, is described in Paper III. Pressure waves were generated in an Al/InSb photo-acoustic transducer and a graphite crystal, and were characterized using TRXD, resulting in

the publication of Paper IV and Paper V. This thesis also presents preliminary results from the non-thermal melting experiment in InSb, and potential applications.

1.2 Structure of this thesis

This thesis includes six chapters. Chapter 2 provides the theory that is relevant to this work, including X-ray scattering and laser-induced structural dynamics in solids. The experimental methods used to study structural dynamics are described in Chapter 3, while the simulation methods are described in Chapter 4. The main results of five experiments are presented in Chapter 5. Chapter 6 provides a summary of the findings, and an outlook on future research.

Chapter 2

Light–Matter Interaction

The theory of light–matter interaction relevant to this work is presented in this chapter. Sections 2.1 and 2.2 discuss the interaction between X-rays and matter, including the basic properties of X-rays and the scattering of X-rays from different objects (a single electron, a single atom, and a crystal). Laser-induced lattice dynamics, such as phonons, pressure waves, and lattice disordering, will be introduced in Section 2.3.

2.1 The basic properties of X-rays

2.1.1 Refractive index

The refractive index of materials to X-ray radiation has a complex form, and is expressed as:

$$n = 1 - \delta - \mathrm{i}\beta \tag{2.1}$$

where δ and β denote the dispersion and absorption, respectively. Here, δ is a small positive number, on the order of 10^{-5}, which means the real part of the refractive index is smaller than 1. The imaginary part, β, is typically on the order of 10^{-8}–10^{-5}. The refractive indices of several materials used in this work are given in Table 2.1.

Table 2.1: Refractive indices of Ni, Au, Al, InSb and graphite at an X-ray photon energy of 6 keV [20].

Refractive index	Ni	Au	Al	InSb	Graphite
δ	4.7×10^{-5}	8.5×10^{-5}	1.5×10^{-5}	2.8×10^{-5}	1.3×10^{-5}
β	1.6×10^{-6}	1.4×10^{-5}	4.9×10^{-7}	4.9×10^{-6}	3.9×10^{-8}

2.1.2 Penetration depth

Due to the small imaginary part of the refractive index, X-rays can penetrate very deep into most materials. The penetration depth of X-rays is significantly greater than that of IR radiation for the materials used in this work. (IR radiation was used as the light source for the laser-induced lattice dynamics described in Section 2.3.) Table 2.2 gives the penetration depths of radiation with photon energies of 1.5 eV and 6 keV. A photon energy of 1.5 eV corresponds to 800 nm radiation (IR). Ti:sapphire lasers with a central wavelength of 800 nm were used to excite the samples in all the experiments presented in this thesis. The photon energies of the X-rays used in these experiments were between 3 keV and 15 keV. The photon energy of 6 keV was used in Table 2.2 as it is the photon energy often used for the comparison of X-ray penetration depths.

Table 2.2: Penetration depths of radiation with different photon energies in the five materials used in this work: Ni, Au, Al, InSb and graphite.

Photon energy	Ni	Au	Al	InSb	Graphite
1.5 eV	13.0 nm[a]	12.2 nm[b]	8.5 nm[b]	91.3 nm[c]	36.2 nm[d]
6 keV	10.5 μm[e]	1.2 μm[e]	33.6 μm[e]	3.4 μm[e]	422.3 μm[e]

[a] Ref. [21].
[b] Ref. [22].
[c] Ref. [23].
[d] Ref. [24].
[e] Ref. [20].

It can be seen from Table 2.2 that the penetration depth of X-rays is generally about three orders of magnitude greater than that of IR radiation. This means that in TRXD experiments in solids, the energy of the laser pulse can only be deposited at the surface of the solid, while the X-rays can probe the dynamics deep into the solid. For example, when exciting a solid with a moderate laser fluence, which is below the damage threshold, the upper layer of the solid will be heated, leading to the generation of acoustic phonons. These acoustic phonons will propagate in the solid at the speed of sound. Since the penetration depth of the X-rays is on the order of μm and the speed of sound in solids is usually a few km per second, this means that such X-rays can be used to probe the transient nature of acoustic phonons during a period of a few hundred ps. Acoustic phonons will be discussed in more detail in Section 2.3.3, and a photo-acoustic transducer, consisting of a metallic film and a semiconductor substrate, will be described in Section 2.3.4. The thickness of the metallic film studied was only tens or hundreds of nm. This means that the energy of the laser pulse will only be absorbed by the metallic film, while the X-rays will easily pass through it without losing too much intensity, and can be used to probe the dynamics in the substrate under the film.

2.1.3 Critical angle and specular reflection

It is known that for an electromagnetic wave in the visible range propagating from a dense medium (n > 1) to vacuum (n = 1), total internal reflection can occur when the angle of incidence is greater than a critical value, called the critical angle. In analogy, for X-rays, when the refractive index n < 1, total external reflection will take place if the incident angle is smaller than the critical angle. According to the convention used in X-ray science, the incident angle is defined as the angle between the X-ray beam and the sample surface. The critical angle can be derived from the refractive index using Snell's law and Taylor expansion.

Snell's law is normally expressed as:

$$\frac{\sin\alpha_1}{\sin\alpha_2} = \frac{n_2}{n_1} \tag{2.2}$$

where α_1, α_2, θ_1 and θ_2 are as illustrated in Figure 2.1, and n_1 and n_2 are the refractive indices of the vacuum and the medium, respectively. In the total external reflection case, $\theta_1 = \theta_c$, where θ_c is the critical angle, and $\theta_2 = 0$. Therefore, $\alpha_1 = \pi/2 - \theta_1 = \pi/2 - \theta_c$ and $\alpha_2 = \pi/2$. Using Eq. 2.1, Eq. 2.2 can be expressed as:

$$\frac{\sin(\frac{\pi}{2} - \theta_c)}{\sin\frac{\pi}{2}} = \frac{1-\delta}{1} \tag{2.3}$$

which gives:

$$\cos\theta_c = 1 - \delta \tag{2.4}$$

Applying Taylor expansion:

$$\cos\theta_c = 1 - \frac{\theta_c^2}{2} + \mathrm{O}(\theta_c^4) \tag{2.5}$$

gives the critical angle [25]:

$$\theta_c \approx \sqrt{2\delta} \tag{2.6}$$

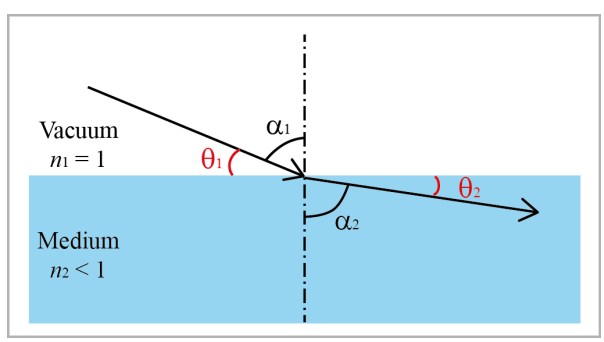

Figure 2.1: Sketch illustrating the geometry used to calculate the critical angle for total external reflection of X-rays.

The critical angle plays an important role in the grazing incidence geometry (see Section 3.1.5), which is generally used to study structural dynamics occurring at the

surface of solids. If the X-ray angle of incidence is less than the critical angle, the X-rays will be reflected by the sample surface, which is called specular reflection. The diffraction efficiency will then be extremely low, since only X-ray evanescent waves enter the sample. Therefore, for grazing incidence geometry, the X-ray angle of incidence should be greater than the critical angle.

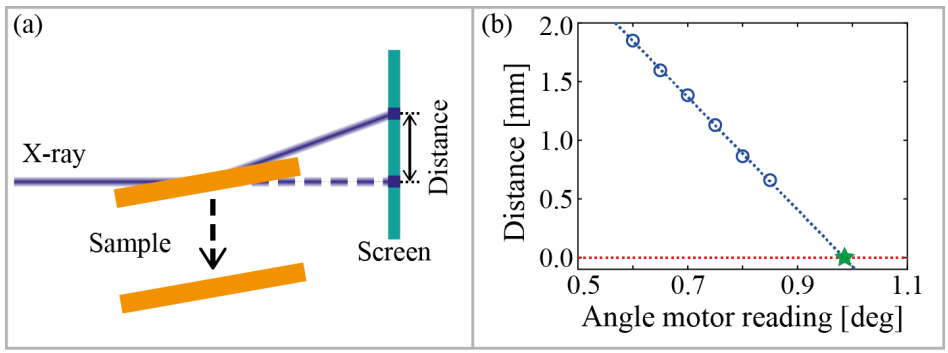

Figure 2.2: (a) Sketch of the experimental setup used for specular reflection measurements. (b) Results of a typical specular reflection measurement. The blue circles represent the measured data points, and the dotted blue line is a linear fit to the experimental data. The green star indicates the angle motor position for the zero angle.

The probing depth changes dramatically with the angle of incidence (as discussed in Section 3.1.4) in grazing incidence geometry. Therefore, the zero angle should be carefully calibrated in order to ensure the correct angle of incidence. Specular reflection can be used to calibrate the angle of incidence of the X-ray beam in the grazing incidence geometry. Figure 2.2(a) illustrates the experimental setup used for specular reflection measurements. The reflected beam or the direct beam can be captured on the screen by moving the sample up or down, and the distance between them can be calculated for a given angle of incidence. The distance will vary as the angle changes with an angle motor. Figure 2.2(b) shows the results of a typical specular reflection measurement. Linear fitting is used to extract the angle motor position for the zero angle, indicated by the green star in Figure 2.2(b).

2.2 X-ray scattering

Time-resolved X-ray diffraction/TRXD was used to probe structural dynamics in different kinds of crystals. X-ray diffraction is a special case of X-ray scattering, in which only elastic scattering is taken into account, and the scattering object is a crystal consisting of atoms, which in turn consist of nuclei surrounded by electrons. X-ray scattering is caused by the interaction between the X-rays and the electrons of the atoms in the crystals. The scattering of X-rays by a single electron, a single atom and by a crystal is discussed in this section.

2.2.1 Scattering by a single electron

The simplest case is the interaction between X-rays and a single electron, as illustrated in Figure 2.3. The electron is located at the origin O, and the electric field at an

observation point P will be derived below. The electric fields of the incident beam and the scattered beam are denoted $\vec{E}_0$ and $\vec{E}$.

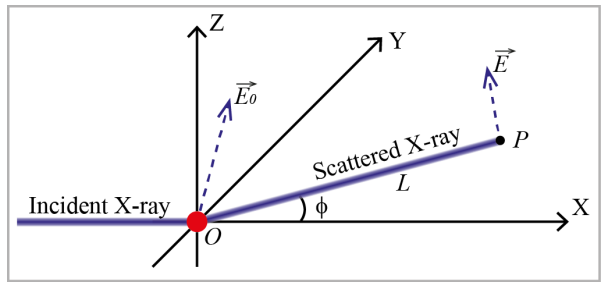

Figure 2.3: X-ray scattering by a single electron.

The relation between the incident beam and the scattered beam is given by [26]:

$$< |\vec{E}|^2 > = < |\vec{E}_0|^2 > \frac{e^4}{m^2c^4L^2} \left(\frac{1 + \cos^2 \phi}{2} \right) \tag{2.7}$$

where e is the elementary charge, m is the electron mass, c is the speed of light, L is the distance between the origin and the observation point, and $(1 + \cos^2 \phi)/2$ is the polarization factor of the scattered beam with respect to the incident beam. L and ϕ are also shown in Figure 2.3.

In practice, the measurable quantity is the elastic scattering intensity, I, which is defined as:

$$I = \frac{c}{8\pi} < |\vec{E}|^2 > \tag{2.8}$$

Therefore, Eq. 2.7 can be expressed in terms of intensity as follows:

$$I = I_0 \frac{e^4}{m^2c^4L^2} \left(\frac{1 + \cos^2 \phi}{2} \right) \tag{2.9}$$

2.2.2 Scattering by a single atom

All atoms in the periodic table, except hydrogen, contain multiple electrons. The scattering of X-rays by a single atom can be obtained by integrating the scattering from all the electrons in an atom [26], which can be written:

$$f(\vec{Q}) = \int_0^\infty \rho(\vec{r}) \exp(\mathrm{i}\vec{Q} \cdot \vec{r}) \, \mathrm{d}\vec{r} \tag{2.10}$$

Here, $f(\vec{Q})$ is the atomic scattering factor including the phase information, which comes from the exponential term in the integral in Eq. 2.10. $\rho(\vec{r})$ is the distribution of the electron density at position $\vec{r}$. $\vec{Q} = \vec{k}_s - \vec{k}_i$ is called the scattering vector or the momentum transfer vector, as illustrated in Figure 2.4. $\vec{k}_s$ and $\vec{k}_i$ represent the wave vectors of the incident beam and the scattered beam, respectively. The atomic scattering factor for the elements in the periodic table can be found in the International Tables for X-ray Crystallography [27].

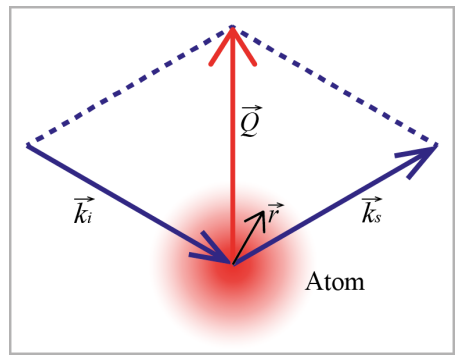

Figure 2.4: X-ray scattering by a single atom.

2.2.3 Crystal structure

When atoms are located in a periodic structure (lattice), they will form a crystal. Figure 2.5 shows a crystal structure in the two-dimensional case. The lattice is generated by discrete translations of the base vectors, as shown by the vectors $\vec{a}_1$ and $\vec{a}_2$ in Figure 2.5. The base vectors ($\vec{a}_1$ and $\vec{a}_2$) and the angle γ_{12} define the smallest repetitive area (volume in the three-dimensional case), which is called the unit cell. Two factors are considered when classifying a lattice system. The first is whether $\vec{a}_1$ and $\vec{a}_2$ have the same length, and the second is whether the angle γ_{12} between $\vec{a}_1$ and $\vec{a}_2$ is 90° or 120°, or any other arbitrary value. Depending on these two factors, four lattice systems are defined in two-dimensional space: monoclinic, orthorhombic, hexagonal and tetragonal.

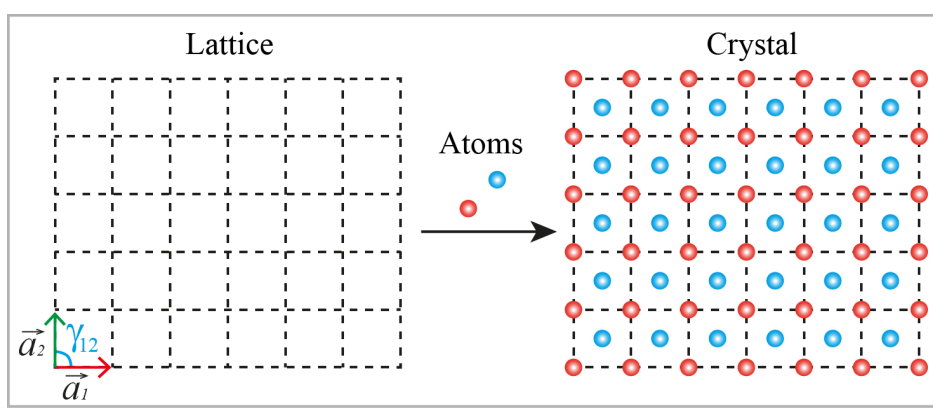

Figure 2.5: Sketch of a crystal structure in two dimensions.

In three-dimensional space, the unit cell is defined by three base vectors and the three angles between the base vectors. According to the classification rules described above, i.e., the length of the base vectors and the values of the angles, seven lattice systems can be defined. In some lattice systems, the atoms can be arranged differently, and these lattice systems can be classified into several subsystems. For instance, the cubic lattice system includes primitive cubic, base-centered cubic, body-centered cubic

and face-centered cubic. These subsystems are called the Bravais lattice, and there are 14 Bravais lattices in three-dimensional space. Since the atoms can be placed in different combinations of discrete positions in the lattice, there are 230 space groups describing the symmetry of the crystal structure. Therefore, a specific crystal structure is defined by the lattice system, the space group and the atoms.

2.2.4 Scattering by a crystal

The scattering of X-rays by a crystal can be considered as the summation of the scattering from all the atoms in the crystal, in analogy to the scattering from multiple electrons in a single atom. From the atomic structure factor in Eq. 2.10, the scattering factor of a crystal can be defined as:

$$F = \sum_{\vec{R}_m} \exp(\mathrm{i}\vec{Q} \cdot \vec{R}_m) \sum_{\vec{r}_j} f_j \exp(\mathrm{i}\vec{Q} \cdot \vec{r}_j) \tag{2.11}$$

Here, the scattering factor is separated into two parts. The first part is summation over all the lattice cells, where $\vec{R}_m$ denotes the position of the m^{th} lattice cell, and the second is summation over the atoms within the unit cell, where $\vec{r}_j$ denotes the position of the j^{th} atom. The second summation term in Eq. 2.11 is called the structure factor of the crystal. If the base vectors of the crystal are denoted $\vec{a}_1$, $\vec{a}_2$ and $\vec{a}_3$, then $\vec{R}_m$ and $\vec{r}_j$ can be expressed in terms of these three base vectors:

$$\vec{R}_m = m_1\vec{a}_1 + m_2\vec{a}_2 + m_3\vec{a}_3 \tag{2.12}$$

$$\vec{r}_j = x_j\vec{a}_1 + y_j\vec{a}_2 + z_j\vec{a}_3 \tag{2.13}$$

where m_1, m_2, m_3 are integers and x_j, y_j, z_j are fractional numbers.

To obtain the maximum amplitude in Eq. 2.11, the first summation term (lattice summation) should fulfil the following condition:

$$\vec{Q} \cdot \vec{R}_m = \mathrm{N} \cdot 2\pi \tag{2.14}$$

where N is an integer representing the scattering order. To find the solution for $\vec{Q}$ in Eq. 2.14, three base vectors are defined in reciprocal space:

$$\begin{aligned} \vec{b}_1 &= 2\pi \frac{\vec{a}_2 \times \vec{a}_3}{\vec{a}_1 \cdot (\vec{a}_2 \times \vec{a}_3)} \\ \vec{b}_2 &= 2\pi \frac{\vec{a}_3 \times \vec{a}_1}{\vec{a}_1 \cdot (\vec{a}_2 \times \vec{a}_3)} \\ \vec{b}_3 &= 2\pi \frac{\vec{a}_1 \times \vec{a}_2}{\vec{a}_1 \cdot (\vec{a}_2 \times \vec{a}_3)} \end{aligned} \tag{2.15}$$

The base vectors $\vec{a}_i$ and $\vec{b}_j$ have the relation:

$$\vec{a}_i \cdot \vec{b}_j = 2\pi\delta_{ij} \tag{2.16}$$

A vector in reciprocal space can then be expressed as:

$$\vec{G}_{hkl} = h\vec{b}_1 + k\vec{b}_2 + l\vec{b}_3 \tag{2.17}$$

When h, k and l are integers, $\vec{G}_{hkl}$ is a solution for $\vec{Q}$ in Eq. 2.14. The multiplication of $\vec{G}_{hkl}$ and $\vec{R}_m$ is:

$$\vec{G}_{hkl} \cdot \vec{R}_m = (h\vec{b}_1 + k\vec{b}_2 + l\vec{b}_3) \cdot (m_1\vec{a}_1 + m_2\vec{a}_2 + m_3\vec{a}_3) = 2\pi(hm_1 + km_2 + lm_3) \quad (2.18)$$

The integers h, k and l are called the Miller indices, and the notation (hkl) is used for the crystalline plane defined by the vectors $\vec{a}_1/h$, $\vec{a}_2/k$ and $\vec{a}_3/l$, while $\vec{G}_{hkl}$ is perpendicular to the (hkl) plane.

2.2.5 The structure factor

The solution for the lattice summation term was derived in the previous section (Eq. 2.14). Here, the expression for the structure factor, F_{hkl}, for the (hkl) crystalline plane, will be derived. Using Eq. 2.13 and $\vec{Q} = \vec{G}_{hkl}$, which is defined in Eq. 2.17, the structure factor can be written:

$$F_{hkl} = \sum_j f_j \, \mathrm{e}^{\mathrm{i}\cdot 2\pi\cdot(hx_j + ky_j + lz_j)} \quad (2.19)$$

The value of F_{hkl} depends on the positions of the atoms in the unit cell. In this work, the focus was on two kinds of crystal structures: the zincblende structure and the hexagonal structure, as shown in Figure 2.6(a) and 2.6(b), respectively. The structure factors for these two crystal structures are briefly summarized below.

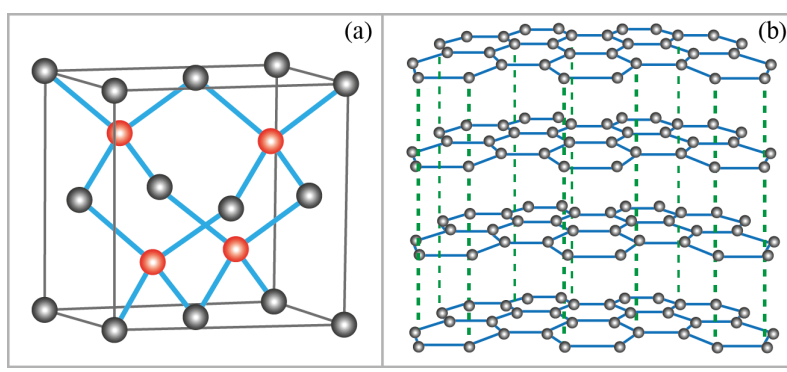

Figure 2.6: Sketches of the zincblende crystal structure (a), and hexagonal crystal structure (b).

The zincblende structure is a special case of the face-centered cubic lattice. It has two kinds of atoms in the unit cell. The atomic positions are given as: (0, 0, 0), (1/2, 1/2, 0), (1/2, 0, 1/2), and (0, 1/2, 1/2) for one kind of atom, and (1/4, 1/4, 1/4), (3/4, 3/4, 1/4), (3/4, 1/4, 3/4), and (1/4, 3/4, 3/4) for the other kind of atom. Inserting these atomic positions into Eq. 2.19 gives:

$$F_{hkl} = \left(1 + \mathrm{e}^{\mathrm{i}\cdot\pi\cdot(h+k)} + \mathrm{e}^{\mathrm{i}\cdot\pi\cdot(h+l)} + \mathrm{e}^{\mathrm{i}\cdot\pi\cdot(k+l)}\right)\left(f_{Aa} + f_{Ab}\,\mathrm{e}^{\mathrm{i}\cdot\pi\cdot\frac{h+k+l}{2}}\right) \quad (2.20)$$

where the subscripts Aa and Ab denote the two kinds of atoms. Since h, k, l are integers, F_{hkl} will have the simplified form:

$$\begin{aligned} hkl \text{ mixed} &: F_{hkl} = 0 \\ hkl \text{ unmixed} &: F_{hkl} = 4\left(f_{Aa} + f_{Ab}\, e^{i\cdot\pi\cdot\frac{h+k+l}{2}}\right) \end{aligned} \tag{2.21}$$

In Eq. 2.21, "mixed" means that (hkl) are a mixture of even numbers and odd numbers, and "unmixed" means that (hkl) are all odd numbers or all even numbers. The structure factor for the hexagonal lattice can be obtained in a similar way:

$$F_{hkl} = \left(1 + e^{i\cdot 2\pi\cdot(\frac{h+2k}{3}+\frac{l}{2})}\right)\cdot f \tag{2.22}$$

with the atom positions (0, 0, 0) and (1/3, 2/3, 1/2).

2.2.6 The Ewald sphere

The Ewald sphere is a useful way of illustrating the scattering of X-rays. The Ewald sphere is a sphere of reflection in reciprocal space. The principles of the Ewald sphere are discussed below in two-dimensional reciprocal space, in which the Ewald sphere is reduced to a circle, as shown in Figure 2.7. Each green spot represents a reflection with a reciprocal vector $\vec{G}_{hkl}$ starting from the origin O. The incident X-ray beam points towards the origin of reciprocal space with a wave vector $\vec{k}_i$. The reflection circle can be drawn with the center at the initial point of $\vec{k}_i$. The radius of the circle is thus equal to the magnitude of $\vec{k}_i$. Since only elastic scattering is considered here, the scattered X-ray wave vector, $\vec{k}_s$, should start at the initial point of $\vec{k}_i$ and end on the reflection circle. According to the discussion in Section 2.2.4, $\vec{G}_{hkl}$ is the solution to Eq. 2.11, which means all the (hkl) points on the reflection circle are solutions for $\vec{k}_s$.

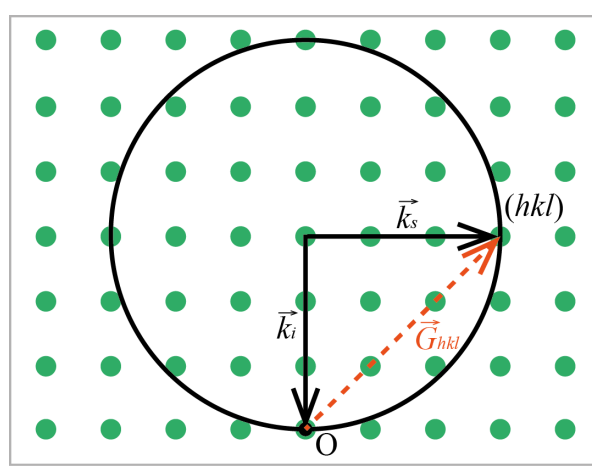

Figure 2.7: Sketch of the Ewald sphere in two-dimensional reciprocal space.

Extending these principles from the two-dimensional case to the three-dimensional case transforms the circle into the Ewald sphere. The magnitude of the incident

X-ray wave vector, $\vec{k}_i$, will increase as the X-ray photon energy is increased. As a consequence, the surface area of the Ewald sphere will increase quadratically, and will cover more (hkl) points. In practice, a larger Ewald sphere means that more reflections can be captured on a detector screen.

2.2.7 Energy scans

The Ewald sphere illustrates the relation between the crystal geometry and the X-ray photon energy. For momentum- (i.e., k-space-) sensitive measurements, such as phonon dynamics in solids, any broadening effects will influence the energy resolution of the measurements. Therefore, the response of the crystal must be carefully calibrated. An energy scan curve provides the overall response of the crystal to the X-rays.

Figure 2.8 shows two broadening effects on the energy scan: (a) sample broadening and (b) instrumental broadening. In Figure 2.8, the (hkl) points are represented by the green spots. If the crystal is perfect, the (hkl) points in reciprocal space should be infinitely small. However, there are always some defects in a crystal, which will cause broadening of the energy scan.

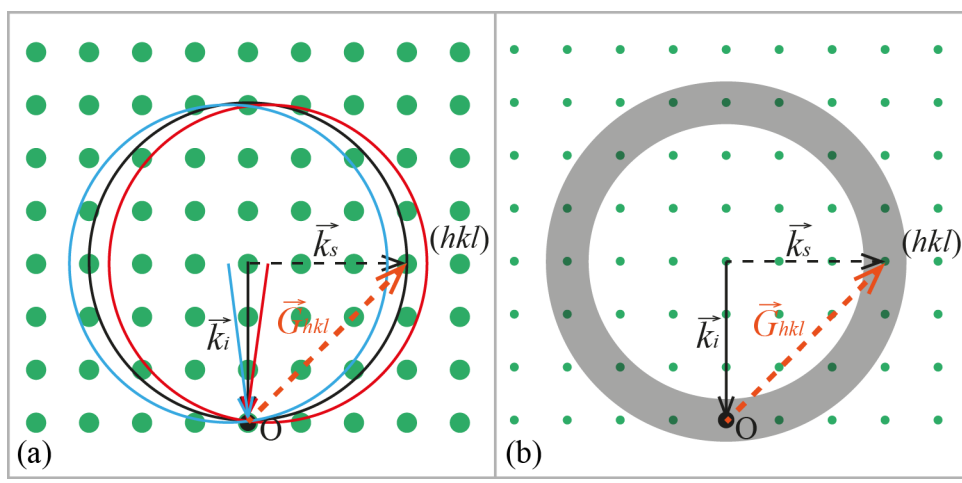

Figure 2.8: Broadening of the energy scan: (a) sample broadening and (b) instrumental broadening.

An energy scan can be obtained using a narrow-bandwidth X-ray beam, by changing the angle of incidence of the X-rays. It can be seen in Figure 2.8(a) that the Ewald sphere rotates with respect to the origin O and intersects with different part of the particular (hkl) point when the angle of incidence is changed. In this context the width of the energy scan depends on the size of the (hkl) point (sample broadening). The bandwidth of the X-ray beam is used as an example of instrumental broadening. The width of the Ewald sphere in Figure 2.8(b) represents the bandwidth of the X-ray beam, and it covers a large portion of the surrounding area of the (hkl) point. In this case, the width of the energy scan is given by the bandwidth of the X-ray beam. In practice, the energy scan of an experiment is the result of the convolution of all the broadening effects.

2.3 Laser-induced lattice dynamics

When a crystal lattice is excited by an ultrashort laser pulse, the laser pulse can create non-equilibrium states in the crystal. These non-equilibrium states lead to complex dynamics in the crystal. This work focused on the structural dynamics, which is referred to as lattice dynamics. Figure 2.9 shows several kinds of lattice dynamics, such as lattice vibrations (expansion and compression), atomic rearrangement and lattice disordering, all of which are related to the laser excitation fluence.

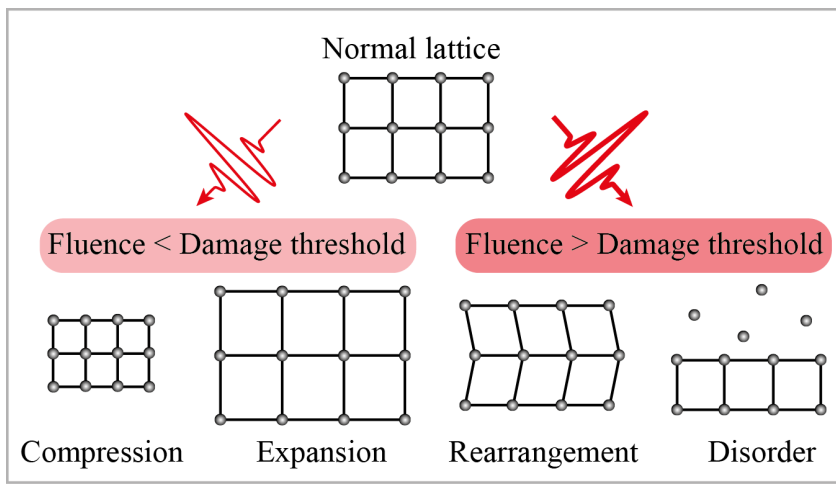

Figure 2.9: Illustration of different lattice dynamics.

2.3.1 Thermal strain in solids

When a solid is illuminated by an ultrashort IR laser pulse, the energy of the laser pulse will be absorbed by the electrons in the solid, and the electron temperature will increase rapidly within the duration of the laser pulse. The electrons will then transfer this heat to the lattice via electron-phonon coupling. Heating of the lattice generates thermal stress, which causes deformation of the crystal lattice. Strain is defined as the relative deformation of an object along a certain direction. Here, strain is used to describe lattice deformation after laser excitation, while a strain wave is the propagation of the strain in the crystal lattice.

Figure 2.10(a) and (b) illustrate the mechanism of strain generation. It can be seen in Figure 2.10(b) that part of the lattice is expanded, while another part is compressed, compared to the normal lattice in Figure 2.10(a). The strain profile of the crystal lattice can be obtained by plotting the strain as a function of depth, as shown in Figure 2.10(c). In general, positive values and negative values represent expansion and compression, respectively. The strain wave propagates at the speed of sound in that material. The focus in this thesis is on longitudinal strain, which means that the direction of vibration of the atoms and the direction of propagation of the strain wave are parallel.

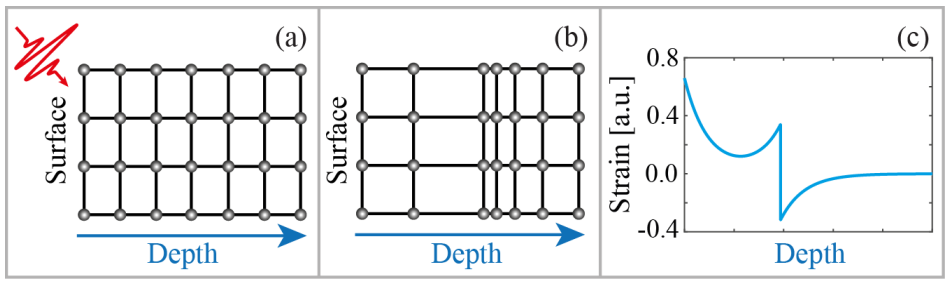

Figure 2.10: Illustration of strain generation. (a) Laser excitation. (b) Lattice deformation. (c) Strain profile.

2.3.2 The Thomsen model

The model proposed by Thomsen et al. [28, 29] was used in this work to describe the generation mechanism of the thermal strain in solids. In this model, the energy deposited per unit volume at a depth z is defined as:

$$W_l(z) = (1-R)\frac{Q_{laser}}{A\zeta}e^{-z/\zeta} \tag{2.23}$$

where R is the reflectivity of the material, Q_{laser} is the total energy of the laser pulse, A is the illuminated area and ζ is the optical absorption length of the laser wavelength. The energy deposited will induce a temperature change $\Delta T(z)$:

$$\Delta T(z) = \frac{W_l(z)}{C} \tag{2.24}$$

where C is the specific heat per unit volume. The heating of the lattice triggers a strain wave $\sigma(z,t)$, which has the following form:

$$\sigma_{z,t} = (1-R)\frac{Q_{laser}\alpha_l}{A\zeta C}\frac{1+\nu}{1-\nu}[e^{-z/\zeta}(1-\frac{1}{2}e^{-vt/\zeta}) - \frac{1}{2}e^{-|z-vt|/\zeta}\mathrm{sgn}(z-vt)] \tag{2.25}$$

where α_l is the linear thermal expansion coefficient, ν is Poisson's ratio, and v is the speed of sound along the longitudinal direction, which is defined as:

$$v^2 = 3\frac{1-\nu}{1+\nu}\frac{M_{bulk}}{\rho} \tag{2.26}$$

where M_{bulk} is the bulk modulus, and ρ is the density of the material.

InSb is used here as an example to discuss laser-induced strain. Figure 2.11(a) shows the strain profile in InSb at different time delays after laser excitation. When the energy of a laser pulse is deposited in a solid, the surface of the solid will be heated, generating one expansion strain component and two compression strain components simultaneously at the surface of the solid. To fulfil the initial condition, which is zero strain in the solid, the sum of these three strain components must be zero. The expansion strain component remains at the surface as a static strain. The two compression strain components will counter-propagate away from each other at the speed of sound. One compression wave propagates into the solid. The other compression

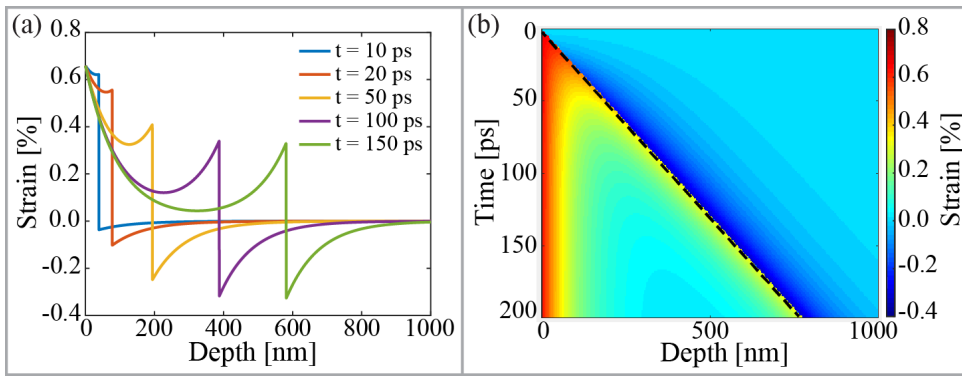

Figure 2.11: (a)The Thomsen strain profile of a single InSb crystal at different time delays. (b) Thomsen strain map. The absorbed laser fluence is 1 mJ/cm^2.

wave propagates towards the vacuum/solid interface, and is reflected at the interface with a phase change π, which means that the compression wave becomes an expansion wave. Figure 2.11(b) shows the overall strain map as a function of both time and depth, where the static strain at the surface of the solid can be clearly seen. The speed of sound can be extracted from the slope of the dashed line, which indicates the intersection between the compression wave and the expansion wave.

2.3.3 The phonon spectrum

The vibration of the crystal lattice is quantized as different phonon modes. Each phonon mode has its own oscillation frequency. A specific phonon mode can be probed using TRXD, the principle of which is shown in Figure 2.12. $\vec{k}_i$ and $\vec{k}_s$ are the wave vectors of the incident X-ray beam and the scattered X-ray beam, and $\vec{G}_{hkl}$ is the reciprocal vector of the (hkl) plane of the crystal. If the X-ray energy is detuned by $\Delta\vec{k}_i$, the phonon mode can be probed with a wave vector of $\vec{g}$.

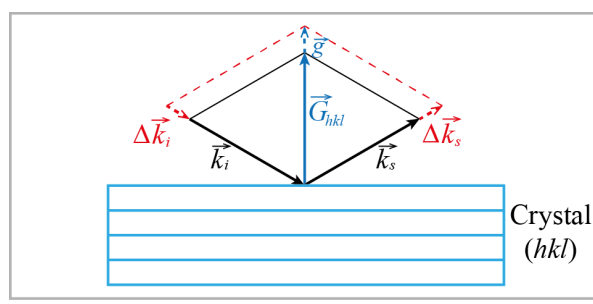

Figure 2.12: Illustration of the principle of probing a specific phonon mode using TRXD.

The phonon spectrum can be mapped as a function of time and energy offset by detuning the X-ray energy by different amounts, as shown in Figure 2.13(a). Here, the energy offset, ΔE, is used because it is easy to relate the phonon spectrum to the practical X-ray diffraction measurements, such as the energy scan. By extracting

a vertical lineout, e.g., the red dashed line in Figure 2.13(a), it is possible to obtain an energy scan of the crystal at a given time delay after laser excitation, as shown in Figure 2.13(b). A horizontal lineout, e.g., the black dot-dashed line in Figure 2.13(a), gives the phonon oscillations at a certain energy offset, as illustrated in Figure 2.13(c). The phonon frequency can then be extracted from the period of the oscillations. The phonon oscillations in Figure 2.13(c) have a sinusoidal profile with an exponential amplitude decay. In the next two sections, an alternative approach to modifying the phonon spectrum will be discussed.

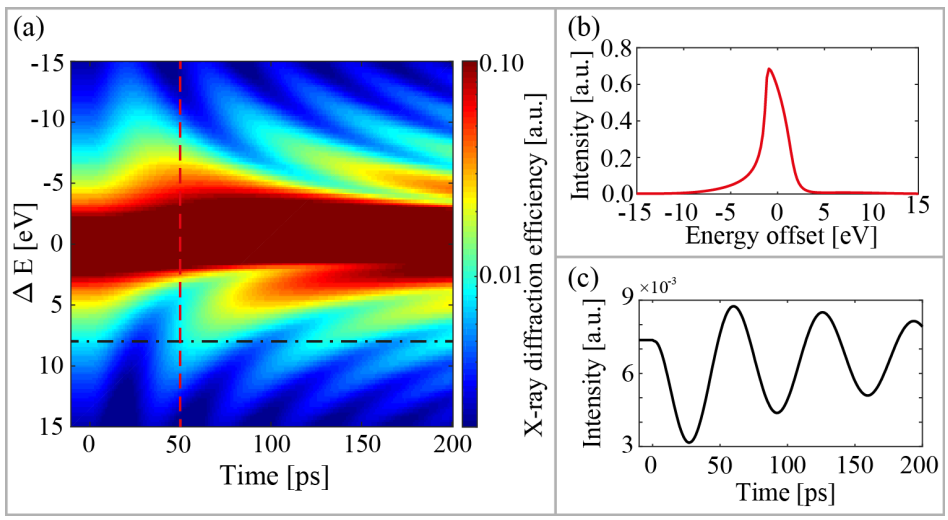

Figure 2.13: (a) Phonon spectrum map of a single InSb crystal. (b) Energy scan at a given time delay (50 ps). (c) Phonon oscillations at a given energy offset (8 eV).

2.3.4 Photo-acoustic transducer

A photo-acoustic transducer is a device that converts photon energy to acoustic energy. It can be used to modify the strain profile and the phonon spectrum in solids. The photo-acoustic transducers used in this work consisted of a thin metallic coating on a semiconductor substrate, as shown in Figure 2.14. The thickness of the metallic film can vary from tens of nm to hundreds of nm.

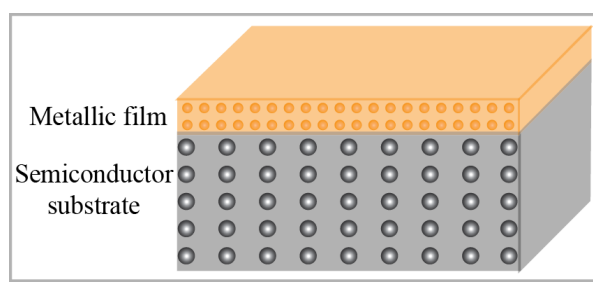

Figure 2.14: Sketch of a photo-acoustic transducer.

As mentioned in Section 2.1.2, the penetration depth of the laser pulse in metals is on the order of 10 nm. Therefore, when a photo-acoustic transducer is excited by an ultrashort laser pulse, the laser pulse energy is absorbed by the metallic film. Strain waves are generated in the film, and will be reflected at the vacuum/metal and metal/semiconductor interfaces. The transmission of the strain waves at the metal/semiconductor interface creates strain echoes in the semiconductor, as shown in Figure 2.15(a). Here, a Au/InSb transducer is used as an example. The thickness of the Au film was 100 nm, as indicated by the gold shaded area in Figure 2.15(a). The overall strain map is shown in Figure 2.15(b) as a function of time and depth, where it can be seen that the metallic film exhibits expansive strain, while the substrate exhibits both expansive and compressive strain.

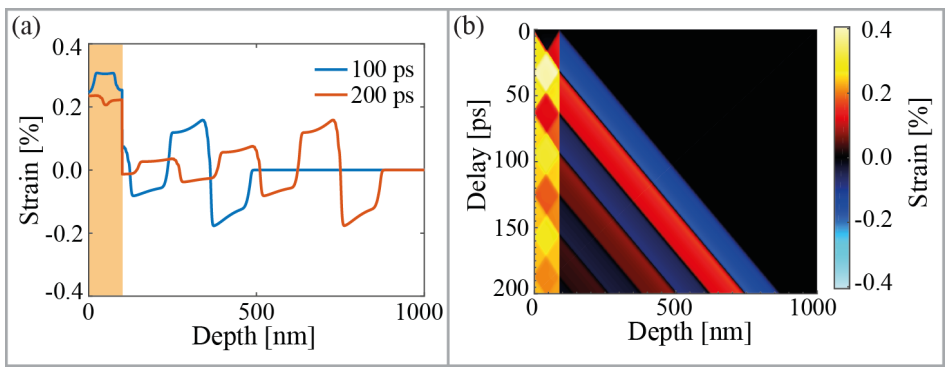

Figure 2.15: (a) Strain profile of a Au/InSb transducer at different time delays. (b) Strain map of the Au/InSb transducer as a function of time and depth. The absorbed laser fluence is 4 mJ/cm^2.

2.3.5 Modification of the phonon spectrum

It is clear from the previous section that the metallic film can influence the strain profile in the semiconductor substrate, and thus modify the phonon spectrum of the substrate. Figure 2.16 shows the phonon spectrum of the Au/InSb photo-acoustic transducer. The phonon spectrum in Figure 2.16 differs significantly from that in Figure 2.13(a) due to the periodicity of the strain echoes in the substrate. The periodicity depends on the propagation time, t_{echo}, of the strain wave in the metallic film, $t_{echo} = 2 \times d_{film}/v_{film}$, where d_{film} is the thickness of the metallic film and v_{film} is the speed of sound in the metallic film. The phonon modes with odd multiples of t_{echo} ($1 \times t_{echo}$, $3 \times t_{echo}$, $5 \times t_{echo}$, ...) will be enhanced in the substrate, while cancellation takes place for phonon modes with even multiples of t_{echo} ($2 \times t_{echo}$, $4 \times t_{echo}$, $6 \times t_{echo}$, ...). In Figure 2.16, the dot-dashed lines indicate the enhancement of two particular phonon modes, while the cancellation of another two phonon modes is indicated by the dashed lines.

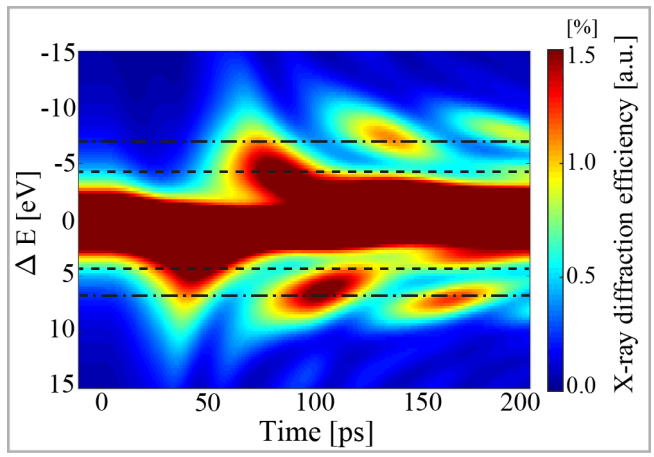

Figure 2.16: Phonon spectrum of a photo-acoustic transducer.

Since a photo-acoustic transducer can modify the phonon spectrum of the substrate, applications can be developed based on its enhancement/cancellation properties. One application of the photo-acoustic transducer, the X-ray switch, is discussed in Section 3.2.5, while Section 5.2 describes the performance of a Au/InSb X-ray switch.

2.3.6 Lattice disordering

The laser fluence used to excite the thermal strain described in the previous sections was only a few mJ/cm^2. This fluence is well below the damage threshold of the materials studied. The number of carriers excited will increase with increasing laser fluence, which may induce disordering in the crystal lattice or melting. There are two general melting mechanisms in semiconductors under ultrashort laser pulse excitation: thermal melting and non-thermal melting [5, 30]. Similar to the generation of thermal strain, thermal melting is also due to electron-phonon coupling, which transfers energy from the electron system to the lattice system, heating the crystal lattice. Thermal melting takes place on the time scale of a few ps [4]. If the density of excited carriers exceeds a critical value (10%), the atomic potential surface will be strongly influenced, triggering atomic relocation [18, 19, 31, 32]. This kind of disordering is called non-thermal melting, and usually takes place on the fs timescale [33–36]. An experiment designed to study non-thermal melting in a semiconductor (InSb), and potential applications, is presented and discussed in Section 5.5.

2.3.7 Large-amplitude strain: pressure wave

The strain discussed in Sections 2.3.2 and 2.3.4 is usually very small, $< 1\%$, due to the low laser fluence used for excitation. Since materials have different densities in their solid and liquid states, strain waves with large amplitudes can be generated at the liquid/solid interface, which can propagate towards the solid part of the material [37, 38]. The stress, which is also called the internal pressure, is associated with the strain waves, and it can be extracted from the amplitude of the strain and the

bulk modulus of the material. The bulk modulus describes the compressibility of a solid, and it varies from tens of GPa to hundreds of GPa for different materials. The amplitude of the strain waves resulting from melting can be a few percent, which means the internal pressure can be a few GPa to tens of GPa. In this context, the strain waves are usually called pressure waves or shock waves, and can be used to study the structural dynamics of solids under high pressure on the ps timescale. Two experiments are discussed in Sections 5.3 and 5.4, in which pressure waves were generated and characterized in an Al/InSb transducer and a graphite crystal.

Chapter 3

Experimental Method

Time-resolved X-ray diffraction/TRXD was used as the experimental method to study phonon dynamics, pressure waves and ultrafast lattice disordering. In this chapter, the principles of TRXD will be introduced, and an overview of hard X-ray sources that can provide fs/ps X-ray pulses will be given. At the end of this chapter, time-resolved electron diffraction will be introduced as a complementary experimental method.

3.1 X-ray diffraction

3.1.1 Bragg's law

The principle of X-ray diffraction is based on Bragg's law, which describes the conditions for constructive interference between X-rays scattered by a crystal, as shown in Figure 3.1.

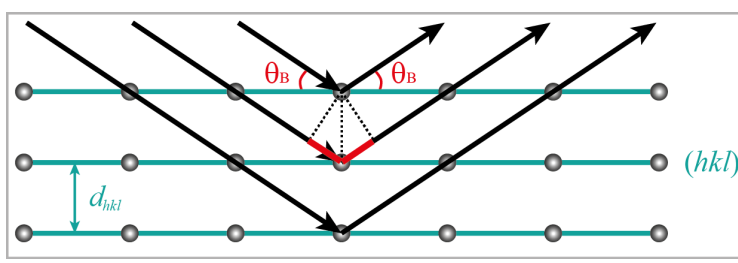

Figure 3.1: Illustration of Bragg's law.

Bragg's law can be expressed as:

$$2 \cdot d_{hkl} \cdot \sin\theta_B = \mathrm{N} \cdot \lambda \tag{3.1}$$

where d_{hkl} is the distance between two adjacent crystalline planes with the same Miller indices (hkl), which is called d spacing. θ_B is the Bragg angle, λ is the wavelength of the incident X-ray beam, and N is an integer denoting the diffraction order. Strong interference peaks can be formed by constructive interference when the difference in

path length of the X-ray beams diffracted from two adjacent (hkl) planes is equal to an integer multiple of the X-ray wavelength. The sum of the red lines in Figure 3.1, representing the difference in path length, is $2 \times d_{hkl} \times \sin\theta_B$.

3.1.2 Coplanar & non-coplanar reflection

In order to observe the reflection from a specific (hkl) crystalline plane, the structure factor (F_{hkl}) must be non-zero and the angle between the incident X-ray beam and the (hkl) crystalline plane must equal the Bragg angle, θ_B. The structure factor is defined by the crystal symmetry and the positions of the atoms in the unit cell. The X-ray angle of incidence is determined by the experimental geometry. Figure 3.2 shows two sets of crystalline planes in the same crystal. It is obvious that they have different spacings, d, which means their Bragg angles are different. This raises the question of how reflections can be observed from both at a given X-ray angle of incidence. The solution is to use different reflection geometries: coplanar reflection and non-coplanar reflection.

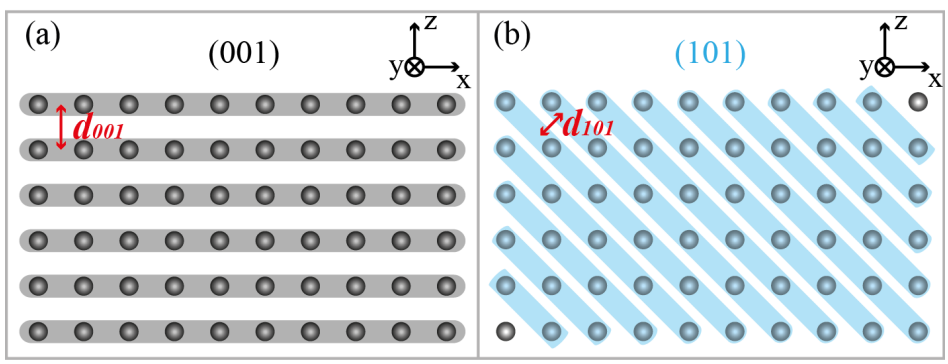

Figure 3.2: Illustration of different crystalline planes in the same crystal.

The reflection geometry is defined by the surface normal of the crystal and the scattering plane spanned by the incident X-ray beam and the scattered X- ray beam. If the surface normal is parallel to the scattering plane, the geometry is called coplanar, otherwise, it is called non-coplanar. Both reflection geometries are shown in Figure 3.3. The surface plane in Figure 3.3 is the (001) crystalline plane, and the (101) crystalline plane has a well-defined angle with respect to the surface plane. The Bragg condition for the (001) plane can be fulfilled by adjusting the angle of incidence of the X-ray beam. This angle is independent of rotation around the surface normal (referred to as azimuth rotation). However, the angle of incidence with respect to the (101) crystalline plane will depend on the azimuth rotation. This allows matching of the Bragg conditions for both (001) and (101) reflections simultaneously.

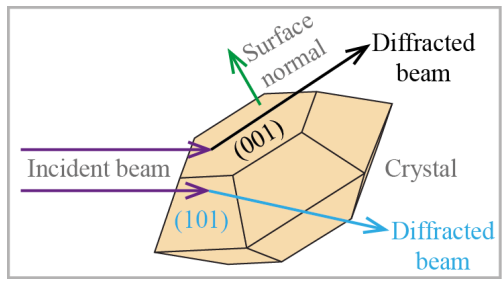

Figure 3.3: Illustration of coplanar reflection (black) and non-coplanar reflection (blue).

Figure 3.4 illustrates the non-coplanar reflection geometry. The incident angle of the X-ray beam is denoted θ_i, which is the angle between the incident X-ray beam and the sample surface. For a given crystalline plane (e.g., the (101) plane in Figure 3.3), a circle can be drawn for the scattered X-ray wave vector, $\vec{k}_s$ (the purple circle in Figure 3.4) with respect to the incident X-ray wave vector, $\vec{k}_i$. The angle between $\vec{k}_i$ and $\vec{k}_s$ is $2 \times \theta_B$. The reciprocal vector of the given crystalline plane is illustrated by $\vec{G}_{hkl}$, and a circle of $\vec{G}_{hkl}$ (the blue circle in Figure 3.4) can be drawn by rotating the sample around the surface normal. The intersection of these two circles, indicated by the red star, indicates the conditions that have to be fulfilled to observe the scattering signal from the given crystalline plane in the non-coplanar reflection geometry. The azimuth angle is denoted Ψ.

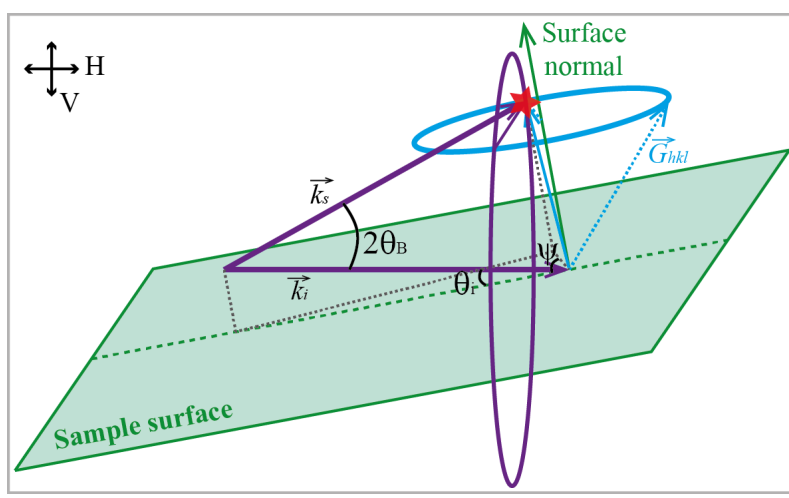

Figure 3.4: Sketch of non-coplanar reflection geometry.

3.1.3 Sample geometry: symmetric & asymmetric

The X-ray diffraction efficiency is defined not only by the reflection geometry, but is also influenced by the sample geometry. Since the crystal can be cut along certain directions, two sample geometries must be considered: symmetric and asymmetric.

In this section, the influence of sample geometry will be discussed in the coplanar reflection case. Figure 3.5 shows the coplanar reflection from a symmetric-cut crystal and an asymmetric-cut crystal. It should be noted that the crystalline planes in Figure 3.5(a) and (b) are the same (hkl) set, and they have the same d spacing. For the symmetric-cut crystal, shown in Figure 3.5(a), the crystalline plane is parallel to the sample surface, and to fulfil the Bragg condition, the incident angle of the X-ray beam, with respect to the sample surface, should be equal to the Bragg angle. For the asymmetric-cut crystal in Figure 3.5(b), the angle between the crystalline plane and the sample surface is close to the Bragg angle. Therefore, the angle of incidence of the X-ray beam must be very small to fulfil the Bragg condition. It is clear from Figure 3.5 that the X-ray beam penetrates much deeper in the symmetric-cut crystal, whereas only a shallow region below the sample surface is probed by the X-ray beam in the asymmetric-cut crystal.

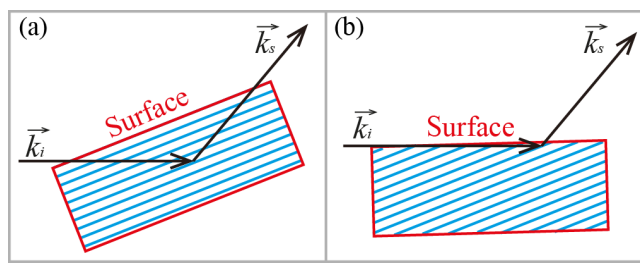

Figure 3.5: Coplanar reflection from a symmetric-cut crystal (a) and an asymmetric-cut crystal (b).

3.1.4 Probing depth

The probing depth is the depth to which the X-rays can provide information on the structural changes in solids. The penetration depths given in Table 2.2 are the probing depths for normal-incidence geometry. In general, the probing depth of X-rays depends on their penetration depth, their angle of incidence, and the refractive index of the materials. The refraction of X-rays at the vacuum/sample interface is not included in Figure 3.5 as the refractive indices of the materials studied in this work are very close to 1. It can be seen from this figure that the probing depth is much smaller for the asymmetric-cut crystal.

Figure 3.6 shows the probing depth of X-rays in InSb as a function of angle of incidence for a photon energy of 6 keV. It can be seen that the probing depth changes dramatically at angles between 0.1° and 1° (shown in red). At an angle of 0.1° the probing depth is ∼2 nm, and increases to > 50 nm at 1°. Therefore, the angle of incidence must be chosen appropriately for surface-sensitive X-ray diffraction experiments, in order to match the probing depth and the excitation depth of the laser pump beam. For instance, to study non-thermal melting in InSb (Section 5.5), the angle of incidence was set to 0.75° with a photon energy of 3.56 keV, and in this geometry the probing depth was 28 nm.

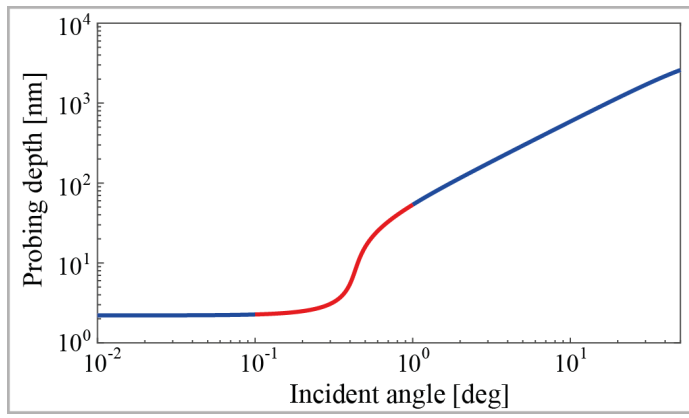

Figure 3.6: Probing depth of X-rays in InSb at different incident angles for a photon energy of 6 keV.

3.1.5 Grazing incidence X-ray scattering

Grazing incidence X-ray scattering (GIXS) is widely used in surface-sensitive measurements [39–41]. In GIXS geometry, the incident angle is usually very close to the critical angle. The probing depth of the X-rays in GIXS geometry can be few tens of nm, which is of the same order as the penetration depth of the laser beam.

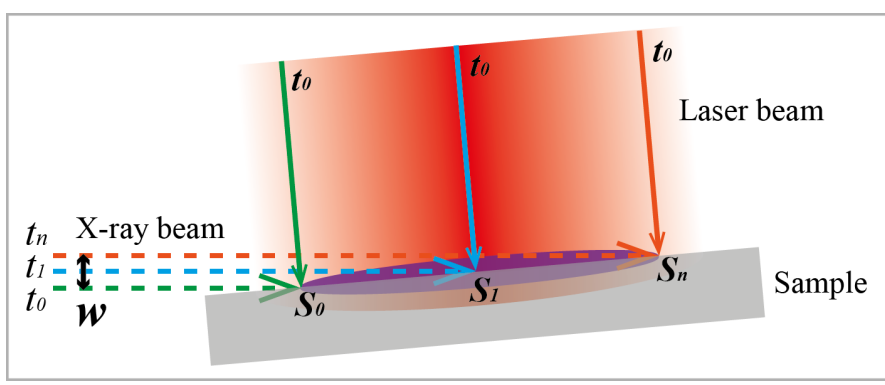

Figure 3.7: Illustration of a cross geometry for pump-probe experiments: normal incidence for the laser beam and grazing incidence for the X-ray beam.

Figure 3.7 shows a so-called cross geometry for a pump-probe experiment using GIXS for the X-ray beam and normal incidence for the laser beam. Since the incident angle in GIXS geometry is small, the footprint of the X-ray beam will be fairly large. Different parts of the X-ray beam will have different propagation times (t_0, t_1, ... t_n) at different positions (S_0, S_1, ... S_n) in the sample, as illustrated in the figure. For instance, an X-ray beam with a full width at half maximum (FWHM) of 100 μm, indicated by the black arrow in Figure 3.7, has a footprint of 5.7 mm at an angle of 1°. This footprint corresponds to a propagation time of 19 ps. Since the laser beam has normal incidence, all the positions within the pump beam area (S_0, S_1, ... S_n)

are excited simultaneously at t_0. Under these conditions, a time axis is automatically created by the difference in the propagation time of the laser beam and the X-ray beam. The cross geometry has been used to investigate atomic motion during phase transitions on the ultrafast time scale [34–36]. The experiment described in Section 5.5, in which non-thermal melting of InSb was studied, was also carried out using this geometry.

3.1.6 Time-resolved X-ray diffraction

Time-resolved X-ray diffraction/TRXD is an experimental method commonly used to study the structural changes in materials on the atomic scale [6, 8]. It combines X-ray techniques with laser techniques. The laser beam excites a solid system from a state of equilibrium to a non-equilibrium state. The X-ray beam is then used to monitor the evolution of the laser-excited system. In this context, the laser beam and the X-ray beam are usually referred to as the pump beam and the probe beam, respectively.

Figure 3.8 shows a typical experimental setup for general pump-probe experiments, such as optical-pump/optical-probe experiments [42], optical-pump/X-ray-probe experiments [43], THz-pump/electron-probe experiments [44], etc. In Figure 3.8, the laser beam and the X-ray beam are spatially overlapped on the sample. The difference in arrival time between the laser beam and the X-ray beam can be adjusted using a delay line. The diffracted X-ray intensity is captured by a detector. Each position of the delay line corresponds to a specific time delay between the pump beam and the probe beam, i.e., a time point. The structural evolution of the sample can be captured by the detector at different time delays by varying the difference in time between the pump beam and the probe beam.

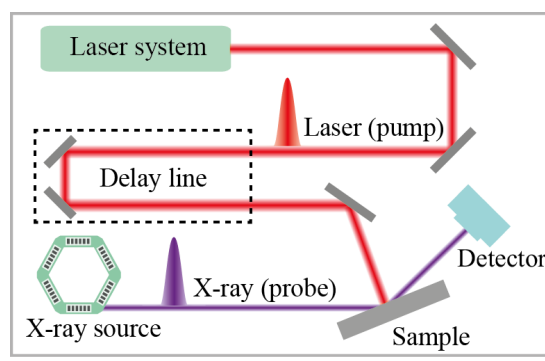

Figure 3.8: Schematic of the experimental setup used for pump-probe experiments.

Figure 3.9 shows the results of a TRXD measurement from a photo-acoustic transducer (Au/InSb). Figure 3.9(a) shows the diffracted intensity at different time delays, and each image constitutes a data point in the curve shown in Figure 3.9(b). This curve is made up of 140 data points, and the step size between two neighboring data points is 2 ps. This experiment is discussed in detail in Section 5.2.

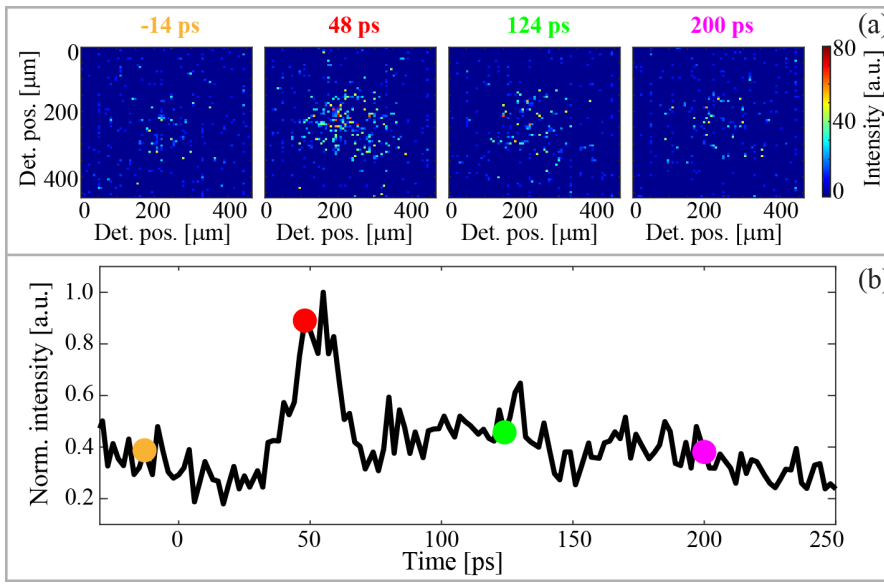

Figure 3.9: (a) X-ray diffraction images collected at different time delays. The detector positions are given on the image axes. (b) Evolution of the X-ray diffraction intensity as a function of time. The colored dots represent the diffraction intensity at various time delays shown in (a).

3.2 X-ray sources

The time resolution of a pump-probe experiment generally depends on the pulse duration of both the pump beam and the probe beam. Techniques are now available to generate ultrashort laser pulses, on the order of fs [45, 46]. However, it is still difficult to obtain ultrashort X-ray pulses. Since the studies described in this thesis focus on structural dynamics taking place on the time scale from femtoseconds to picoseconds, this section provides an overview of the hard X-ray sources that can provide short X-ray pulses, such as the laser plasma sources, storage rings and free-electron lasers.

The brilliance is often used to describe the quality of an X-ray source. The brilliance of an X-ray source describes the photon distribution in time, space and spectra, and is expressed in the following units:

$$\frac{\text{photons}}{\text{second} \cdot \text{mrad}^2 \cdot \text{mm}^2 \cdot 0.1\% \text{ bandwidth}}$$

In experiments, it is important to distinguish between average brilliance and peak brilliance. The number of photons per second is used to calculate the average brilliance, while calculation of the peak brilliance requires the number of photons per pulse and the pulse duration [47]. In the work described in this thesis, the photon flux is a more important parameter, since it directly influences the signal-to-noise (S/N) ratio and the data acquisition time. The photon flux is defined as the number of photons per second. In repetitive experiments, the laser excitation fluence is below the damage threshold of the materials, and the structural change in the materials will relax to the equilibrium state. In this case, the S/N ratio can be estimated from the photon flux.

In single-shot experiments, the laser excitation fluence is above the damage threshold of samples, and the photo-induced structural change is irreversible. In this case, the S/N ratio is defined by the number of photons per pulse, which is the photon flux divided by the repetition rate. Figure 3.10 shows a comparison of the X-ray sources discussed in the following sections, in terms of pulse duration and the number of photons per pulse on the sample.

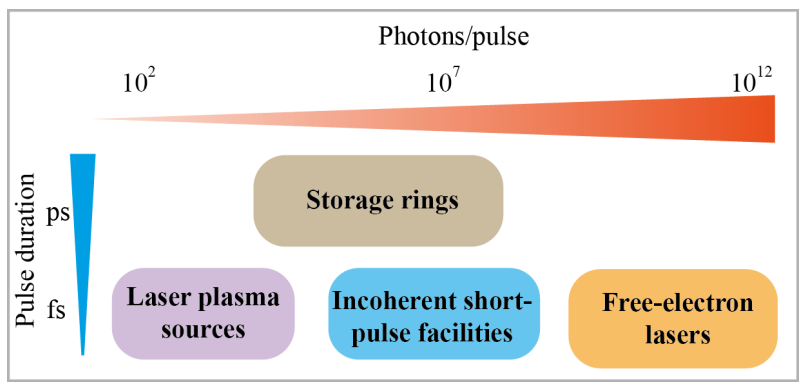

Figure 3.10: Comparison of different X-ray sources in terms of pulse duration and photons per pulse on the sample.

3.2.1 Laser plasma sources

The generation of X-rays using laser plasma sources can be described in three steps: plasma generation from a metal target, acceleration of electrons, and recombination of electrons with the target [48]. When a metal target is illuminated by an ultrashort, intense laser pulse, with a duration shorter than 100 fs and a peak intensity of 10^{15}–10^{16} W/cm^2, the electrons in the metal target will be ionized, forming a thin layer of plasma at the target surface. After the creation of the plasma, the laser field will drive the motion of the free electrons. During the first half-cycle of the driving laser field, these free electrons are extracted from the target surface. The electrons are then accelerated by the second half-cycle of the driving laser field, and reach an average kinetic energy of several tens of keV. These so-called hot electrons penetrate into the metal target and excite K-shell electrons in the atoms. X-rays are then emitted during the recombination of the K-shell holes and outer-shell electrons. The duration of the X-ray radiation pulse is on the same order as the driving laser pulse duration, as the electrons can only be generated and accelerated during the laser pulse. The photon flux is in the range of 10^8–10^{10} photons/s [49–52]. The driving laser is usually operated at a repetition rate of 0.01–10 kHz, which means the number of photons per pulse is 10^5–10^7. Due to the spontaneous emission process, the X-ray radiation is uniformly distributed over a solid angle of 4π, which means that only a fraction of the emitted photons can be focused onto the sample and used to perform experiments. The number of photons per pulse reaching the sample is on the order of 10^2–10^5 [53–57].

3.2.2 Storage rings

X-ray radiation can also be generated by high-energy electrons when they are accelerated [58]. A storage ring is a type of accelerator in which high-energy electrons can be circulated at highly relativistic velocities for a few hours [59]. When these high-energy electrons pass through a magnetic field, they will emit synchrotron radiation along the direction tangential to their orbital path. Three devices can be used to provide a magnetic field: bending magnets, wigglers and undulators. Storage rings usually provide a photon flux in the range of 10^{10}–10^{13} photons/s. The repetition rate of the pulses is on the order of MHz, and the number of photons per pulse is in the range of 10^{4}–10^{7}, which is similar to that from the laser plasma sources. However, unlike laser-driven plasma sources, the divergence of synchrotron radiation is very small, on the order of milliradians. This means that all the photons in the X-ray pulse can be used to conduct experiments.

Bending magnets are generally used to guide electrons in the storage ring, and they can also be used to generate synchrotron radiation. The critical energy, which divides the total emitted power in half, of the bending magnet radiation is given as [60]:

$$E_c = \frac{3\hbar e \gamma^2 B}{2m} \tag{3.2}$$

where $\hbar$ is the reduced Planck's constant, e is the elementary charge, γ is the relativistic parameter, B is the magnetic field and m is the rest mass of the electron. The relativistic parameter γ is defined as:

$$\gamma = \frac{1}{\sqrt{1 - (\frac{v_e}{c})^2}} \tag{3.3}$$

where v_e is the speed of the electron and c is the speed of light in vacuum. Substituting the tabulated values for all the constants, allows Eq. 3.2 to be expressed in a simpler form:

$$E_c \approx 0.6650 \cdot E_e^2 \cdot B \tag{3.4}$$

where E_c is in keV, E_e is the electron kinetic energy in GeV, and B is in tesla (T).

The wigglers and the undulators, which are usually referred to as an insertion device (ID), are installed in the straight section of the storage rings. An ID consists of a series of periodic dipole magnets [60]. The critical energy of wiggler radiation has a similar form to that in Eq. 3.2. The magnetic field of wigglers can be stronger than that of bending magnets, and wiggler radiation can therefore have a higher critical energy. Since the electrons can bend multiple times in wigglers, the wiggler radiation will have more power than bending magnet radiation.

The difference between undulators and wigglers is that the magnetic field of undulators is weaker, which causes shallow bends in the path of the electrons. These shallow bends constitute a small source and also induce interference effects. The wavelength of the undulator radiation is given by [61]:

$$\lambda = \frac{\lambda_u}{2\gamma^2}\left(1 + \frac{K_u^2}{2} + \gamma^2\theta_e^2\right) \tag{3.5}$$

where λ_u is the periodicity of the dipole magnets, γ is the relativistic parameter of the electrons, as defined in Eq. 3.3, θ_e is the angular deviation from the axis of the

electron beam, and K_u is the dimensionless undulator parameter, which is defined as [61]:

$$K_u \equiv \frac{eB\lambda_u}{2\pi mc} \tag{3.6}$$

where e, B, m and c have the same meanings as in Eq. 3.2 and Eq. 3.3. The undulator parameter, K_u, describes the deflection of the undulator radiation. If $K_u \gg 3$, the electrons will oscillate with large amplitude, the emitted radiation will be distributed over a large opening angle, and no interference takes place. When $K_u \leq 3$, the radiation emitted from each period of the undulators will overlap, and interference can occur, resulting in peaks in the radiation spectrum [62]. Using tabulated constants and the Planck–Einstein relation, $E = hc/\lambda$, gives a simplified expression for the radiation energy emitted and the undulator parameter:

$$E \approx \frac{0.9496 \cdot E_e^2}{\lambda_u \left(1 + \frac{K_u^2}{2} + \gamma^2\theta_e^2\right)} \tag{3.7}$$

$$K_u \approx 0.9337 \cdot B \cdot \lambda_u \tag{3.8}$$

where E is in keV, λ_u is in cm, and E_e and B have the same units as in Eq. 3.4.

The electrons will lose energy due to the emission of radiation. This loss of energy can be restored by a radio frequency (RF) cavity, which gives a small energy boost to the electrons. The RF cavity also separates the electrons in the storage rings into bunches. The length of these bunches defines the pulse duration of the emitted X-ray radiation, which is typically on the order of 100 ps [63, 64]. To perform TRXD experiments, the pump beam must be synchronized to a given bunch in the storage ring. Storage rings can be operated in different modes to increase the number of electrons in a given bunch: single-bunch mode, multi-bunch mode and hybrid mode [65]. In single-bunch mode, there is only one bunch of electrons in the storage ring. The multi-bunch mode is the normal mode of operation, but the number of bunches can be reduced, e.g., 4 bunches or 16 bunches at the European Synchrotron Radiation Facility (ESRF) in Grenoble [66]. The hybrid mode is a combination of single-bunch mode and multi-bunch mode. In this mode, a single bunch is isolated by a large gap from the rest of the bunches [60].

Part of this work was carried out at beamline D611 at MAXLAB (Paper II). The synchrotron radiation was generated by a bending magnet, and the bunch duration in the MAX II storage ring was 600 ps. A temporal resolution as high as 2 ps was achieved using a streak camera, as described in Section 3.2.5.

3.2.3 Free-electron lasers

The free-electron laser (FEL) is a unique source that provides coherent X-rays with a pulse duration on the order of tens of femtoseconds. In FELs, the electrons are generated from a photocathode by an ultrashort laser pulse. The kinetic energy of the electrons is increased to the GeV range in a linear accelerator. Bunch compressors are used to shorten the length of the electron bunch, providing emitted radiation with a short pulse duration. For instance, the pulse duration of the Linac Coherent Light Source (LCLS) at the SLAC National Accelerator Laboratory in Stanford is on the order of 100 fs [67, 68].

As mentioned in the previous section, the undulator radiation suffers from interference effects when $K_u \leq 3$. The length of the undulators at storage rings is usually a few meters. In FELs, the length of the undulators is much longer, for example, 60 m at the SwissFEL [69] and 130 m at the LCLS [67]. When an electron bunch enters the undulators, radiation will be emitted, which will modulate the electron bunch into micro-bunches [70]. The radiation from each micro-bunch is phase aligned, giving a very high peak intensity. This is called self-amplified spontaneous emission [70]. The photon flux of FELs is in the range of 10^{12}–10^{14} photons/s [67, 69]. The repetition rate of FELs is much lower than that of storage rings: for example, 30 Hz at the SPring-8 Angstrom Compact free electron LAser (SACLA) [71], 120 Hz at the LCLS [67] and 100 Hz at the SwissFEL [69]. Taking the repetition rate into account, the number of photons per pulse at FELs is in the range of 10^{10}–10^{11}, which is 5–6 orders higher than the number of photons per pulse at storage rings.

3.2.4 Incoherent short-pulse facilities

From the previous section, it was clear that FELs are attractive as they can provide short X-ray pulses with high photon flux. However, there are only a few hard X-ray FELs worldwide, and competition for beamtime is very high at these facilities. Incoherent short-pulse facilities offer an alternative for generating X-ray pulses with a similar photon flux to that of storage rings, and similar pulse duration to that of FELs. As in the case of FELs, a linear accelerator is used to provide short electron bunches, which are passed through an undulator (5–10 m) generating X-ray pulses with a pulse duration of ∼100 fs. This concept was tested at the Sub-Picosecond Photon Source (SPPS) in Stanford, where 80-fs X-ray pulses were generated with 3×10^7 photons per pulse [72]. The SPPS was closed in 2006 for the construction of the LCLS.

The FemtoMAX beamline at the short-pulse facility of the MAX IV Laboratory was designed using the similar concept to the SPPS to provide incoherent X-ray pulses with a pulse duration <100 fs (Paper I). Two experiments, which are included in this thesis, were carried out as part of the commissioning of the FemtoMAX beamline. The electron bunches are generated with a photo-cathode gun and accelerated to 3 GeV in a linear accelerator [73]. Two bunch compressors are used to reduce the duration of the electron bunch to < 100 fs [74]. The X-ray radiation is generated by a 10-m-long in-vacuum undulator. The FemtoMAX beamline is equipped with two kinds of monochromators, a double-crystal monochromator and a multilayer monochromator, for monochromatization of the X-ray energy.

The double-crystal monochromator has a bandwidth of 4×10^{-4}. Figure 3.11 shows a monochromator scan using a double-crystal monochromator, which employs InSb (111) reflection. The instant charge was measured at different monochromator angles, and is shown in Figure 3.11(a), where three peaks are visible at 27.5°, 13.7° and 8.9°. These monochromator angles can be converted to photon energies using Bragg's law, as shown in Figure 3.11(b), and correspond to energies of 3.6 keV, 7.0 keV and 10.7 keV. These three peaks are the fundamental peak, the second harmonic and the third harmonic of the undulator spectrum. To convert the instant charge to the number of photons per pulse, the electron-hole pair creation energy must be taken into account. In this scan, a silicon detector was used, and the electron-hole pair creation energy for silicon is 3.7 eV, which means that an X-ray photon with an energy of 3.7 keV can create 1000 electron-hole pairs, and contribute 1.6×10^{-16} C

to the instant charge. The detector had a gain factor of 1000. Using the gain factor and the electron-hole pair creation energy of the detector, allows the instant charge in Figure 3.11(a) to be converted into the number of photons per pulse, as shown in Figure 3.11(b), where it can be seen that the number of photons per pulse of the fundamental peak is $\sim 2.5 \times 10^5$, with a bandwidth of $\sim$100 eV. Since a higher-energy photon creates more electron-hole pairs than a lower-energy photon, the number of photons per pulse for the third harmonic is similar to that for the second harmonic, despite the fact that the instant charge of the third harmonic is almost a factor of 2 higher than that of the second harmonic (Figure 3.11(a)).

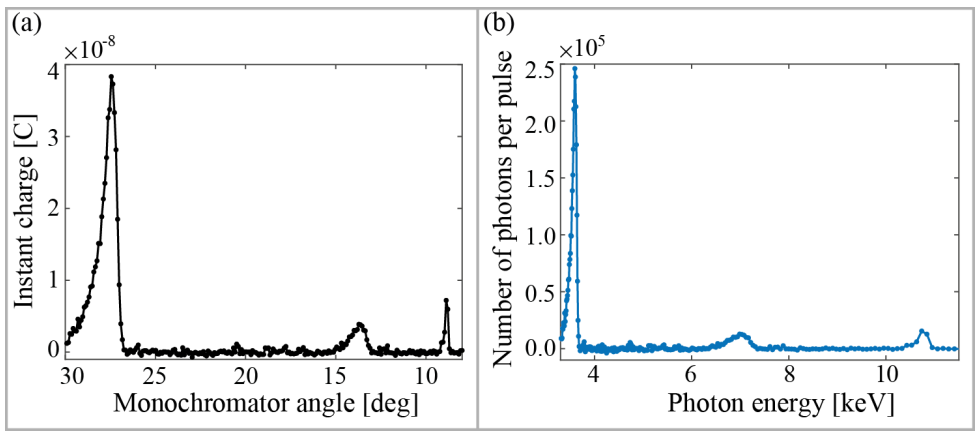

Figure 3.11: Monochromator scan using a double-crystal monochromator to obtain the undulator spectrum.

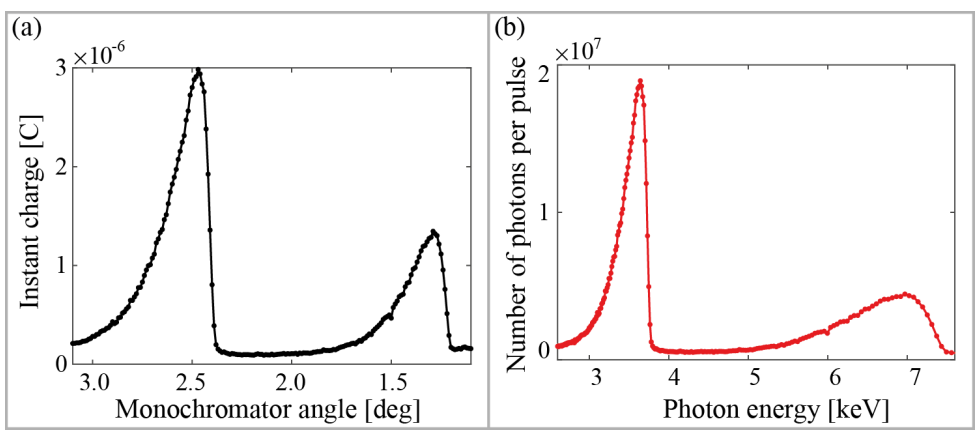

Figure 3.12: Monochromator scan using a multilayer monochromator to obtain the undulator spectrum.

A multilayer monochromator can be used to increase the photon flux. Figure 3.12 shows a monochromator scan using a multilayer monochromator that consists of Ni and B_4C, with a d spacing of 39.5 Å and a bandwidth of $< 2\%$ (Paper I). As the d spacing is

known, the monochromator angle (Figure 3.12(a)) can be converted to photon energy (Figure 3.12(b)). It can be seen from Figure 3.12(b) that the fundamental peak is at 3.6 keV, and the second harmonic is at 7.0 keV, as in Figure 3.11(b). The number of photons per pulse can be calculated from the instant charge, using a similar approach to that described above. Comparing Figure 3.12(a) and Figure 3.11(a) shows that the instant charge from a multilayer monochromator is approximately two orders of magnitude higher than that from a double-crystal monochromator, and thus the multilayer monochromator delivers a much higher photon flux than the double-crystal monochromator. The number of photons per pulse of the fundamental peak in Figure 3.12(b) is $\sim 2 \times 10^7$, showing that the design specification of the FemtoMAX beamline has been achieved (Paper I). The FWHM of the fundamental peak in Figure 3.12(b) is ~330 eV.

A pair of harmonic rejection mirrors was implemented to suppress the higher harmonics, as higher photon energies have smaller critical angles for specular reflection. These two mirrors are mounted parallel at an adjustable angle. Since the fundamental energies have larger critical angles, these energies can be reflected by the mirrors, while the higher harmonics will penetrate into the substrate of the mirrors. This allows a higher photon flux to be obtained than with the multilayer monochromator.

3.2.5 Achieving high temporal resolution at storage rings

Although the pulse duration at storage rings is hundreds of picoseconds, several techniques and devices have been developed to achieve high temporal resolution, such as low-alpha mode, femtoslicing, streak cameras and X-ray switches. Figure 3.13 illustrates where these techniques/devices are employed at a storage ring.

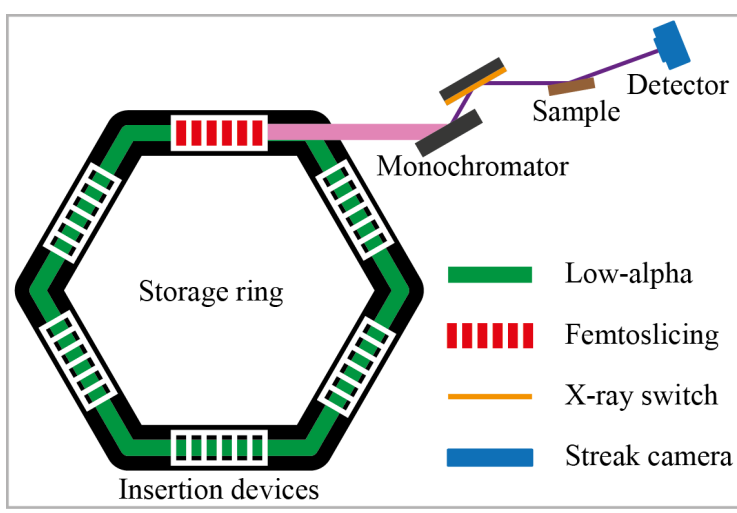

Figure 3.13: Schematic showing where different techniques/devices can be used to achieve high temporal resolution at storage rings.

Low-alpha mode

The length of an electron bunch in a storage ring is described by a momentum compaction factor, denoted alpha (α) [75]. Since the X-ray pulse duration is determined by the length of the electron bunch, one way to achieve short X-ray pulses is to reduce alpha, which means compressing the electron bunch along the longitudinal direction. This can be done by reducing the number of electrons and optimizing the operating parameters of the storage rings. In the low-alpha operation mode, the length of the electron bunch can be reduced to a few ps [76, 77].

Femtoslicing

The femtoslicing technique is based on energy modulation of the electron bunch at storage rings. It consists of three steps: energy modulation, pulse separation, and X-ray radiation [78]. In the first step, a femtosecond laser pulse copropagates with the electron bunch through an undulator/wiggler (the "modulator"). The electric field of the laser pulse induces energy modulation of the electron bunch and produces off-energy electrons in the transverse direction of the main electron bunch [79]. In the second step, dipole magnets are used to separate the main electron bunch and the off-energy electrons spatially or angularly [80]. While passing through a second undulator ("radiator"), the main electron bunch and the off-energy electrons will emit long-pulse and short-pulse radiation, respectively. Due to the spatial or angular separation, the long-pulse radiation can be blocked by apertures, while the short-pulse radiation can pass through the apertures and continue to propagate towards the sample station. Since the off-energy electrons can only be created during the femtosecond laser pulse, the short-pulse radiation will have a pulse duration of $\sim$100 fs [81–83]. The electron bunch is modulated in both the femtoslicing technique and in FELs; the difference being that the femtoslicing technique slices only a small portion electrons from the original electron bunch, whereas in FELs the whole electron bunch is modulated into micro-bunches.

X-ray switches

Low-alpha operation and the femtoslicing method produce short X-ray pulses by manipulating the electron bunches in the storage ring. This will have various effects on other beamlines at the storage ring. An X-ray switch can be implemented at a specific beamline to produce short X-ray pulses without influencing the activities at other beamlines.

An X-ray switch can be used during standard operation of a storage ring, which means normal photon flux. The principle of this device is to temporally switch the X-ray diffraction efficiency of a crystal lattice at a fixed Bragg angle using an ultrashort laser pulse [84]. Figure 3.14 shows a sketch of the gate response of an X-ray switch. At the beginning of the X-ray pulse, the crystal lattice does not match the Bragg condition, so the X-ray diffraction efficiency is suppressed and the switch is in the "OFF" state. The crystal lattice can be perturbed using a laser pulse to match the Bragg condition during a short period, during which the switch gives a gate diffraction signal ("ON" state). After the crystal lattice relaxes to its equilibrium state, the switch returns to the "OFF" state.

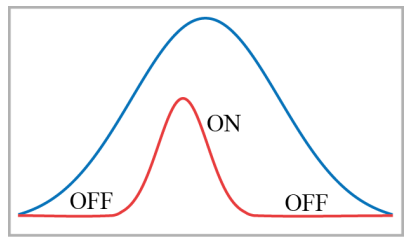

Figure 3.14: A sketch of the gate response of an X-ray switch. The blue curve represents a typical X-ray pulse, and the red curve the response curve of the X-ray switch.

The so-called PicoSwitch can be used as an X-ray switch [85]. The PicoSwitch consists of a thin transparent dielectric layer (cap layer), a thin metallic layer, and a transparent substrate [86]. A femtosecond laser pulse is used to induce a transient response in the PicoSwitch. The laser pulse energy is deposited in the metallic layer, which launches compression waves into both the cap layer and the substrate. The compression wave propagating in the cap layer will be reflected at the surface and become an expansion wave, propagating into the substrate. These waves modulate the lattice parameters of the substrate, thus temporally affecting the X-ray diffraction efficiency.

A photo-acoustic transducer has also been proposed as an X-ray switch by modulating the phonon spectrum of a semiconductor [87]. The performance of an X-ray switch based on a Au/InSb transducer (Paper III) is discussed in detail in Section 5.2.

Streak cameras

A streak camera is a fast detector that converts a short temporal signal into space. Streak cameras have been widely used over a large range of wavelengths, from the UV to the X-ray range [88–90]. The temporal resolution varies from picoseconds to attoseconds [91–95].

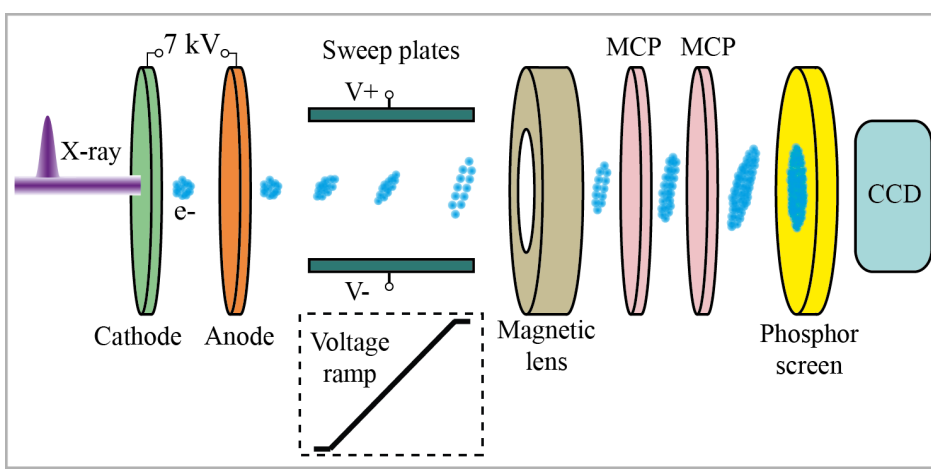

Figure 3.15: Schematic of a streak camera.

In this section, the basic principles of an X-ray streak camera, which formed part of the experimental setup described in Paper II, will be discussed. This streak camera works in the hard X-ray range, and provides a time resolution of 3 ps. Figure 3.15 shows a schematic of the streak camera. The scattered X-ray pulse excites a photo-electron bunch from a photo-cathode. This photo-electron bunch is accelerated by a high voltage, and propagates through a pair of sweep plates. A voltage ramp is applied to the sweep plates. While passing through the sweep plates, the photo-electron bunch will be deflected by the varying voltage. The electrons generated earlier will move upwards due to the negative voltage, and the electrons generated later will be deflected downwards by the positive voltage. After passing between the sweep plates, the photo-electron bunch will become streaked in space. The streaked photo-electron bunch is focused by a magnetic lens, amplified by a pair of microchannel plates (MCP) and then projected onto a phosphor screen. A CCD camera is used to capture the streaked signal.

The time resolution of the streak camera is determined by the energy spread of the photo-electron bunch. A UV beam was used to characterize the time resolution of the streak camera, as shown in Figure 3.16(a). A fused silica glass plate was inserted into the UV beam path. The refractive index of fused silica is different from that of air, thus light has different propagation times in these two media. As illustrated in Figure 3.16(a), the fused silica glass plate splits the UV beam into two parts in time, which consequently generates two photo-electron bunches and thus two spots on the phosphor screen. Figure 3.16(b) shows the lineouts of these two spots along the time axis, which corresponds to the time axis in Figure 3.16(a). The distance between the two peaks results from the difference in propagation time induced by the glass plate. The pixels on the CCD camera can then be time calibrated using the distance between the two peaks. The time resolution of the streak camera is given by the FWHM of the peaks, as shown in Figure 3.16(b).

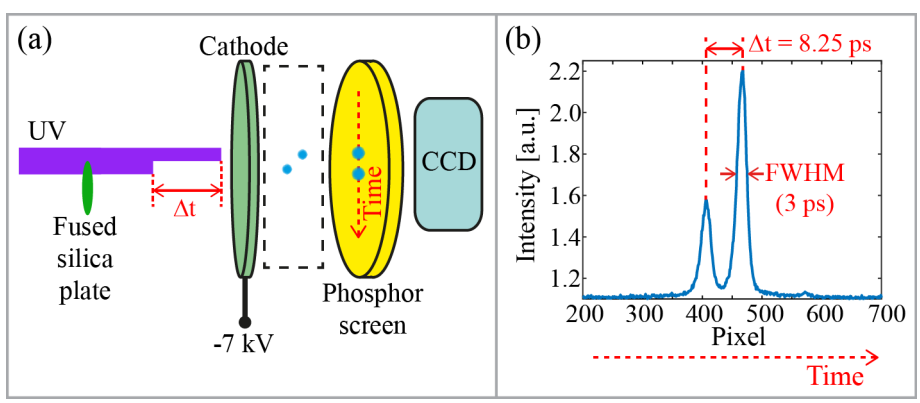

Figure 3.16: (a) Setup used to measure the time resolution of the streak camera. The dashed box omits the anode, the sweep plates, the magnetic lens, and the MCPs. (b) Estimation of the time resolution of the streak camera.

Figure 3.17 shows the X-ray diffraction signal from a laser-excited InSb crystal using the streak camera. It can be seen that dynamic information can be acquired from −50 ps to 300 ps within one X-ray pulse that has a duration of a few hundred

picoseconds.

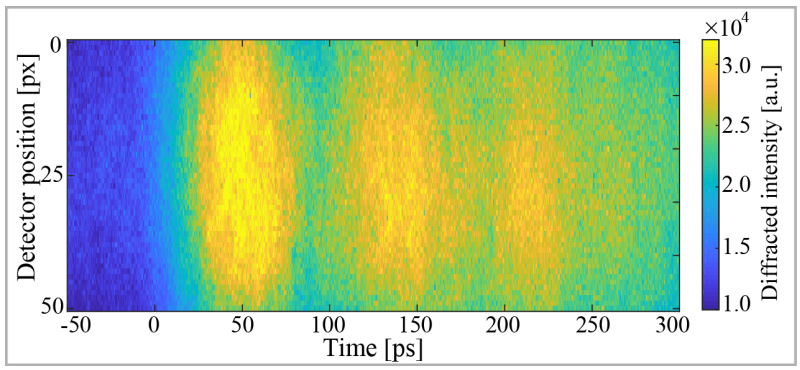

Figure 3.17: X-ray diffraction signal acquired with an X-ray streak camera.

3.3 Time-resolved electron diffraction

The maximum energy of X-rays provided by synchrotron storage rings and FELs is ∼30 keV [96]. This photon energy corresponds to a wavelength of ∼0.4 Å, which indicates a spatial resolution of the same order. A complementary method that can be used to study structural dynamics on the atomic-scale and with femtosecond resolution is time-resolved electron diffraction (TRED). In TRED experiments, the energy of the electrons can reach tens of keV using a DC voltage [16], or a few MeV using RF acceleration [17]. In this way, the wavelength of the electrons can be significantly reduced. For instance, if an electron has an energy of 3 MeV, its wavelength is only 0.4 pm, which is two orders of magnitude less than that of X-ray photons. The basic principle of electron diffraction is also described by Bragg's law. Since the wavelength of the electrons is shorter in electron diffraction experiments than in X-ray diffraction experiments, the Bragg angle will be smaller.

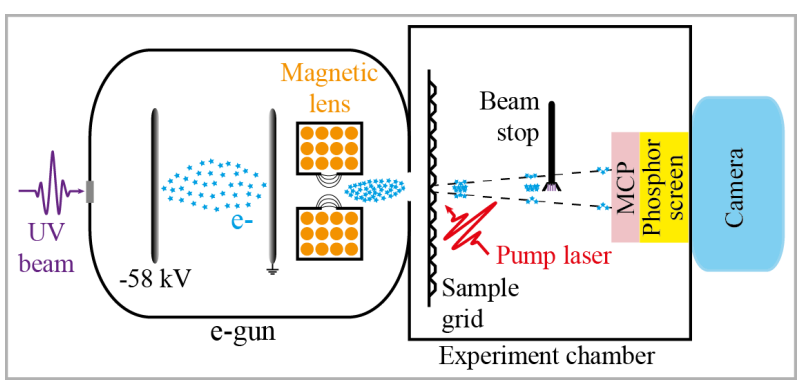

Figure 3.18: Schematic of a typical TRED setup.

Figure 3.18 shows a TRED experimental setup developed by our group [11]. The electrons are generated by a UV beam (266 nm) and accelerated by a DC voltage

(−58 kV). The electrons are then focused by a magnetic lens and propagate towards a sample grid, where multiple thin samples can be mounted. The thickness of the samples is usually tens of nm. The samples can be excited by a pump laser with a pulse duration of 40 fs. The electron beam hits the photo-excited sample and will be diffracted. The diffracted electron beam propagates towards a MCP, which amplifies the diffracted signal. The amplified electron signal is projected onto a phosphor screen, and the diffraction pattern on the phosphor screen is captured by a camera. A beam stop is mounted between the sample grid and the MCP in order to block the direct beam while applying high voltages to the MCP and the phosphor screen. The number of electrons per pulse is ∼1500, which gives a pulse duration of <400 fs [97]. A delay stage (not shown in Figure 3.18) is used to vary the difference in arrival time between the UV beam and the pump beam.

Figure 3.19 shows a diffraction image acquired from a natural graphite sample using the setup illustrated in Figure 3.18. The letters A-E denote the (100) reflection with six-fold symmetry, which arises from the hexagonal lattice structure of graphite (Figure 2.6(b)). The sixth diffraction spot is blocked by the beam stop.

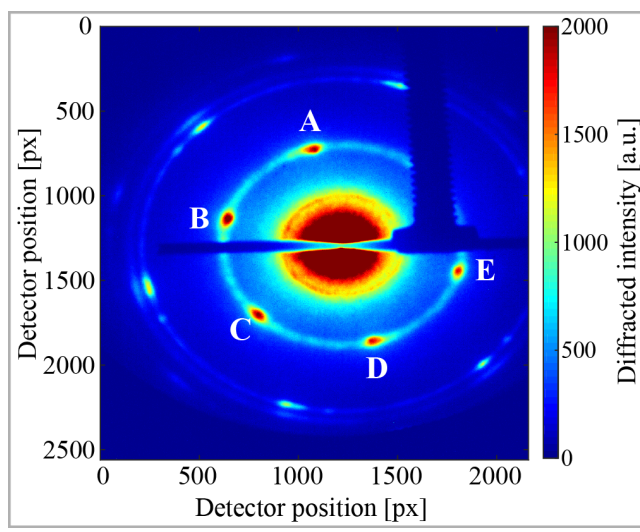

Figure 3.19: Electron diffraction pattern from a natural graphite sample.

When setting up a TRED experiment, it is critical to identify time zero, at which the laser (pump) beam and the electron (probe) beam arrive at the sample position at the same time. A copper grid is used to define time zero. The images of the electron beam transmitted from the copper grid without and with laser excitation are shown in Figure 3.20(a) and 3.20(b), respectively. The transmitted electron beam becomes blurred as a result of laser excitation (Figure 3.20(b)), compared to the unperturbed electron beam (Figure 3.20(a)). This is because the copper grid emits electrons upon laser excitation. These electrons will deflect the electron beam that is generated by the UV beam [98, 99]. The copper grid can be clearly seen in Figure 3.20(c), after subtracting Figure 3.20(a) from Figure 3.20(b). The interaction between the emitted electrons and the UV-generated electron beam contributes to the positive intensity in Figure 3.20(c).

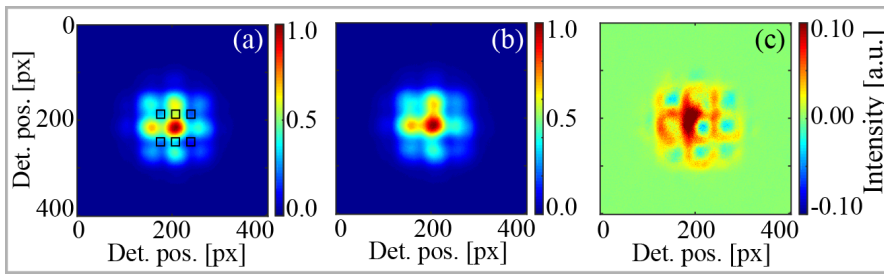

Figure 3.20: Images of the electron beam transmitted from a copper grid: (a) without laser excitation; (b) with laser excitation. The difference image in (c) is obtained after subtracting (a) from (b).

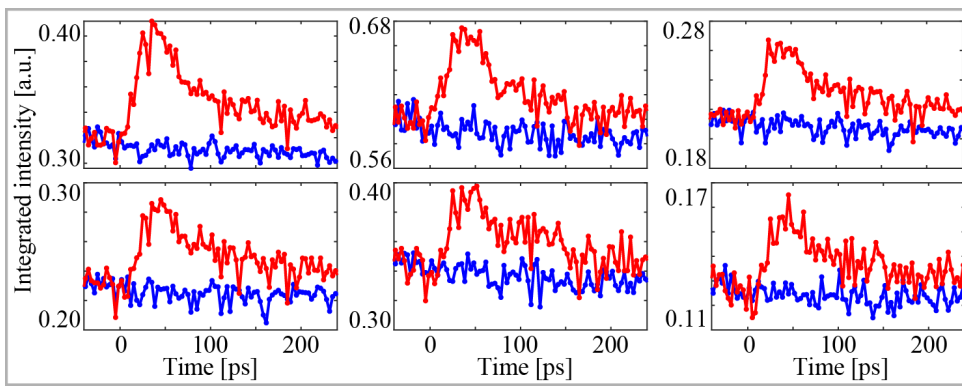

Figure 3.21: A delay scan of the integrated intensity in the selected areas shown in Figure 3.20(a). Red and blue curves correspond to the images acquired with and without laser excitation, respectively.

In order to follow the dynamic response of the copper grid, a delay stage was used to make a time scan and acquire a series of images. Six areas were selected in each image, and the intensity of each area was integrated. The six areas are indicated by the black squares in Figure 3.20(a). The variation in intensity is shown as a function of time in Figure 3.21. All six areas selected in the images acquired with laser excitation gave a rise time of ∼20 ps (the red curves). Laser-induced blurring lasted for ∼100 ps, which can also be seen in Figure 3.21. Thus, time zero can be estimated with a precision of a few picoseconds using the copper grid. In an actual experiment, time zero can be determined more accurately by monitoring the response of the sample upon laser excitation.

Chapter 4

Modelling & Simulations

In this chapter, the models used to explain the experimental results included in this thesis will be discussed. Two sets of simulation codes that can be used to reproduce the strain profile after ultrashort laser excitation are introduced. In the last section of this chapter, a diffraction code is introduced, and some applications related to the work described in this thesis are discussed.

4.1 Two-temperature model

The modification of the phonon spectrum and the generation of pressure waves were discussed in Chapter 2. Both of these are related to the generation and propagation of strain in solids. To interpret the mechanism of strain generation, a model called the two-temperature model is used to simulate the evolution of the temperature and the strain in solids.

The two-temperature model treats the lattice and the electrons as two systems. The laser pulse energy is first deposited in the electron system, which takes place within the laser pulse duration, on the femtosecond time scale. The temperature of the electron system increases rapidly, by thousands of Kelvins, depending on the excitation fluence. The heat energy from the electron system is then transferred to the lattice system via electron-phonon scattering processes [100, 101]. The electron system and the lattice system will reach thermal equilibrium on the time scale of ∼10 ps. Eq. 4.1 describes the temperature evolution of the electron system and the lattice system:

$$\begin{cases} A_e T_e \dfrac{\partial T_e(t,z)}{\partial t} = \dfrac{\partial}{\partial z}\left(k_e \dfrac{T_e}{T_l}\dfrac{\partial T_e(t,z)}{\partial z}\right) - G \times (T_e(t,z) - T_l(t,z)) + S(t,z) \\ C_l \dfrac{\partial T_l(t,z)}{\partial t} = G \times (T_e(t,z) - T_l(t,z)) \end{cases} \tag{4.1}$$

In Eq. 4.1, A_e and C_l denote the electronic heat capacity and the lattice heat capacity, T_e and T_l are the electron temperature and the lattice temperature, k_e is the electronic thermal conductivity, and G is the electron-phonon coupling factor. $S(t,z)$ is the initially deposited laser power per unit volume as a function of time t and depth z,

and is defined as:

$$S(t,z) = \frac{F_{abs}}{\tau_p \zeta} e^{-\frac{z}{\zeta}} e^{-\frac{t^2}{\tau_p^2}} \tag{4.2}$$

where F_{abs} is the absorbed laser fluence, τ_p is the laser pulse duration, and ζ is the optical absorption depth. The simulation codes used in this work are one-dimensional codes.

A toolbox called udkm1Dsim was used to simulate the strain profile and the transient X-ray diffraction efficiency [102, 103] in experiments with low laser excitation fluence, i.e., below the damage threshold of the samples. The udkm1Dsim toolbox implements the two-temperature model, and it can simulate the temperature evolution in one-dimensional crystalline structures after laser excitation. After obtaining the temperature profile of the crystal structures, the thermal strain can be calculated using the linear thermal expansion coefficient.

Figure 4.1 shows an example of the temperature evolution in a Ni film simulated with the udkm1Dsim toolbox. The lineouts represent the temperature evolution of the electron system and the lattice system of a Ni film with an excitation fluence of 4 mJ/cm^2. It can be seen that the electron temperature increases instantaneously to ∼1800 K after laser excitation, while the lattice temperature remains at room temperature. The electron temperature then decreases to ∼500 K within the first 5 ps, during which time the lattice temperature starts to increase, and the two systems reach thermal equilibrium.

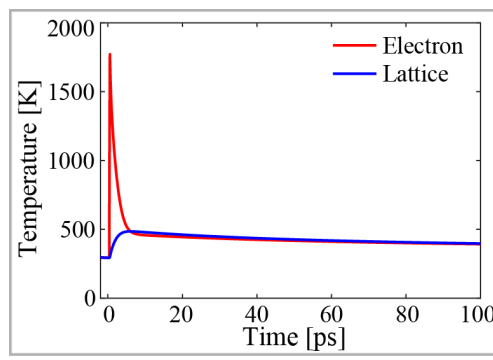

Figure 4.1: The evolution of the electron temperature and the lattice temperature of a Ni film after laser excitation. The absorbed laser fluence is 4 mJ/cm^2.

It can be seen from Eq. 4.1 that the electron-phonon coupling factor, G, plays an important role in the transfer of energy from the electron system to the lattice system. It can be used to describe the electron diffusion in metallic films. A small electron-phonon coupling factor means the energy will be retained in the electron system for a longer time, and the electrons can diffuse further into the material (strong electron diffusion). A large electron-phonon coupling factor, on the other hand, means that the energy will be transferred rapidly from the electron system to the lattice system, i.e., weak electron diffusion. Figure 4.2 shows the results of simulations of electron diffusion in a Ni film using the two-temperature model with two different electron-phonon coupling factors, where it can be seen that the electron diffusion is stronger

with a smaller electron-phonon coupling factor (Figure 4.2(a)) than with a higher electron-phonon coupling factor (Figure 4.2(b)).

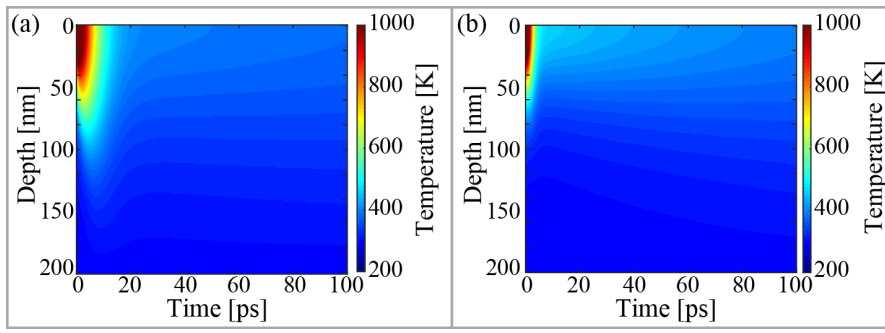

Figure 4.2: Electron temperature evolution of a Ni film after laser excitation with an electron-phonon coupling factor of (a) $G = 9 \times 10^{16}$ W/(m$^3\cdot$ K) , and (b) $G = 36 \times 10^{16}$ W/(m$^3\cdot$ K). The absorbed laser fluence is 4 mJ/cm^2.

4.2 Hydrodynamic simulation

The udkm1Dsim toolbox can only solve the temperature evolution of the structures when they are in the solid state. It cannot handle structural changes that involve solid-to-liquid transitions. In this case, a one-dimensional hydrodynamic code (ESTHER) can be used to simulate the response of the crystal structures when the laser excitation fluence is above the damage threshold of the material [104, 105]. This hydrodynamic code uses the two-temperature model to determine the temperature profile of the electron system and the lattice system, and solves the evolution of the mass density of the materials [106].

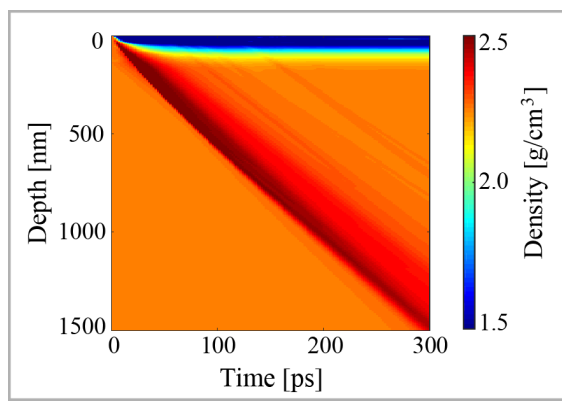

Figure 4.3: Evolution of mass density of a graphite crystal after laser excitation with a fluence of 400 mJ/cm^2.

Figure 4.3 shows the mass density evolution of a graphite crystal with an excitation fluence of 400 mJ/cm^2, which is above the damage threshold (185 mJ/cm^2) [107].

It can be seen that the upper layer (∼50 nm, shaded blue) is ejected after laser excitation, resulting in a density lower than the normal density of graphite. The orange area corresponds to the normal density of graphite (2.26 g/cm^3), and the red area indicates the compressed region of the graphite crystal.

The change in mass density will result in a variation in the volume, which, in the one-dimensional case, is the change in length (strain). Therefore, the strain map can be extracted from the mass density map, as shown in Figure 4.4. The strain in the surface layer is positive, which corresponds to the ejection of the upper layer. The blue shaded region in Figure 4.4 represents negative strain, or compressive strain. It can be seen that compressive strain propagates in the graphite lattice as a function of time. Moreover, the slope of the blue area indicates the velocity of the pressure waves. The hydrodynamic simulations are compared with the experimental results for an Al/InSb transducer and a natural graphite crystal in Chapter 5, in order to provide a detailed understanding of pressure wave generation and evolution.

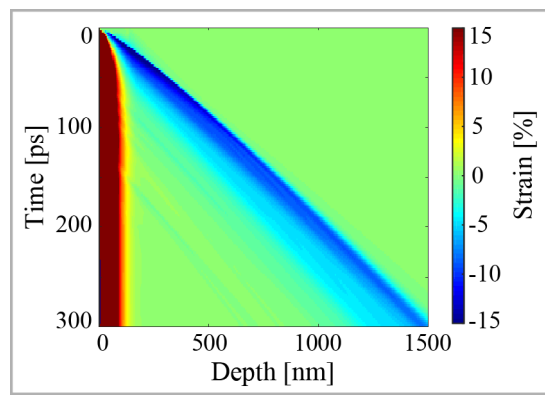

Figure 4.4: Evolution of strain in a graphite crystal after laser excitation with a fluence of 400 mJ/cm^2.

4.3 Two-dimensional diffraction patterns

For phonon studies, it is possible to focus on only one Bragg reflection, and measure the variation in intensity within the vicinity of the Bragg peak as a function of time. However, for large-amplitude strain wave studies, the internal pressure (stress) has the potential to induce lattice rearrangement or disordering. Therefore, it is necessary to cover a large portion of reciprocal space in order to capture the occurrence of new Bragg peaks or the disappearance of existing ones. In this case, a large detector is usually used to acquire two-dimensional diffraction patterns. A diffraction code was used in this work to simulate the two-dimensional diffraction patterns of single crystalline structures [108].

In Section 3.1.2, it was pointed out that the azimuth rotation is important for non-coplanar reflections in order to fulfil Bragg's law. It is impossible to observe all the allowed Bragg reflections without azimuth rotation of the single crystalline sample. The two-dimensional diffraction code used in this work has no constraints regarding the azimuth angle. Therefore, it is able to calculate all the allowed Bragg reflections

based only on the structure factors, and provides the azimuth angle as an output. This is convenient for experiments, as it is easy to find different reflections by comparing their azimuth angles.

Figure 4.5 shows a comparison between the simulated results and an experimental diffraction image from a highly oriented pyrolytic graphite (HOPG) sample. This sample has different single crystalline grains. All these grains have the same surface normal ([001]) but different azimuth orientations [109]. Due to the multiple azimuth orientations, all the allowed Bragg reflections can be seen. The blue dots were generated by the diffraction code, and they coincide well with the experimental results, indicated by the yellow spots. The white dashed lines represent the q values of graphite. The q values are defined as:

$$q = \frac{4\pi}{\lambda} \cdot \sin\theta \tag{4.3}$$

where λ is the wavelength of the incident X-ray beam, and θ is the scattering angle of the Bragg reflections. The diameter of the q circles on the detector is defined by the q values and the distance between the sample and the detector. Therefore, the q values can be used to calibrate the sample–detector distance in experiments.

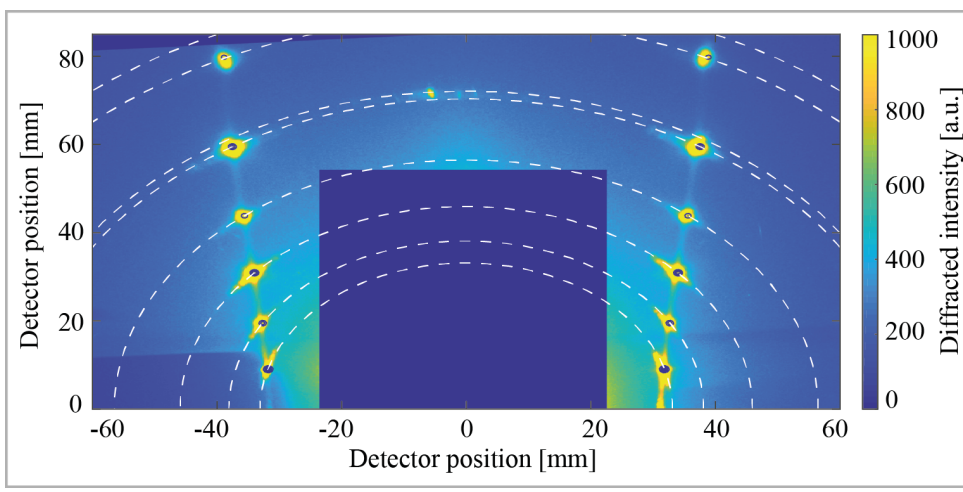

Figure 4.5: Comparison between the simulated pattern and the experimental diffraction pattern of a highly oriented pyrolytic graphite sample. The bright yellow spots indicate the experimental patterns. The blue dots were generated by the diffraction code, and the white dashed lines represent the q values of graphite.

The diffraction code requires the atomic positions and lattice constants as input. The two-dimensional diffraction pattern will change if the basic parameters of crystal lattice deviate from their normal values. Therefore, the diffraction code can be used to investigate the structural changes in a crystal lattice.

Figure 4.6 shows the two-dimensional diffraction patterns from a perfect graphite lattice and a strained graphite lattice with 10% compression along the [001] axis. The Miller indices of the diffraction spots are $(10l)$ ($l = 0, 1, 2, 3$) from the bottom to the top. The mirror symmetry of the diffraction spots is due to the six-fold symmetry of the hexagonal lattice system. It can be seen in Figure 4.6(a) that all the diffraction spots for the perfect graphite lattice fall on the q rings, which correspond to the static

$(10l)$ (l = 0, 1, 2, 3) Bragg reflections. When the [001] axis of the graphite lattice is compressed by 10%, the diffraction spots deviate from the static q rings, as can be seen in Figure 4.6(b). This is because when the lattice is compressed, the scattering angle will increase to fulfil Bragg's law (Eq. 3.1). According to Eq. 4.3, the q value for the compressed lattice will increase as the scattering angle increases, and the diffraction spots deviate upwards in Figure 4.6(b).

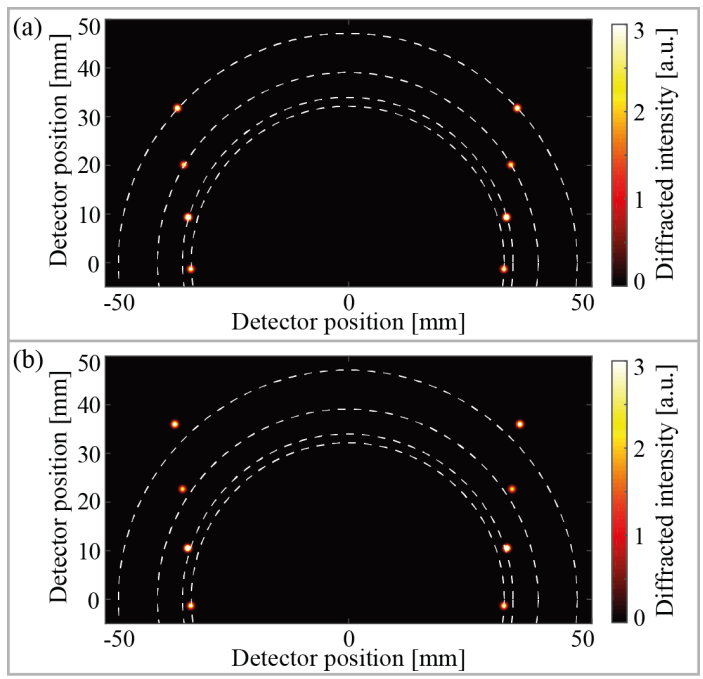

Figure 4.6: Diffracted intensity from a graphite crystal: (a) with no strain; (b) with 10% compressive strain.

Figure 4.6 shows the results with a constant strain component, but a set of variable strain components can be used in the diffraction code to monitor the change in the diffraction pattern. Figure 4.7(a) shows the two-dimensional diffraction pattern from a graphite crystal with the linear strain profile illustrated in Figure 4.7(b). It can be seen in Figure 4.7(a) that the linear strain profile induces a streak in the diffraction pattern. The streak becomes more elongated for Bragg reflections with higher q values. For the graphite lattice, the d spacing for the $(10l)$ family is given by:

$$\frac{1}{d_{10l}^2} = \frac{4}{3} \cdot \frac{h^2 + hk + k^2}{a_1^2} + \frac{l^2}{a_3^2} = \frac{4}{3a_1^2} + \frac{l^2}{a_3^2} \tag{4.4}$$

where a_1 and a_3 are lattice constants, and $h = 1$, $k = 0$ and l are the Miller indices. From Eq. 4.4, it can be seen that the Bragg reflection with a higher value of l is more sensitive to changes in the lattice constant a_3, which is consistent with the streaks in Figure 4.7(a). Since the streak for the (103) reflection is much longer than that for the (100) reflection, better resolution can be obtained by analyzing the (103) reflection. The diffraction code has been used together with hydrodynamic simulations

to characterize the pressure waves in graphite upon intense laser excitation (see Section 5.4).

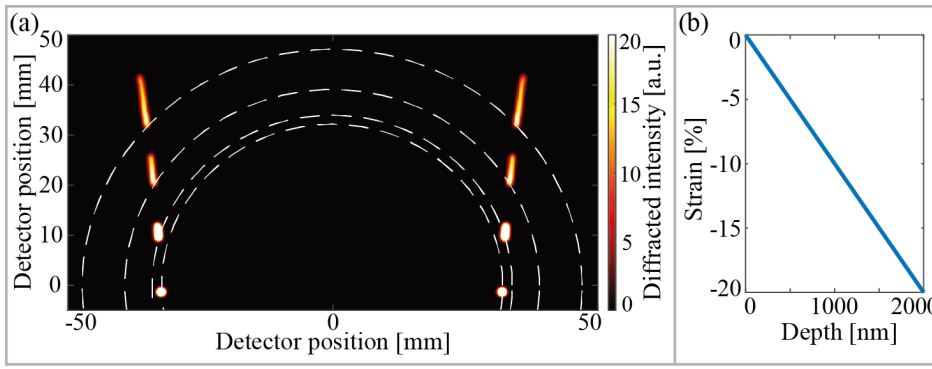

Figure 4.7: (a) Diffracted intensity from a graphite crystal, with a linear strain profile as shown in (b).

Chapter 5

Results

In this chapter, the main results of the five experiments in which different structural dynamics in solids were studied, are presented. These five experiments can be divided into two categories. The first two experiments were carried out with a laser excitation fluence below the damage threshold of the samples. The electron diffusion in a Ni film was studied, and the performance of a Au/InSb X-ray switch was characterized. The third and the fourth experiments were performed with a laser excitation fluence higher than the damage threshold of the samples. In these two experiments, pressure waves were studied in an Al/InSb transducer and a graphite crystal. The last experiment was also carried out with a laser excitation fluence above the damage threshold. In this experiment, non-thermal melting in InSb was studied, and the potential use of non-thermal melting as a timing monitor is discussed.

5.1 Electron diffusion in nickel

This experiment was carried out to investigate how electron diffusion modifies the heat deposition profile in a Ni film after irradiation with femtosecond IR laser pulses (Paper II). The tabulated optical absorption depth in Ni is 17.6 nm for a laser wavelength of 800 nm [110]. The energy deposition depends on the electron diffusivity and the electron-phonon coupling. Therefore, the two-temperature model was used to interpret the experimental results and to characterize the electron diffusion in the Ni film.

This experiment was carried out at the D611 beamline at the MAX II storage ring. The experimental setup is shown in Figure 5.1. The sample consisted of a 150-nm Ni film coated on a 525-μm InSb substrate. A Ti:sapphire laser was employed to provide ultrashort laser pulses with a duration of 43 fs, at a central wavelength of 800 nm. The pulse energy of the laser was 2.4 mJ, at a repetition rate of 4.25 kHz. The laser beam was split into three parts: the first part was used to excite a photo-conductive switch (PC switch) to trigger the detector (streak camera), the second part was passed through a tripling stage to generate UV light that was used for time calibration, and the third part was used as the pump beam to excite the sample. The laser excitation fluence was 4 mJ/cm^2. The sample was probed using X-ray pulses with a duration of 600 ps at a photon energy of 4.5 keV. The diffracted X-ray signal was acquired in a streak camera with a time resolution of 3 ps.

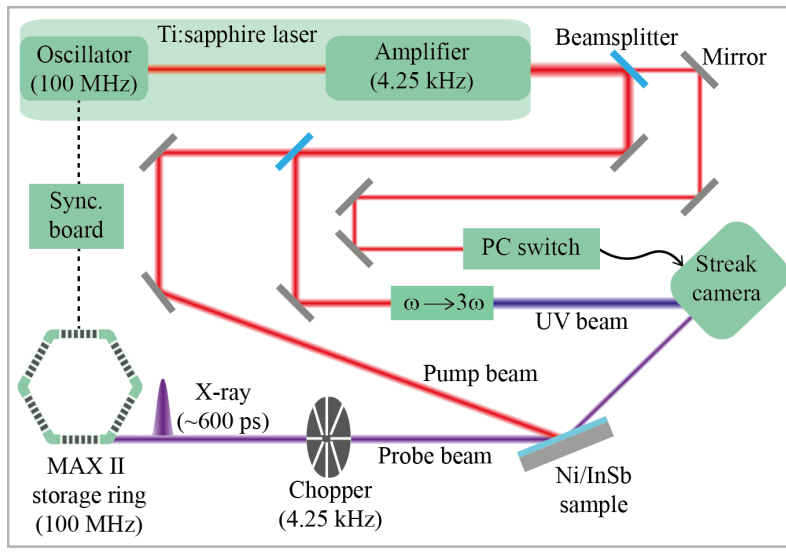

Figure 5.1: Schematic of the experimental setup used to investigate electron diffusion in a Ni film.

The relative intensity was obtained by dividing the diffracted X-ray intensity with laser excitation by that without laser excitation, as shown in Figure 5.2(a). The experimental data shown in Figure 5.2(a) are the average of four measured datasets, and each dataset contained 400 000 X-ray pulses. The standard deviation of the four measured datasets was used as the experimental error. Since the strain wave travels at the longitudinal speed of sound, it takes 25 ps for the strain waves to propagate through the Ni film. Therefore, the decrease in the X-ray reflectivity starts after 25 ps. Two models were used to simulate the strain generation in order to interpret the initial decrease in the experimental data. In the first model, a tabulated optical absorption depth of 17.6 nm [110] was used to describe the energy deposition profile based on the Thomsen model without considering electron diffusion. As can be seen in Figure 5.2(a), the results obtained with this model (dotted blue curve) do not agree with the experimental data, as the initial decrease is steeper than that observed experimentally. The two-temperature model, which was used as the second model, provides a much better fit (dashed red curve) to the experimental data with the same optical absorption depth. The electron-phonon coupling factor was defined as a free parameter, and the best fit was obtained at a value of 9×10^{16} W/(m$^3\cdot$ K).

The amplitude of the strain pulse can be extracted from the derivative of the X-ray reflectivity on the short time scale and for sufficiently small strains. A short time scale means the period of the initial decrease in the X-ray reflectivity (∼30 ps), and sufficiently small strain means that the change in X-ray reflectivity is approximately linear with strain. Figure 5.2(b) shows the strain pulse obtained experimentally and from simulations. The simulation without electron diffusion predicts a narrow strain pulse, while the two-temperature model provides a broader strain pulse, in better agreement with the experimental data. This means the heat deposition profile expands deeper into the material, as illustrated in Figure 5.3. When the Ni film is illuminated by

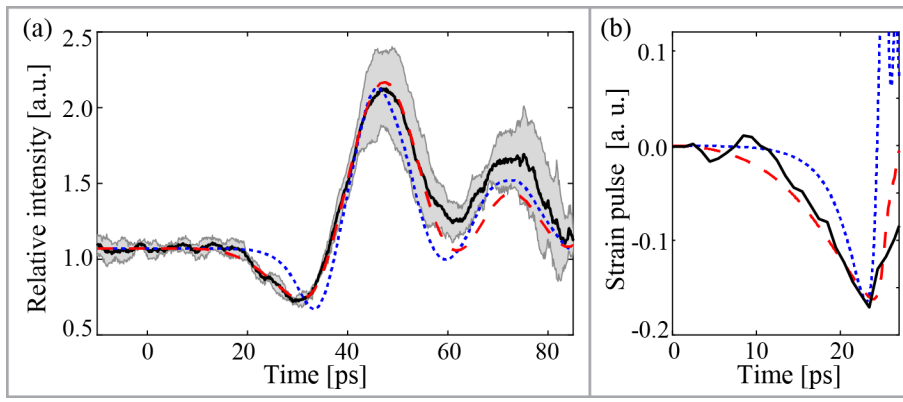

Figure 5.2: (a) Normalized X-ray reflectivity as a function of time. The experimental data are represented by the solid black curve, and the gray shaded area shows the experimental error. The dotted blue curve shows the results of the simulation without electron diffusion. The dashed red curve shows the simulation obtained with the two-temperature model. (b) Strain pulse amplitude extracted from the derivative of the normalized X-ray reflectivity (solid black curve). The dotted blue curve shows the derivative of the simulated reflectivity obtained without considering electron diffusion, and the dashed red curve that obtained from the two-temperature model (Paper II).

a femtosecond laser pulse, the energy is first deposited within the optical absorption depth, as shown in Figure 5.3(a). During relaxation of the electron-phonon scattering, the diffusive motion of the hot electrons transfers the energy beyond the optical absorption depth, as shown in Figure 5.3(b).

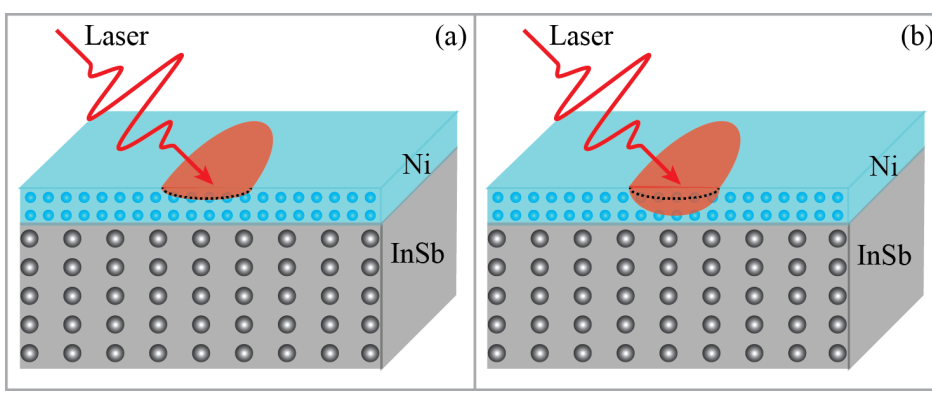

Figure 5.3: Illustration of heat deposition in Ni film after laser excitation without electron diffusion (a), and the two-temperature model (b). The black dotted line in (b) indicates the same depth in (a).

This experiment thus showed that TRXD can be used to study the electron diffusion in a metallic film, and to characterize the electron-phonon coupling factor together with the two-temperature model.

5.2 Modification of the phonon spectrum: an X-ray switch

In this section, a photo-acoustic transducer with the ability to reduce the pulse duration of the X-ray pulse to 20 ps is described (Paper III). This experiment was carried out at the FemtoMAX beamline at the MAX IV Laboratory. The experimental setup is shown in Figure 5.4.

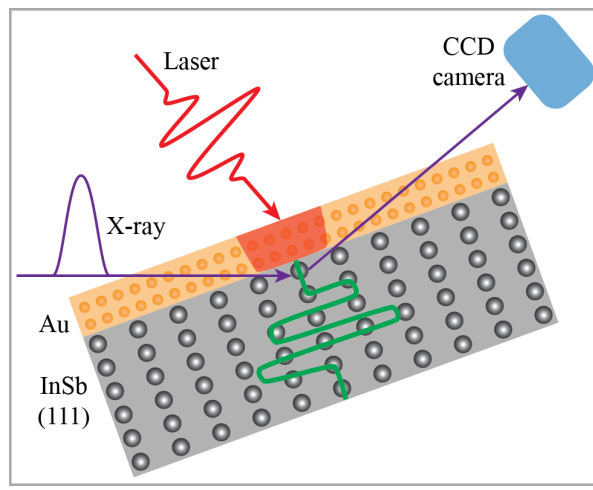

Figure 5.4: Schematic of the experimental setup used in the Au/InSb X-ray switch experiment. The red shaded area in the Au film indicates the energy deposition volume of the laser pulses, and the green curve represents the strain wave propagating through the InSb substrate.

The sample consisted of a 60-nm Au film coated on an InSb substrate. The sample was illuminated with laser pulses with a duration of 60 fs, at a central wavelength of 800 nm. The angle of incidence of the laser beam was 50°. The dynamic processes taking place in the InSb substrate were probed using X-ray pulses with a duration of 2 ps. The angle of incidence of the X-ray beam was 19.32°. A CCD camera was used to measure the X-ray diffraction efficiency of the InSb (111) crystalline plane at different time delays between the laser pulse and the X-ray pulse.

The two-temperature model was used to simulate the strain generation in the Au/InSb transducer. Upon laser excitation, the energy of the laser pulse is deposited in the electron system of the Au film. Due to the weak electron-phonon coupling in Au, the energy deposition profile is almost uniform throughout the whole film thickness, and the Au film is heated uniformly through its entire thickness. This heating leads to a uniform stress, which is released by thermal expansion of the Au film. A compressive strain wave is thus generated, which propagates into the InSb substrate. At the same time, two expansion waves are generated at the vacuum/gold interface and the gold/InSb interface, respectively. Figure 5.5(a) shows the compression component in the InSb substrate, and the two expansion strain waves in the Au film at a time delay of 5 ps after laser excitation. These two expansion waves counter-propagate in the Au film and are reflected multiple times at the interfaces. The multiple reflections of the expansion strain waves create a series of strain echoes in the InSb substrate. Figure

5.5(b) and 5.5(c) show the travelling strain echoes at time delays of 150 ps and 250 ps, respectively. The red arrow in Figure 5.5(c) indicates one period of the strain echoes.

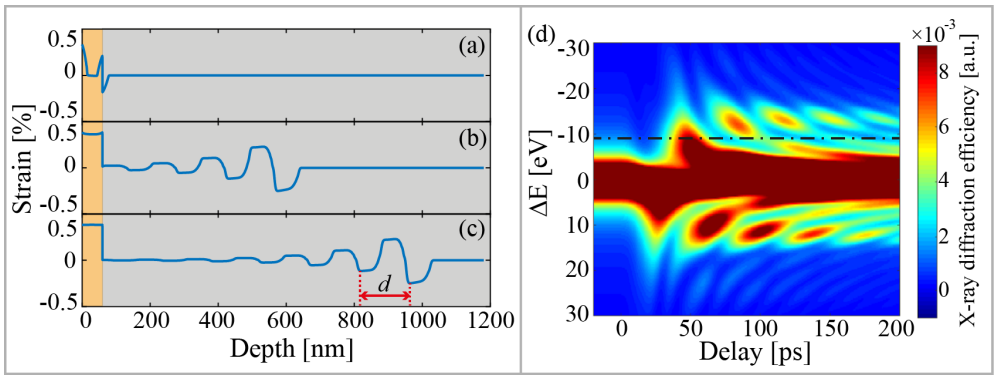

Figure 5.5: Strain profile at different time delays: (a) 5 ps, (b) 150 ps, (c) 250 ps. The gold shaded area indicates the Au film and the gray shaded area the InSb substrate. The periodicity of the strain echoes is 145 nm, indicated by the red arrow in (c). The X-ray diffraction efficiency is shown as a function of time and energy offset in (d). The dot-dashed line indicates the energy offset (−8.2 eV) required to obtain an isolated peak along the time axis in the X-ray diffraction curve. The absorbed laser fluence was 4 mJ/cm^2. The thickness of the Au film was 60 nm.

The TRXD efficiency can be calculated from the strain profile as a function of time and energy offset, and is shown in Figure 5.5(d). The X-ray diffraction efficiency has an isolated peak along the time axis at an energy offset of −8.2 eV, as indicated by the dot-dashed line in Figure 5.5(d), while oscillations after this peak are suppressed. The TRXD efficiency of the Au/InSb switch obtained from both experimental measurements (solid black curve) and the two-temperature model (dot-dashed red curve) is shown in Figure 5.6(a). The experimental data were measured at an energy offset of −8 eV. A sharp peak was observed at a time delay of 50 ps, and the FWHM of this peak was 20 ps. The TRXD efficiency at the peak was 8%. As can be seen from this figure, good agreement was obtained between the experimental data and the simulation. To illustrate the application of the Au/InSb switch, the experimental X-ray diffraction curve was multiplied by a Gaussian profile with a pulse duration of 100 ps. The Gaussian profile and the resulting curve are shown in Figure 5.6(b). This means that the incoming 100-ps Gaussian pulse could be reduced to 20 ps at a time delay of 50 ps after laser excitation. The performance of an X-ray switch is usually characterized by two factors: the temporal response and the temporal contrast. The temporal response is given by the FWHM of the X-ray diffraction curve. The temporal contrast is defined as:

$$C_{0,\infty} = \frac{\eta_{max} - \eta_{0,\infty}}{\eta_{0,\infty}} \tag{5.1}$$

where η is the X-ray diffraction efficiency, and the subscripts 0, ∞ and max denote $before$, $after$ and at the $maximum$ of the peak, respectively. The temporal contrast of the Au/InSb switch proposed here is $C_0 = 9$ and $C_\infty = 4$.

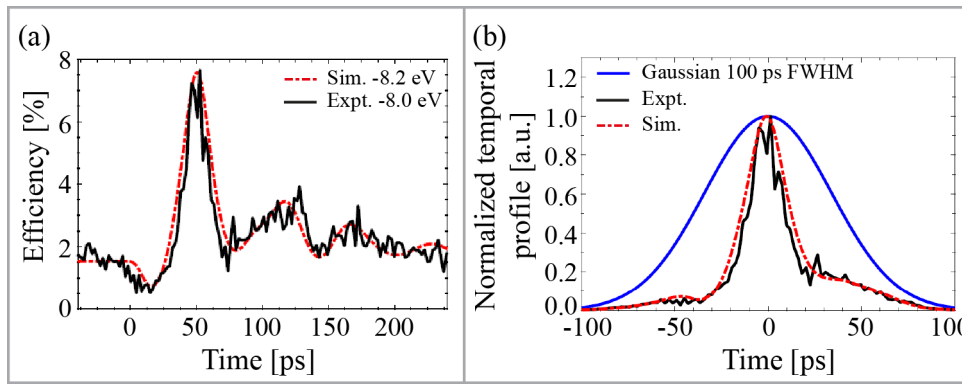

Figure 5.6: (a) The TRXD efficiency obtained experimentally (solid black curve) and from simulation (dot-dashed red curve). (b) Multiplication of the TRXD curve with a 100-ps Gaussian pulse (Paper III).

The film thickness influences the energy offset of the first cancellation in the phonon spectrum, so a faster switch with a shorter temporal response can be obtained by reducing the film thickness. However, this will reduce the temporal contrast. Figure 5.7 shows the results of a simulation for a Au/InSb switch with a film thickness of 35 nm. The periodicity of the strain echoes is 85 nm (Figure 5.7(a)-(c)), which is shorter than that in Figure 5.5(a)-(c). The strain echoes in Figure 5.7 have a saw-tooth profile, in contrast to the top-hat profile in Figure 5.5. The first cancellation is seen at an energy offset of -15.2 eV, with a peak width of 15 ps (FWHM) in Figure 5.7(d), which is slightly faster than that in Figure 5.5(d). However, the temporal contrast is reduced to $C_0 = 4$ and $C_\infty = 1.5$. The performance of the Au/InSb switches with film thicknesses of 60 nm and 35 nm is given in Table 5.1.

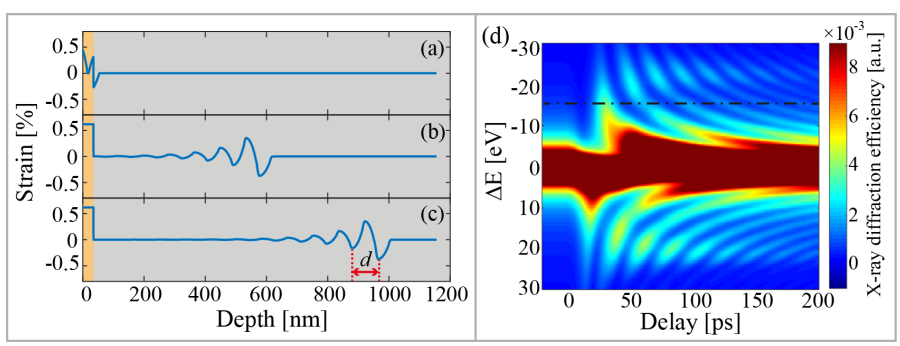

Figure 5.7: Strain profile at different time delays: (a) 5 ps, (b) 150 ps, (c) 250 ps. The gold shaded area indicates the Au film and the gray shaded area the InSb substrate. The periodicity of the strain echoes is 85 nm, indicated by the red arrow in (c). The X-ray diffraction efficiency is shown as a function of time and energy offset in (d). The dot-dashed line indicates the energy offset (-15.2 eV) required to obtain an isolated peak along the time axis in the X-ray diffraction curve. The absorbed laser fluence was 4 mJ/cm^2. The thickness of the Au film was 35 nm.

Table 5.1: The performance of the Au/InSb switch with two film thicknesses.

Thickness [nm]	Fluence [mJ/cm^2]	Temporal response [ps]	Temporal contrast C_0	Temporal contrast C_∞
60	4.0	20	9	4
35	4.0	15	4	1.5

This experiment was part of the commissioning of the FemtoMAX beamline, and the experimental X-ray diffraction efficiency curve was the first time scan obtained at this beamline. This experiment validated the instrument design of the FemtoMAX beamline.

5.3 Generation of pressure waves in an Al/InSb transducer

The laser excitation fluence in the experiments discussed in Sections 5.1 and 5.2 was below the damage threshold of the metallic films. When the fluence is above the damage threshold, the metallic film can be melted, and a pressure wave can be generated by the molten layer due to the change in density. This section describes the characterization of the pressure wave generated in an Al/InSb transducer (Paper IV). This experiment was conducted at beamline ID09 at the European Synchrotron Radiation Facility. The experimental setup used is illustrated in Figure 5.8.

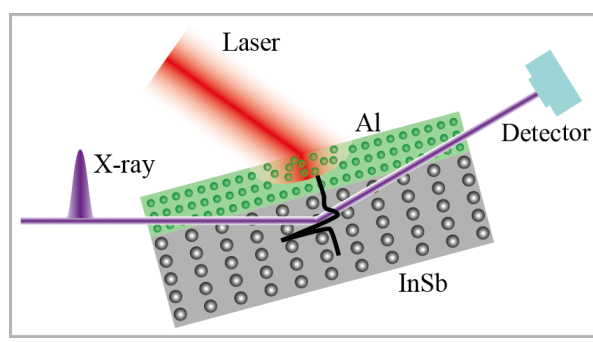

Figure 5.8: Schematic of the experimental setup used to characterize the pressure wave in an Al/InSb transducer.

The sample consisted of a 300-nm Al film deposited on an InSb substrate with (111) symmetrically cut geometry. A Ti:sapphire laser, with a central wavelength of 800 nm and a pulse duration of 1.2 ps, was used to excite the Al film at an angle of incidence of 74° (p-polarized). The reflectivity of Al at 800 nm was found to be 60% at this angle of incidence for p-polarized light. During the experiment, the incident fluence was set to 120 mJ/cm^2, which means that the absorbed fluence was 48 mJ/cm^2. This is above the melting threshold of Al, which has been reported to be in the range of 5 mJ/cm^2 to 20 mJ/cm^2 [16, 111, 112]. Therefore, the top layer of the Al film was melted. The melting of the top layer of the Al film launches a pressure wave that propagates into the InSb substrate, as illustrated by the black curve in Figure 5.8.

The pressure wave was probed with X-ray pulses with a photon energy of 15 keV and a pulse duration of 100 ps. The angle of incidence of the X-rays was set to $\theta_B = 6.35°$, which is the Bragg angle of the InSb (111) reflection at 15 keV. The X-ray diffraction pattern of the sample was captured with a 2D detector. This experiment was carried out in coplanar geometry.

In order to characterize the pressure wave, the X-ray reflectivity of the InSb (111) reflection was measured at different angles of incidence with and without laser excitation. It can be seen from Figure 5.9 that, on the right side of the Bragg peak, the X-ray reflectivity with laser excitation is higher than that without laser excitation. According to Bragg's law, a larger angle of incidence corresponds to a smaller d spacing, at a fixed X-ray wavelength. Therefore, the increased intensity with laser excitation seen in Figure 5.9 means that a compressive pressure wave was generated due to the melting of the Al film. On the left side of the Bragg peak, the X-ray reflectivity with laser excitation is similar to that without laser excitation, which means there is no expansion component associated with the pressure wave.

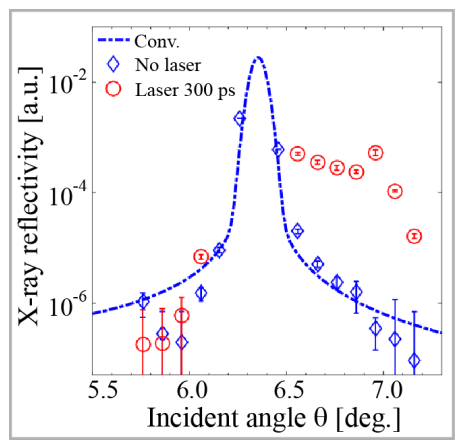

Figure 5.9: X-ray reflectivity of InSb measured at different angles of incidence of the X-rays. The blue diamonds represent the measurement that was done without laser excitation, and the dot-dashed blue curve shows the theoretical reflectivity curve convoluted with the instrumental function. The red circles represent the X-ray reflectivity that was measured with laser excitation at a time delay of 300 ps.

In order to determine the profile of the pressure wave, the hydrodynamic code ESTHER (see Section 4.2) was used to simulate the evolution of the density of the Al film after laser excitation. Figure 5.10 shows the mass density map of the Al film as a function of time and depth with a laser excitation fluence of 42 mJ/cm^2. It can clearly be seen that the top layer (∼50 nm) of the Al film is melted after 10 ps, as illustrated by the red arrow. The yellow area in Figure 5.10 represents a density greater than the tabulated solid density of Al (2.7 g/cm^3), which indicates compression of the Al film. The compression changes with time, which indicates a propagating pressure wave in the Al film.

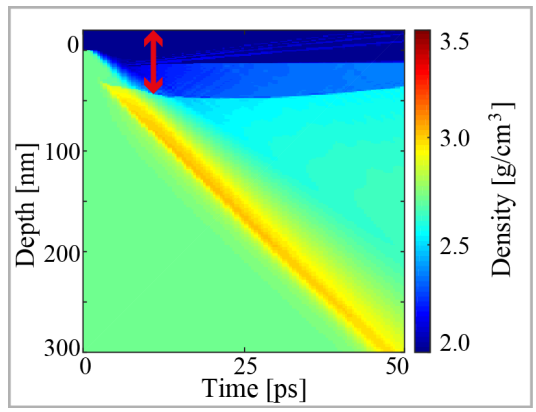

Figure 5.10: Evolution of the mass density of the Al film after laser excitation with a fluence of 42 mJ/cm^2.

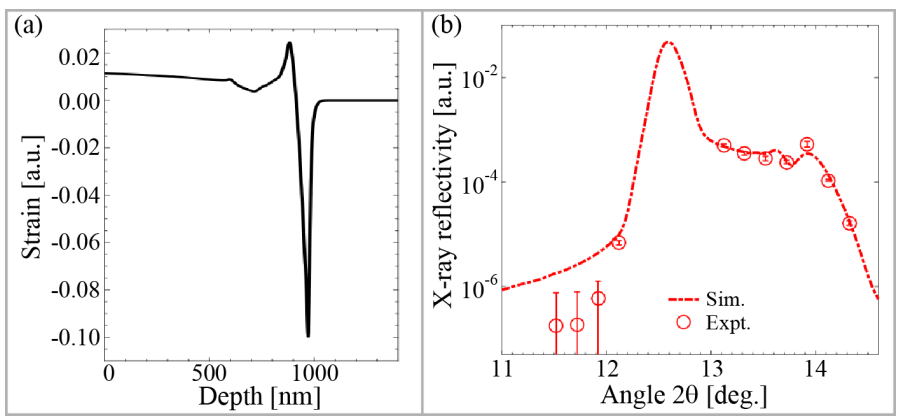

Figure 5.11: (a) Strain profile in InSb at a delay of 300 ps. (b) Experimental and simulated X-ray reflectivity.

The strain profile can be extracted from the mass density, as described in Section 4.2. The thickness of the Al film in this experiment was 300 nm. The strain profile ($\sigma(z,t)$) at 300 nm in the Al film was extracted from the mass density using the relation: $\sigma(z,t) = \rho_{Al,s}/\rho_{Al}(z,t) - 1$, where $\rho_{Al,s}$ is the tabulated solid density of Al and $\rho_{Al}(z,t)$ is the density calculated with the ESTHER code. This strain profile will be transmitted into the InSb substrate, where it will propagate at the speed of sound (3900 m/s). Figure 5.11(a) shows the strain profile in the InSb substrate at a time delay of 300 ps after laser excitation. The sharp peak has an amplitude of -10% and a duration of 25 ps. In order to compare this with the experimental measurements shown in Figure 5.9, the strain profile in Figure 5.11(a) was imported to the Stepanov X-ray server [113] to simulate the dynamic X-ray reflectivity of InSb. Figure 5.11(b) shows the experimental measurements and the simulated X-ray reflectivity of InSb at a delay of 300 ps. It can be seen that the simulation is in good agreement with the experimental data. This means a strain with an amplitude of -10% was generated

in this experiment. The pressure can be extracted from the strain amplitude and the bulk modulus of InSb M_{InSb} (50 GPa) [114], using the relation: $P = \sigma \times M_{InSb}$, giving a value of 5 GPa.

To characterize the transient nature of the pressure wave, the X-ray reflectivity of the InSb substrate was measured at a fixed angle of incidence ($\theta = 6.85°$) at different delays. Figure 5.12 shows the X-ray reflectivity of the InSb substrate at different time delays with laser excitation, and the reference reflectivity without laser excitation. It can be seen that the decay of the X-ray reflectivity is exponential, with a width of 500 ps. This width can also be calculated from the probing depth of the X-rays and the speed of sound in InSb. At $\theta = 6.85°$, the probing depth of the X-rays is 2300 nm for a photon energy of 15 keV. Based on the speed of sound in InSb, which is 3900 m/s, the pressure wave will propagate through the probing area of the X-rays after ~600 ps, which is in good agreement with the experimental data.

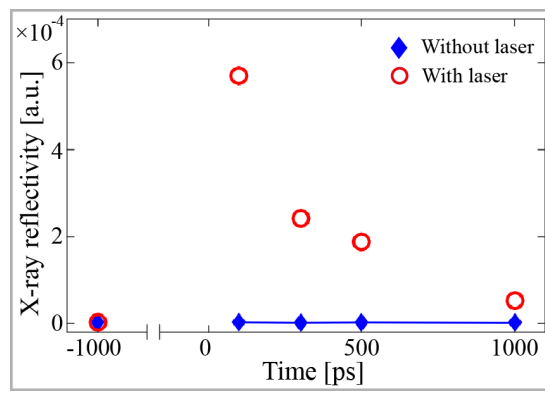

Figure 5.12: Evolution of X-ray reflectivity of the InSb substrate at $\theta = 6.85°$.

It has been theoretically predicted that, under the pressure created (5 GPa), phase transition could occur from InSb I to InSb III [115]. These two structures are shown in Figure 5.13. X-ray diffraction patterns were obtained during this experiment in an attempt to determine whether a phase transition had occurred. However, the photon flux was low and the S/N ratio was poor, and no evidence was seen of a phase transition in the time-resolved measurements.

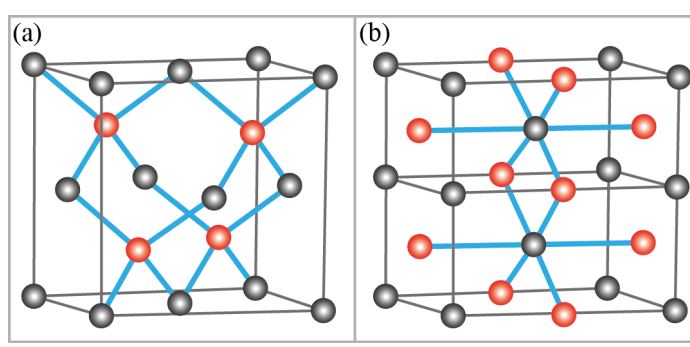

Figure 5.13: Crystal structures of InSb I (a) and InSb III (b).

Our group has since obtained beamtime at the LCLS, which provides a photon flux 3–4 orders higher, making it possible to investigate structural changes in real time. Data analysis is ongoing.

5.4 Pressure waves generated in graphite

Direct melting of InSb has shown that the amplitude of the transient strain wave is 2% [38], which corresponds to a pressure of 1 GPa. This is smaller than the pressure of 5 GPa generated in the Al/InSb transducer. However, it shows that it is possible to generate large pressure waves in materials without using transducer structures. This section describes the generation of a pressure wave in graphite (Paper V). This experiment was performed in non-coplanar geometry in order to fulfil the Bragg condition at a given X-ray angle of incidence. Figure 5.14 shows a schematic of the experimental setup.

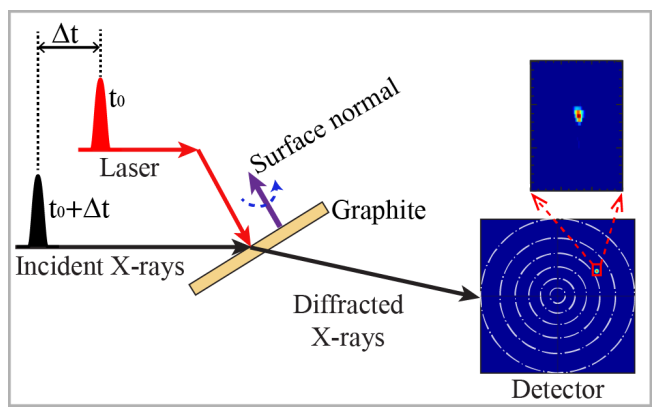

Figure 5.14: Schematic of the experimental setup used to measure the pressure wave generated in graphite.

The sample was a natural graphite crystal with a thickness of 20 μm. The crystal was mounted on a rotation stage to allow azimuth rotation around the surface normal. The laser beam had a central wavelength of 800 nm and a pulse duration of 1.2 ps, and normal incidence was used. The lattice dynamics of the graphite crystal after laser excitation was probed with an X-ray beam with a photon energy of 15 keV and a pulse duration of 100 ps. The angle of incidence of the X-ray beam was 12°. The diffracted X-rays were captured with a 2D detector at a distance of 78 cm from the sample. At this distance, the detector can cover a q range of 1–6 Å^{-1}, indicated by the white dot-dashed circles in Figure 5.14.

During this experiment, the intensity of the X-rays diffracted from the (103) crystalline plane of graphite, indicated by the red rectangle in Figure 5.14, was compared before and after laser excitation. Figure 5.15(a) shows the reference intensity and position of the static (103) reflection. The diffracted intensity increased significantly between 33 mm and 35 mm along the vertical position of the detector 200 ps after laser excitation, as can be seen in Figure 5.15(b). The laser-induced increase in intensity appeared above the static (103) reflection position, which corresponds to higher q

range in Figure 5.14. According to the definition of the q value in Eq. 4.3 and Bragg's law, a higher value of q corresponds to a larger scattering angle θ, and thus smaller d spacing of the crystal lattice. The increase in the diffracted intensity seen in Figure 5.15(b) therefore indicates that the graphite lattice was compressed as a result of laser excitation.

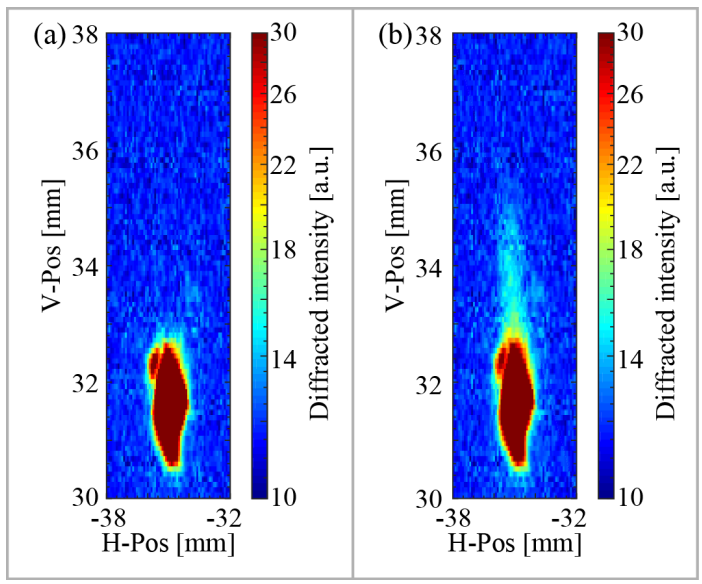

Figure 5.15: X-ray diffraction patterns obtained from a natural graphite crystal before laser excitation (a) and 200 ps after laser excitation (b).

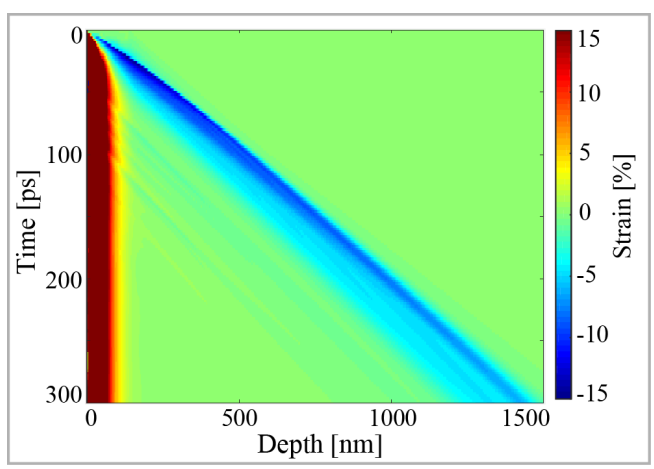

Figure 5.16: Evolution of strain in graphite with a laser fluence of 300 mJ/cm2^2.

Every position within the area of increased intensity in Figure 5.15(b) corresponds to a specific d spacing, and thus a specific strain. The hydrodynamic model was used to simulate the strain evolution as a function of time and depth, in order to investigate

the profile of the laser-induced strain in the graphite sample. Figure 5.16 shows the strain map calculated with the ESTHER code. It can be seen that the strain in the upper layer (∼80 nm, red shaded area) is greater than 10%, which is due to melting of the surface layer. The blue shaded area in Figure 5.16 represents negative strain, which means compression of the graphite lattice. The generation of compressive strain is associated with the melting of the surface layer. During the first 40 ps after laser excitation, the melting depth increased gradually, and the width of the compressive strain became broader. After 40 ps, the expansive strain remained in the surface layer while the compressive strain propagated into the crystal lattice. The compressive strain pulse reached a depth of ∼1500 nm within 300 ps.

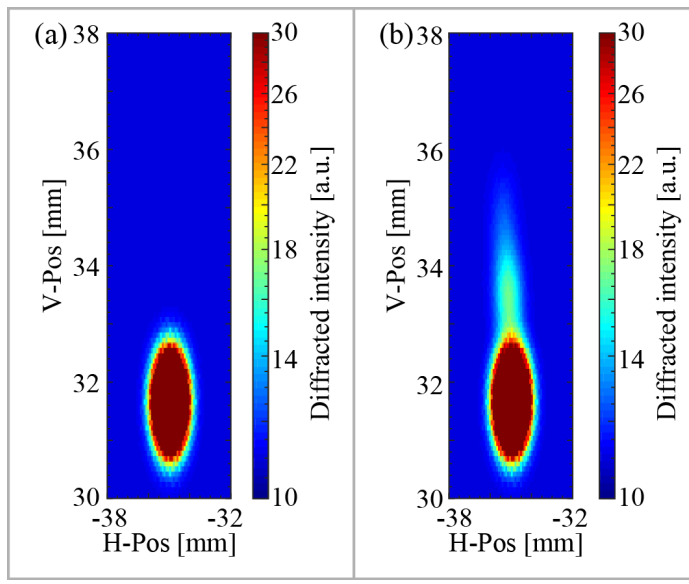

Figure 5.17: Simulated X-ray diffraction patterns using the strain profile from hydrodynamic calculations: (a) before laser excitation, (b) 200 ps after laser excitation.

The diffraction code discussed in Section 4.3 can be used to study the strained crystal lattice. The strain map obtained from the hydrodynamic simulation was imported into the diffraction code to reproduce the intensity of the diffracted X-rays. Figure 5.17 shows the simulated X-ray diffraction patterns for reflection from the graphite (103) plane. The reference diffracted intensity without laser excitation is shown in Figure 5.17(a), and the diffracted intensity at a time delay of 200 ps, calculated with the diffraction code, is shown in Figure 5.17(b). In this experiment, the pulse duration of the X-rays was 100 ps, which means that the X-ray pulse probed the overall crystal response to the propagating strain wave. Therefore, the simulated diffraction pattern in Figure 5.17(b) was calculated by importing strain profiles obtained at different time delays into the diffraction code with a weighting factor that was proportional to the amplitude of the X-ray pulse at the corresponding time. It can be seen that the simulated results are in good agreement with the experimental diffraction pattern.

It can be seen from Figure 5.15(b) and Figure 5.17(b) that the diffracted intensity, which is related to the compressive strain, is much weaker than that of the static

(103) reflection. This is because the thickness of the strained layers is smaller than that of the unperturbed layers. The thickness of the graphite crystal was 20 μm, and it can be seen in Figure 5.16 that the width of the compressive strain, which is the thickness of the strained layers, is on the order of hundreds of nm. Therefore, the dominating contribution to the diffracted intensity in the raw diffraction images is from the unperturbed graphite lattice.

In order to visualize the laser-induced compressive strain with better contrast, the X-ray diffraction image obtained before laser excitation was subtracted from the diffraction image acquired after laser excitation. Figure 5.18 shows the difference images of the diffracted intensity, 100 ps and 200 ps after laser excitation. Figure 5.18(a) and 5.18(c) show the images obtained by the subtraction of experimental results, while the corresponding simulated images are shown in Figure 5.18(b) and 5.18(d). The blue areas in Figure 5.18, which have a negative intensity, correspond to the static (103) reflection, as shown in Figure 5.15(a) and Figure 5.17(a). The positive intensity in Figure 5.18 is related to the compressive strain. It can be seen that the positive intensity appears further away from the static reflection in Figure 5.18(a) than it does in Figure 5.18(c). This difference is also visible in the simulated results (Figure 5.18(b) and Figure 5.18(d)). This means that the amplitude of the strain is higher at 100 ps than at 200 ps. In order to quantify the strain amplitude at different time delays, a series of dashed lines, which indicate a strain range of 0–12% along the surface normal of the graphite crystal, are included in Figure 5.18. The step size between two neighboring dashed lines is 2%.

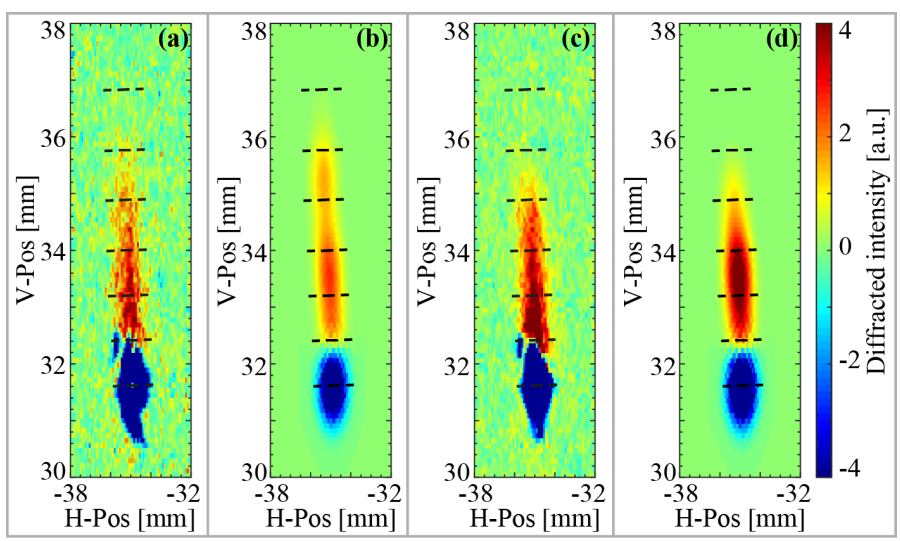

Figure 5.18: X-ray diffraction images obtained by subtracting the image obtained before laser excitation from the diffraction image acquired after laser excitation. (a) and (c) show experimental results at delays of 100 ps and 200 ps, and (b) and (d) simulated results at delays of 100 ps and 200 ps.

The amplitude of the compressive strain at 100 ps was found to be 10.0%, with an uncertainty of ±0.5%, which is related to the X-ray energy resolution. The pressure was deduced to be 7.2 GPa from the strain amplitude and the compressibility of

graphite [116]. At 200 ps after laser excitation, the amplitude of the strain had decreased to 8.5%, and the corresponding pressure was 4.8 GPa. The decrease in the amplitude of the compressive strain can also be seen in Figure 5.16. From the hydrodynamic simulation shown in Figure 5.16, it was estimated that the amplitude of the compressive strain was ∼15% at 25 ps, and decreased to ∼6% at 300 ps. The hydrodynamic simulation was calculated in steps of 2 ps, which enabled the large compressive strain (∼15%) at early time delays (25 ps) to be resolved. The X-ray pulse used in this experiment had a pulse duration of 100 ps, and thus probed the overall evolution of the strain pulse. Shorter X-ray pulses will be needed to investigate the early evolution of the graphite lattice after laser excitation.

5.5 Non-thermal melting of InSb

The probing depths in the two experiments described above were chosen to be on the order of few μm or even more, in order to investigate the propagation of pressure waves. This section describes the ultrafast melting of InSb. If a sufficient proportion (10% or more) of the electrons is excited from the valence band to the conduction band in semiconductors, non-thermal melting can occur on the time scale of few hundred femtoseconds [33–36]. In order to match the melting depth, the probing depth should be much smaller (tens of nm) than those used in the experiments described in Sections 5.3 and 5.4.

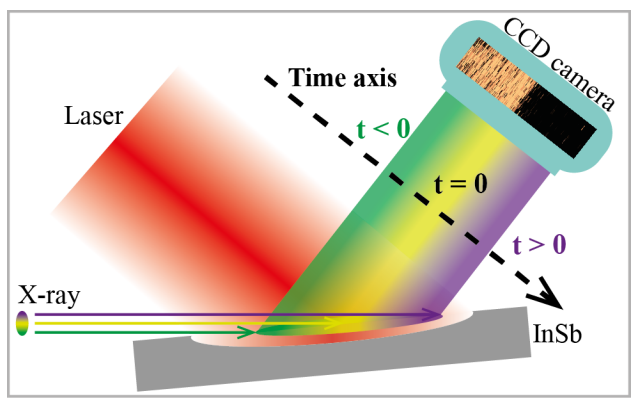

Figure 5.19: Schematic of the experimental setup used to study non-thermal melting in InSb.

Figure 5.19 shows the experimental setup used in the non-thermal melting experiment. Since the probing depth of the X-rays is related to the angle of incidence, the grazing incident geometry was used for the X-ray beam in this experiment to ensure a small probing depth. The photon energy of the X-rays was 3.56 keV with a bandwidth of 4×10^{-4}. The angle of incidence was set to 0.75°, and the resulting probing depth was 28 nm. The pulse duration of the X-rays was 100 fs. The InSb sample was excited by a laser beam with a pulse duration of 40 fs, a central wavelength of 800 nm, and an angle of incidence of 45°. The intensity of the X-rays diffracted from the (111) plane in InSb was captured with a CCD camera. Different parts of the X-ray beam probe different parts of the sample with specific time delays after laser excitation, due to

differences in the propagation time (as illustrated by the colors in Figure 5.19). For instance, the green shaded part of the X-ray beam arrives at the sample earlier than the laser beam, which means this part of the X-ray beam probes the sample response before laser excitation ($t < 0$), while the purple shaded part of the X-ray beam records the lattice dynamics after laser excitation ($t > 0$). The time axis is represented by the dashed black arrow. The position on the CCD camera along the time axis can be converted into time using a coefficient of 14.6 fs/px, which was calculated from the geometry of the experiment.

The X-ray diffraction patterns from the InSb sample are shown in Figure 5.20, where each image was obtained from the average of 10 measurements. The horizontal axis in Figure 5.20 corresponds to the time axis in Figure 5.19, and has been converted into time. The reference image (Figure 5.20(a)) shows the intensity of the diffracted X-rays without laser excitation, while Figure 5.20(b) shows the results with laser excitation. The diffracted intensity in Figure 5.20(b) is similar to that in Figure 5.20(a) before time 0, after which it decreases, indicating disordering of the InSb crystal lattice. The lineout of the X-ray diffraction efficiency, shown in Figure 5.20(c), was obtained from the ratio of the diffracted intensity with laser excitation and without laser excitation.

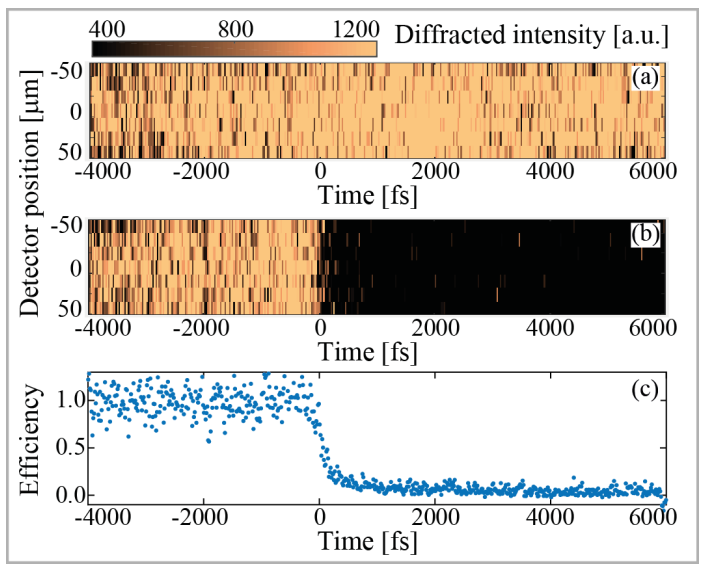

Figure 5.20: X-ray diffraction patterns: (a) without laser excitation, (b) with laser excitation. The ratio of the diffracted intensity with laser excitation and without laser excitation is in (c).

To investigate the lattice dynamics during melting, the lineout was selected within a shorter time window (−1000 fs to 2000 fs), and is shown in Figure 5.21. The Debye-Waller model was used to interpret the evolution of the diffraction efficiency in this experiment. This model describes the relation between the scattering intensity of the X-rays and the averaged mean-square displacement of the atoms in the crystal lattice:

$$I = \mathrm{e}^{-2W} = \mathrm{e}^{-Q^2 \cdot \langle u^2 \rangle / 3} \tag{5.2}$$

where W is the Debye-Waller factor, Q is the magnitude of the reciprocal vector of the (hkl) reflection, and $< u^2 >$ is the averaged mean-square displacement of the atoms. In this experiment, the InSb (111) reflection was studied, therefore $Q_{111} = 2 \cdot \pi / d_{111} = 1.680$ Å^{-1}. Equation 5.2 states how the diffracted intensity of a Bragg reflection (hkl) decreases when the atoms deviate from their equilibrium positions in the crystal lattice. It should be noted that I denotes the normalized intensity in Eq. 5.2, which is the same as the X-ray diffraction efficiency. The X-ray diffraction efficiency for different averaged root-mean-square displacements ($\sqrt{< u^2 >}$) for the InSb (111) reflection is given in Table 5.2.

Table 5.2: X-ray diffraction efficiency for different values of the averaged root-mean-square displacement ($\sqrt{< u^2 >}$) for the InSb (111) reflection.

Efficiency	100%	90%	60%	40%	20%
$\sqrt{< u^2 >}$ [Å]	0.0	0.3	0.7	1.0	1.3

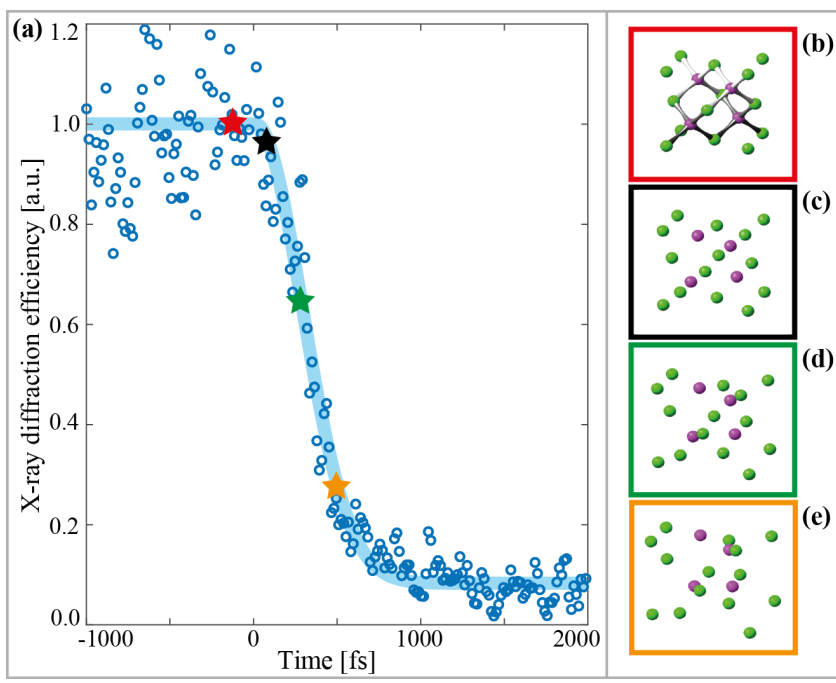

Figure 5.21: (a) TRXD efficiency obtained from an InSb crystal. The experimental data are shown by blue circles. The blue curve is a Gaussian fit to the experimental data, which gives a 10%–90% drop time of 450 fs. The differently colored stars represent the X-ray diffraction efficiency with different averaged root-mean-square displacements ($\sqrt{< u^2 >}$). (b)-(e) Schematic representations of the evolution of the crystal lattice corresponding to stars with different colors in (a). Indium (In) atoms are shown in green and antimony (Sb) atoms in purple.

The average mean-square displacement is found in the exponential term in Eq. 5.2,

which means that the diffraction efficiency has a Gaussian profile. Therefore, the experimental data from this experiment were fitted with a Gaussian function, as shown in Figure 5.21(a). The time scale of non-thermal melting in InSb was estimated from this fit, giving a disordering time of 450 fs, which corresponds to the time required for the 10%–90% change in the X-ray diffraction efficiency. Figure 5.21(b)-(e) shows schematic illustrations of the displacement of atoms in a unit cell of InSb for various values of the averaged root-mean-square displacement, corresponding to the stars with the same colors in Figure 5.21(a). In Figure 5.21(b) this is zero, so the diffraction efficiency is one. As the averaged root-mean-square displacement increases, the diffraction efficiency starts to decrease, as can be seen in Figure 5.21(a).

Potential application in monitoring the arrival time of X-ray pulses

The development of hard X-ray FELs has provided the opportunity to study structure dynamics in bulk materials with femtosecond time resolution [8]. However, the precision in the synchronization between the pump beam and the X-ray beams is on the order of 100 fs, due to the stochastic nature of emitted radiation [117, 118]. It is therefore difficult to determine time zero for the pump-probe experiments carried out at these large-scale X-ray facilities. Since non-thermal melting is an ultrafast response of materials, it can be used as a time stamp for pump-probe experiments.

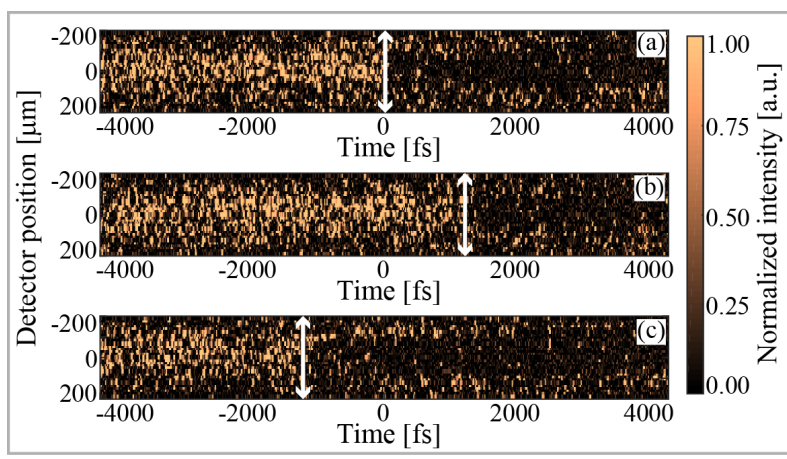

Figure 5.22: X-ray diffraction patterns acquired with three X-ray pulses with laser excitation. The white arrows represent time zero for each X-ray pulse. The nominal time axes in (b) and (c) were adjusted to the time axis in (a).

Figure 5.22 shows X-ray diffraction patterns with laser excitation. Each image was acquired with a single X-ray pulse. For easy comparison, the nominal time axes in Figure 5.22(b) and Figure 5.22(c) were adjusted to the time axis in Figure 5.22(a). The white arrows indicate time zero for each X-ray pulse. It can be seen that the arrival time of the X-rays varies from shot to shot. This variation in the X-ray arrival time is called jitter.

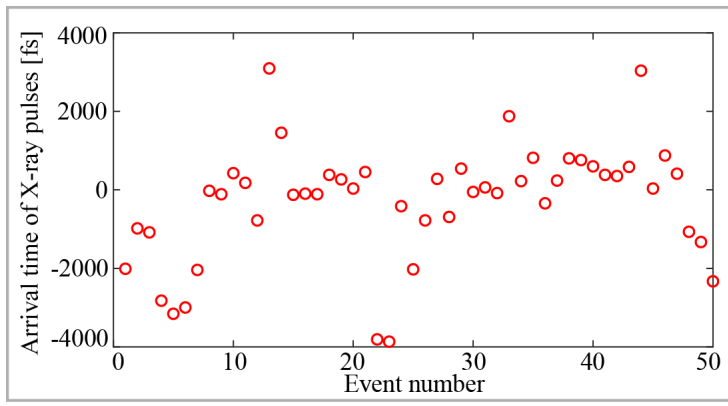

Figure 5.23: Monitoring the arrival time of X-ray pulses using non-thermal melting.

In order to investigate the jitter of the X-ray pulses, fifty non-thermal melting events were acquired, and the arrival time was extracted from the X-ray diffraction patterns. The results from these fifty measurements are shown in Figure 5.23, where it can be seen that ∼50% of the X-ray pulses arrived within −500 fs and +500 fs. Together, these fifty measurements provide an estimate of the jitter of the X-ray pulses, which is on the order of 1 ps.

Chapter 6

Summary & Outlook

6.1 Summary of this thesis

This thesis presents the main results from five experiments, in which various structural dynamics in solids were studied, ranging from lattice vibration to lattice disordering. Figure 6.1 categorizes these fives experiments in terms of laser excitation fluence and the time scale of the dynamics.

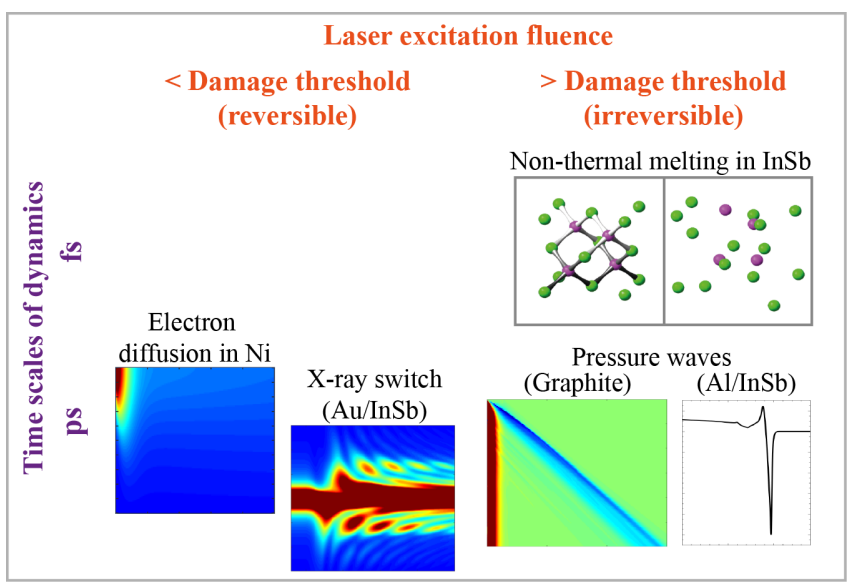

Figure 6.1: Time scales and laser excitation fluences of the experiments described in this thesis.

Electron diffusion in Ni (Paper II) and the performance of the Au/InSb switch (Paper III) were studied with a laser fluence below the damage threshold of the samples. In these two experiments, the dynamics in the samples are reversible, which means that repetitive measurements can be made. In the study of electron diffusion

in a Ni film, the electron-phonon coupling factor was characterized together with the two-temperature model simulation. This shows that TRXD can be used to characterize the basic physical properties of a metallic film. The Au/InSb switch described in Paper III allows the duration of the X-ray pulse to be reduced from 100 ps to 20 ps, which provides a potential method of generating short X-ray pulses at storage rings.

The pressure waves in an Al/InSb transducer (Paper IV) and a graphite crystal (Paper V) were studied with a laser fluence above the damage threshold of the samples. In the Al/InSb transducer, a pressure wave with an amplitude of 5 GPa, resulting from the melting of the top layer of the Al film, was generated and characterized 300 ps after laser excitation. Since the melting of the Al film is an irreversible change, this was a single-shot experiment. The amplitude of the pressure wave in the graphite sample was found to be 7.2 GPa 100 ps after laser excitation. Due to the high in-plane thermal diffusivity of graphite, thermal diffusion equilibrates the temperature laterally between two consecutive laser shots, thus multiple shots were acquired on the same position in order to improve the S/N ratio. The experiment in which non-thermal melting of InSb was studied, was also carried out in the high-fluence regime. Using the short X-ray pulses at the FemtoMAX beamline (Paper I), the atomic motion in InSb was visualized during the ultrafast melting process with a temporal resolution of 100 fs. The InSb lattice lost its crystalline structure after the laser shots, and this experiment was therefore conducted in single-shot mode. The findings of these three experiments that were carried out in the high-fluence regime extend the current knowledge on hydrodynamic pressure waves and ultrafast phase transitions in solids.

6.2 Outlook

Probing early-stage evolution of pressure waves

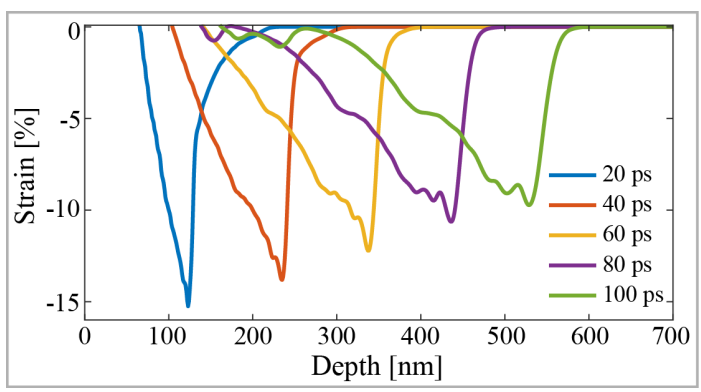

Figure 6.2: Evolution of strain waves in graphite after laser excitation with a fluence of 300 mJ/cm^2.

From the hydrodynamic simulations shown in Figure 6.2, it can be seen that the amplitude of the strain waves in graphite decreases significantly during the first 100 ps after laser excitation. However, during the experiment presented in Paper V, the duration of the X-ray pulse was not short enough to resolve the strain profiles at different time delays and to track the evolution of the strain waves during the early

stages. Therefore, it was impossible to evaluate the amplitude of the pressure waves at short time delays. Experiments should be carried out in the future with X-ray pulses shorter than 100 ps, to improve our understanding of the pressure changes at early stages after laser excitation.

Due to the low X-ray photon flux in single-shot mode, no direct evidence of phase change was found in the time-resolved measurements presented in Paper IV, despite the fact that the amplitude of the pressure pulse was in the range in which phase transition could occur. X-ray pulses with a higher photon flux will definitely help to improve the S/N ratio. Measurements have recently been carried out at the X-ray pump-probe instrument [68] at the LCLS, and analysis is ongoing.

Mapping reciprocal space & diffuse scattering

The development of TRED techniques provides a means of studying structural dynamics with femtosecond resolution on the atomic scale. Due to the high kinetic energy of the electrons (tens of keV to a few MeV), the wavelength of the electrons is on the order of a picometer, which is approximately two orders of magnitude shorter than the wavelength of the X-rays. According to Bragg's law, the Bragg angles will be smaller for shorter wavelengths, which means that electron diffraction can map a large portion of reciprocal space. This offers a unique opportunity to visualize structural changes such as ultrafast solid-liquid phase transition [16, 17] and symmetry switching with atomic-level precision [44]. Figure 6.3(a) shows the electron diffraction pattern from a graphite crystal. The phonon map can be overlaid on the diffraction image, in order to construct the Brillouin zone, which is a primitive cell in reciprocal space, around each diffraction spot, as illustrated by the white-shaded hexagons in Figure 6.3(a).

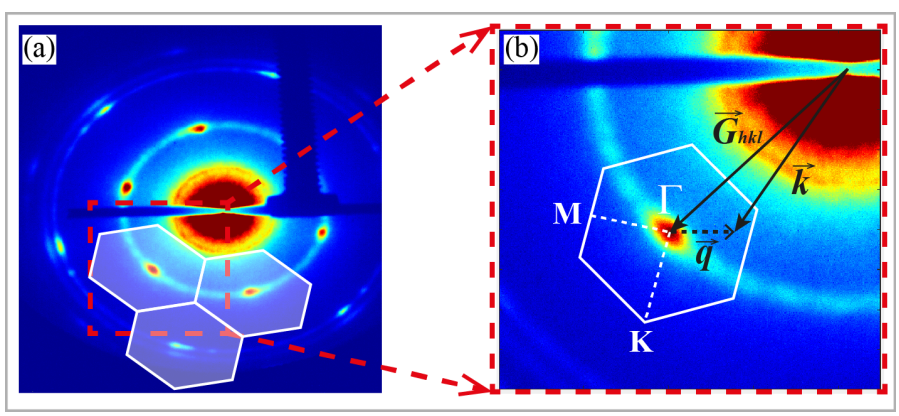

Figure 6.3: (a) Illustration of a phonon map in a graphite crystal lattice. (b) Principles of diffuse scattering. The Bragg diffraction spot is at the center of the Brillouin zone (Γ), and M and K denote the central point of the zone edge and the corner of the Brillouin zone, respectively.

Since the electron diffraction image captures a large portion of reciprocal space, it is feasible to perform diffuse scattering studies around the diffraction spots. Figure 6.3(b) illustrates the principles of diffuse scattering. $\vec{G}_{hkl}$ is the reciprocal vector of a given Bragg reflection. The diffuse scattering wave vector, which corresponds to a

phonon wave vector $\vec{q}$ around the (hkl) reflection, is denoted $\vec{k}$. The diffuse scattering around the diffraction spots provides the momentum-resolved phonon information [12]. Moreover, diffuse scattering is sensitive to the random motion of atoms, and has been used together with diffraction methods to study ultrafast disordering [119].

THz-driven structural dynamics

The structural dynamics discussed in this thesis are generally triggered by the excitation of carriers in solids. Due to the development of THz techniques, it is now possible to excite the atoms directly using the strong electric field of THz radiation [120, 121]. THz techniques have been used together with TRXD and TRED in several studies to investigate structural dynamics [44, 122, 123]. The combination of THz techniques and diffraction methods provides a new pathway for future fundamental studies on solids.

Acknowledgements

This thesis would not have been completed without the help of many people: my supervisors, my colleagues, my friends and my family.

First of all, I would like to express my sincere thanks to my main supervisor, Prof. Jörgen Larsson. Thank you for giving me the opportunity to join this wonderful ultrafast X-ray science group. I have learned a lot during the past few years; in both research and pedagogical skills. Thank you for asking me questions and helping me to think critically. Thank you for always giving me your support during my research, and for helping me to explain my research in an intuitive way. *Tack så mycket!*

Secondly, I would like to thank my co-supervisor, Dr. Henrik Enquist. You were always able to explain complex physics and experimental setups using pen and paper. Thank you so much for all your help regarding research, and for explaining so many things during daily research life; from lasers to X-rays, and from monochromators to phase shifters.

I have shared many memorable moments with the other members of our group during the past years. I will always remember the good times we spent together; from D611 to FemtoMAX, from ESRF to LCLS. At the same time, I learned a lot from you, and you gave me a lot of help. Amelie, I am so lucky to have worked with you during the first two years of my PhD. Your enthusiasm and passion for science are inspiring. Thank you for all the detailed explanations of ultrafast lasers and all our constructive conversations during our day-to-day work. Thank you also for introducing me to Gruyère de Comté, and for sharing your family recipe for Galette Charentaise. *Merci beaucoup!* Thanks Anna, for your help from my first day as a PhD student. Carl and Åsa, thanks a lot for your help during the nights of data acquisition. I also would like to thank Chien-Ming, Amit, Armand, Eric and Axel, for interesting discussions.

Part of my research was carried out at the FemtoMAX beamline at the MAX IV Laboratory. I would like to express my thanks to the beamline staff. Andrius, you are the first person I ask for help whenever I have a question about samples. Thank you for answering my numerous questions during our beamtime. Thai, thank you very much for reminding me of experimental details during the beamtime. David, thank you so much for always preparing the laser in the best possible way for our experiments.

Most of my PhD work was supported by the X-probe Innovative Training Network. I would like to thank Prof. Beatrice Vallone and the other group leaders for organizing all the meetings. I would also like to thank all the fellows; it was very nice to meet you all.

Many thanks to my colleagues at the Division of Atomic Physics. Prof. Claes-Göran Wahlström, thank you for leading the Division so well, and thank you so much for providing me with the necessary paperwork on a Friday afternoon, so that I could get my visa three days before our beamtime started. Anne, thank you for answering all my questions concerning administrative matters. Jakob, thank you for your help with the invoices. Åke, thank you very much for all your help; from computers to soldering. I also appreciate the help of Anders, Per, Isabel, Lana, Lovisa, Adam, Samuel, Jan, Sylvain, Hampus, Filippo.

我想感谢几位工作中的同事。郭辰，谢谢你分享给我的中文包，让我可以在论文中写中文，还要谢谢你在工作中的帮忙。佑辰，谢谢你给我的机械软件十五分钟新手快速入门教程，让我可以有一个相对容易的开端并且能够循序渐进地自学，还要谢谢你分享给我的毕业流程，让我可以按部就班地准备毕业答辩。春艳，谢谢你耐心地阅读我毕业论文的第一版手稿并且提出详细的建议，这些反馈帮助我把论文写得更加有条理。李倩，谢谢你的帮忙，无论是在隆德还是在斯德哥尔摩。

我想感谢几位生活中的朋友。马爽，很幸运在二十五年前认识你这位挚友，我可以随意地和你聊学习，聊工作，从生活琐碎到愿望理想。夏雪，静茹，谢谢你们一直以来对我的鼓励与支持。荆丽，你是一位可以从量子分子聊到电视电影的同学兼好友。海丽，谢谢你回答我关于签证的相关问题以及准备相关材料的提醒，谢谢你给我的关于面签的建议和注意事项。毛毛，谢谢你帮我找到了需要的文献，还要谢谢你从凝聚态理论的角度给我的科普总结所提的意见。师姐，杜娥，谢谢你们平时的温暖问候。

最后，我想感谢我的家人。爸爸妈妈，谢谢你们总是耐心安静地听我诉说工作和学习方面的琐事，总是不断地叮嘱我注意身体，也谢谢你们平时把自己照顾得好好的，让我可以安心地工作。爸爸，您的幽默，妈妈，您的温和，总能轻而易举地带走我工作中的疲惫与烦忧。姐姐，谢谢你的关心与叮咛，也谢谢你分享给我的那些生活中的小窍门。丽焕姐，谢谢你对我的照顾以及平日里的温馨问候。因着你们无微不至的关怀，我才能够怀着一颗平常心在科研的道路上踏实前行。

References

1. L. E. Hargrove, R. L. Fork, and M. A. Pollack. Locking of He-Ne laser modes induced by synchronous intracavity modulation. *Appl. Phys. Lett.*, 5(1):4–5, 1964.

2. D. Strickland and G. Mourou. Compression of amplified chirped optical pulses. *Opt. Commun.*, 55(6):447–449, 1985.

3. C. Danson, D. Hillier, N. Hopps, and D. Neely. Petawatt class lasers worldwide. *High Power Laser Sci. Eng.*, 3(e3), 2015.

4. B. Rethfeld, K. Sokolowski-Tinten, D. Von Der Linde, and S. I. Anisimov. Timescales in the response of materials to femtosecond laser excitation. *Appl. Phys. A*, 79(4-6):767–769, 2004.

5. S. K. Sundaram and E. Mazur. Inducing and probing non-thermal transitions in semiconductors using femtosecond laser pulses. *Nat. Mater.*, 1(4):217–224, 2002.

6. K. J. Gaffney and H. N. Chapman. Imaging atomic structure and dynamics with ultrafast X-ray scattering. *Science*, 316(5830):1444–1448, 2007.

7. M. Chergui and A. H. Zewail. Electron and X-ray methods of ultrafast structural dynamics: Advances and applications. *ChemPhysChem*, 10(1):28–43, 2009.

8. A. M. Lindenberg, S. L. Johnson, and D. A. Reis. Visualization of atomic-scale motions in materials via femtosecond X-ray scattering techniques. *Annu. Rev. Mater. Res.*, 47:425–449, 2017.

9. M. Harb, A. Jurgilaitis, H. Enquist, et al. Picosecond dynamics of laser-induced strain in graphite. *Phys. Rev. B*, 84(4):045435, 2011.

10. R. P. Chatelain, V. R. Morrison, B. L. M. Klarenaar, and B. J. Siwick. Coherent and incoherent electron-phonon coupling in graphite observed with radio-frequency compressed ultrafast electron diffraction. *Phys. Rev. Lett.*, 113(23):235502, 2014.

11. M. Harb, H. Enquist, A. Jurgilaitis, et al. Phonon-phonon interactions in photoexcited graphite studied by ultrafast electron diffraction. *Phys. Rev. B*, 93(10):104104, 2016.

12. M. J. Stern, L. P. René de Cotret, M. R. Otto, et al. Mapping momentum-dependent electron-phonon coupling and nonequilibrium phonon dynamics with ultrafast electron diffuse scattering. *Phys. Rev. B*, 97(16):165416, 2018.

13. L. Wirtz and A. Rubio. The phonon dispersion of graphite revisited. *Solid State Commun.*, 131(3-4):141–152, 2004.

14. K. Sokolowski-Tinten, J. Bialkowski, M. Boing, et al. Thermal and nonthermal melting of gallium arsenide after femtosecond laser excitation. *Phys. Rev. B*, 58(18):R11805–R11808, 1998.

15. B. Rethfeld, K. Sokolowski-Tinten, D. Von der Linde, and S. I. Anisimov. Ultrafast thermal melting of laser-excited solids by homogeneous nucleation. *Phys. Rev. B*, 65(9):092103, 2002.

16. B. J. Siwick, J. R. Dwyer, R. E. Jordan, and R. J. D. Miller. An atomic-level view of melting using femtosecond electron diffraction. *Science*, 302(5649):1382–1385, 2003.

17. M. Z. Mo, Z. Chen, R. K. Li, et al. Heterogeneous to homogeneous melting transition visualized with ultrafast electron diffraction. *Science*, 360(6396):1451–1455, 2018.

18. P. Stampfli and K. H. Bennemann. Time dependence of the laser-induced femtosecond lattice instability of Si and GaAs: Role of longitudinal optical distortions. *Phys. Rev. B*, 49(11):7299–7305, 1994.

19. A. Rousse, C. Rischel, S. Fourmaux, et al. Non-thermal melting in semiconductors measured at femtosecond resolution. *Nature*, 410(6824):65–68, 2001.

20. B. L. Henke, E. M. Gullikson, and J. C. Davis. X-ray interactions: photoabsorption, scattering, transmission, and reflection at E = 50–30000 eV, Z = 1–92. *At. Data Nucl. Data Tables*, 54(2):181–342, 1993.

21. P. B. Johnson and R. W. Christy. Optical constants of transition metals: Ti, V, Cr, Mn, Fe, Co, Ni, and Pd. *Phys. Rev. B*, 9(12):5056–5070, 1974.

22. K. M. McPeak, S. V. Jayanti, S. J. P. Kress, et al. Plasmonic films can easily be better: rules and recipes. *ACS Photonics*, 2(3):326–333, 2015.

23. D. E. Aspnes and A. A. Studna. Dielectric functions and optical parameters of Si, Ge, GaP, GaAs, GaSb, InP, InAs, and InSb from 1.5 to 6.0 eV. *Phys. Rev. B*, 27(2):985–1009, 1983.

24. A. B. Djurišić and E. H. Li. Optical properties of graphite. *J. Appl. Phys.*, 85(10):7404–7410, 1999.

25. D. Attwood and A. Sakdinawat. *X-rays and extreme ultraviolet radiation: principles and applications*. Cambridge university press, 2017.

26. B. E. Warren. *X-ray Diffraction*. Courier Corporation, 1969.

27. International Union of Crystallography. *International tables for X-ray crystallography*, volume 2. Kynock Press, 1959.

28. C. Thomsen, H. T. Grahn, H. J. Maris, and J. Tauc. Surface generation and detection of phonons by picosecond light pulses. *Phys. Rev. B*, 34(6):4129–4138, 1986.

29. C. Thomsen, J. Strait, Z. Vardeny, et al. Coherent phonon generation and detection by picosecond light pulses. *Phys. Rev. Lett.*, 53(10):989–992, 1984.

30. N. Medvedev, Z. Li, and B. Ziaja. Thermal and nonthermal melting of silicon under femtosecond X-ray irradiation. *Phys. Rev. B*, 91(5):054113, 2015.

31. E. S. Zijlstra, J. Walkenhorst, and M. E. Garcia. Anharmonic noninertial lattice dynamics during ultrafast nonthermal melting of InSb. *Phys. Rev. Lett.*, 101(13):135701, 2008.

32. E. S. Zijlstra, J. Walkenhorst, C. Gilfert, et al. Ab initio description of the first stages of laser-induced ultra-fast nonthermal melting of InSb. *Appl. Phys. B*, 93(4):743–747, 2008.

33. I. L. Shumay and U. Höfer. Phase transformations of an InSb surface induced by strong femtosecond laser pulses. *Phys. Rev. B*, 53(23):15878–15884, 1996.

34. K. J. Gaffney, A. M. Lindenberg, J. Larsson, et al. Observation of structural anisotropy and the onset of liquidlike motion during the nonthermal melting of InSb. *Phys. Rev. Lett.*, 95(12):125701, 2005.

35. A. M. Lindenberg, J. Larsson, K. Sokolowski-Tinten, et al. Atomic-scale visualization of inertial dynamics. *Science*, 308(5720):392–395, 2005.

36. P. B. Hillyard, K. J. Gaffney, A. M. Lindenberg, et al. Carrier-density-dependent lattice stability in InSb. *Phys. Rev. Lett.*, 98(12):125501, 2007.

37. K. Sokolowski-Tinten, C. Blome, C. Dietrich, et al. Femtosecond X-ray measurement of ultrafast melting and large acoustic transients. *Phys. Rev. Lett.*, 87(22):225701, 2001.

38. H. Enquist, H. Navirian, T. N. Hansen, et al. Large acoustic transients induced by nonthermal melting of InSb. *Phys. Rev. Lett.*, 98(22):225502, 2007.

39. M. Sharma, M. K. Sanyal, I. Farrer, et al. Density dependent composition of InAs quantum dots extracted from grazing incidence X-ray diffraction measurements. *Sci. Rep.*, 5:15732, 2015.

40. Y. Soldo-Olivier, M. De Santis, W. Liang, and E. Sibert. Growth mechanisms of Pd nanofilms electrodeposited onto Au (111): an in situ grazing incidence X-ray diffraction study. *Phys. Chem. Chem. Phys.*, 18(4):2830–2839, 2016.

41. J. Schlipf and P. Müller-Buschbaum. Structure of organometal halide perovskite films as determined with grazing-incidence X-ray scattering methods. *Adv. Energy Mater.*, 7(16):1700131, 2017.

42. D. H. Reitze, X. Wang, H. Ahn, and M. C. Downer. Femtosecond laser melting of graphite. *Phys. Rev. B*, 40(17):11986–11989, 1989.

43. H. T. Lemke, C. Bressler, L. X. Chen, et al. Femtosecond X-ray absorption spectroscopy at a hard X-ray free electron laser: application to spin crossover dynamics. *J. Phys. Chem. A*, 117(4):735–740, 2013.

44. E. J. Sie, C. M. Nyby, C. D. Pemmaraju, et al. An ultrafast symmetry switch in a Weyl semimetal. *Nature*, 565(7737):61–66, 2019.

45. N. L. Wagner, E. A. Gibson, T. Popmintchev, et al. Self-compression of ultrashort pulses through ionization-induced spatiotemporal reshaping. *Phys. Rev. Lett.*, 93(17):173902, 2004.

46. D. M. Gaudiosi, A. L. Lytle, P. Kohl, et al. 11-W average power Ti:sapphire amplifier system using downchirped pulse amplification. *Opt. Lett.*, 29(22):2665–2667, 2004.

47. W. Ackermann, G. Asova, V. Ayvazyan, et al. Operation of a free-electron laser from the extreme ultraviolet to the water window. *Nat. Photon.*, 1(6):336–342, 2007.

48. J. Weisshaupt, V. Juvé, M. Holtz, et al. High-brightness table-top hard X-ray source driven by sub-100-femtosecond mid-infrared pulses. *Nat. Photon.*, 8(12):927–930, 2014.

49. M. Bargheer, N. Zhavoronkov, Y. Gritsai, et al. Coherent atomic motions in a nanostructure studied by femtosecond X-ray diffraction. *Science*, 306(5702):1771–1773, 2004.

50. G. Korn, A. Thoss, H. Stiel, et al. Ultrashort 1-kHz laser plasma hard X-ray source. *Opt. Lett.*, 27(10):866–868, 2002.

51. N. Zhavoronkov, Y. Gritsai, G. Korn, and T. Elsaesser. Ultra-short efficient laser-driven hard X-ray source operated at a kHz repetition rate. *Appl. Phys. B*, 79(6):663–667, 2004.

52. F. Zamponi, Z. Ansari, C. von Korff Schmising, et al. Femtosecond hard X-ray plasma sources with a kilohertz repetition rate. *Appl. Phys. A*, 96(1):51–58, 2009.

53. U. Shymanovich, M. Nicoul, W. Lu, et al. Coherent acoustic and optical phonons in laser-excited solids studied by ultrafast time-resolved X-ray diffraction. In *AIP Conference Proceedings*, volume 1278, pages 558–566. AIP, 2010.

54. M. Woerner, C. von Korff Schmising, M. Bargheer, et al. Ultrafast structural dynamics of perovskite superlattices. *Appl. Phys. A*, 96(1):83–90, 2009.

55. D. Schick, A. Bojahr, M. Herzog, et al. Normalization schemes for ultrafast X-ray diffraction using a table-top laser-driven plasma source. *Rev. Sci. Instrum.*, 83(2):025104, 2012.

56. D. Schick, R. Shayduk, A. Bojahr, et al. Ultrafast reciprocal-space mapping with a convergent beam. *J. Appl. Cryst.*, 46(5):1372–1377, 2013.

57. L. Miaja-Avila, G. C. O'Neil, J. Uhlig, et al. Laser plasma X-ray source for ultrafast time-resolved X-ray absorption spectroscopy. *Struct. Dyn.*, 2(2):024301, 2015.

58. E. J. Jaeschke, S. Khan, J. R. Schneider, and J. B. Hastings. *Synchrotron Light Sources and Free-electron Lasers: Accelerator Physics, Instrumentation and Science Applications*. Springer, 2016.

59. T. A. Ezquerra, M. C. Garcia-Gutierrez, A. Nogales, and M. Gomez. *Applications of synchrotron light to scattering and diffraction in materials and life sciences*, volume 776. Springer, 2009.

60. P. Willmott. *An introduction to synchrotron radiation: techniques and applications*. John Wiley & Sons, 2011.

61. S. Mobilio, F. Boscherini, and C. Meneghini. *Synchrotron Radiation*. Springer, 2016.

62. J. A. Clarke. *The science and technology of undulators and wigglers*, volume 4. Oxford University Press on Demand, 2004.

63. F. Schotte, M. Lim, T. A. Jackson, et al. Watching a protein as it functions with 150-ps time-resolved X-ray crystallography. *Science*, 300(5627):1944–1947, 2003.

64. D. A. Walko, B. W. Adams, G. Doumy, et al. Developments in time-resolved X-ray research at APS beamline 7ID. In *AIP Conference Proceedings*, volume 1741, page 030048. AIP Publishing, 2016.

65. R. Kersevan. Status of the ESRF vacuum system. In *Proceedingf of European Particle Accelerator Conference*, volume 98, pages 2178–2180, 1998.

66. J. M. Filhol, L. Hardy, and U. Weinrich. Status report of the ESRF. In *Proceedings of the 1999 Particle Accelerator Conference*, volume 4, pages 2334–2336. IEEE, 1999.

67. P. Emma, R. Akre, J. Arthur, et al. First lasing and operation of an ångstrom-wavelength free-electron laser. *Nat. Photon.*, 4(9):641–647, 2010.

68. M. Chollet, R. Alonso-Mori, M. Cammarata, et al. The X-ray pump–probe instrument at the linac coherent light source. *J. Synchrotron Rad.*, 22(3):503–507, 2015.

69. C. J. Milne, T. Schietinger, M. Aiba, et al. SwissFEL: The Swiss X-ray free electron laser. *Appl. Sci.*, 7(7):720, 2017.

70. G. Margaritondo and P. R. Ribic. A simplified description of X-ray free-electron lasers. *J. Synchrotron Rad.*, 18(2):101–108, 2011.

71. M. Yabashi, H. Tanaka, and T. Ishikawa. Overview of the SACLA facility. *J. Synchrotron Rad.*, 22(3):477–484, 2015.

72. L. Bentson, P. Bolton, E. Bong, et al. FEL research and development at the SLAC sub-picosecond photon source, SPPS. *Nucl. Instrum. Methods Phys. Res., Sect. A*, 507(1-2):205–209, 2003.

73. S. Werin, S. Thorin, M. Eriksson, and J. Larsson. Short pulse facility for MAX-lab. *Nucl. Instrum. Methods Phys. Res., Sect. A*, 601(1-2):98–107, 2009.

74. S. Thorin, D. Angal-Kalinin, M. Eriksson, et al. Bunch compression by linearising achromats for the MAX IV injector. In *International Free Electron Laser Conference*, pages 471–474, 2010.

75. I. P. S. Martin, G. Rehm, C. Thomas, and R. Bartolini. Experience with low-alpha lattices at the Diamond Light Source. *Phys. Rev. ST Accel. Beams*, 14(4):040705, 2011.

76. X. Huang, J. Safranek, J. Corbett, et al. Low alpha mode for SPEAR3. In *Proceedings of the 2007 Particle Accelerator Conference*, pages 1308–1310. IEEE, 2007.

77. M. A. Tordeux, J. Barros, A. Bence, et al. Low-alpha operation for the SOLEIL storage ring. In *Proceedings of International Particle Accelerator Conference*, pages 1608–1610, 2012.

78. S. Khan. Femtoslicing in storage rings. In *Proceedings of the 2005 Particle Accelerator Conference*, pages 590–594. IEEE, 2005.

79. R. W. Schoenlein, S. Chattopadhyay, H. H. W. Chong, et al. Generation of femtosecond pulses of synchrotron radiation. *Science*, 287(5461):2237–2240, 2000.

80. P. Beaud, S. L. Johnson, A. Streun, et al. Spatiotemporal stability of a femtosecond hard–X-ray undulator source studied by control of coherent optical phonons. *Phys. Rev. Lett.*, 99(17):174801, 2007.

81. S. Khan, K. Holldack, T. Kachel, et al. Femtosecond undulator radiation from sliced electron bunches. *Phys. Rev. Lett.*, 97(7):074801, 2006.

82. K. Holldack, J. Bahrdt, A. Balzer, et al. FemtoSpeX: a versatile optical pump–soft X-ray probe facility with 100 fs X-ray pulses of variable polarization. *J. Synchrotron Rad.*, 21(5):1090–1104, 2014.

83. M. Labat, S. Ravy, H. Abualrob, et al. Commissioning progress of the femtoslicing at SOLEIL. In *Proceedings of International Particle Accelerator Conference*, pages 206–208, 2014.

84. P. Gaal, D. Schick, M. Herzog, et al. Time-domain sampling of X-ray pulses using an ultrafast sample response. *Appl. Phys. Lett.*, 101(24):243106, 2012.

85. P. Gaal, D. Schick, M. Herzog, et al. Ultrafast switching of hard X-rays. *J. Synchrotron Rad.*, 21(2):380–385, 2014.

86. M. Sander, A. Koc, C. T. Kwamen, et al. Characterization of an ultrafast bragg-switch for shortening hard X-ray pulses. *J. Appl. Phys.*, 120(19):193101, 2016.

87. A. Loether, Y. Gao, Z. Chen, et al. Transient crystalline superlattice generated by a photoacoustic transducer. *Struct. Dyn.*, 1(2):024301, 2014.

88. C. F. McConaghy and L. W. Coleman. Picosecond X-ray streak camera. *Appl. Phys. Lett.*, 25(5):268–270, 1974.

89. J. Feng, H. J. Shin, J. R. Nasiatka, et al. An X-ray streak camera with high spatio-temporal resolution. *Appl. Phys. Lett.*, 91(13):134102, 2007.

90. J. Larsson, Z. Chang, E. Judd, et al. Ultrafast X-ray diffraction using a streak-camera detector in averaging mode. *Opt. Lett.*, 22(13):1012–1014, 1997.

91. H. Enquist, H. Navirian, R. Nüske, et al. Subpicosecond hard X-ray streak camera using single-photon counting. *Opt. Lett.*, 35(19):3219–3221, 2010.

92. M. M. Murnane, H. C. Kapteyn, and R. W. Falcone. X-ray streak camera with 2 ps response. *Appl. Phys. Lett.*, 56(20):1948–1950, 1990.

93. P. Gallant, P. Forget, F. Dorchies, et al. Characterization of a subpicosecond X-ray streak camera for ultrashort laser-produced plasmas experiments. *Rev. Sci. Instrum.*, 71(10):3627–3633, 2000.

94. U. Frühling, M. Wieland, M. Gensch, et al. Single-shot terahertz-field-driven X-ray streak camera. *Nat. Photon.*, 3(9):523–528, 2009.

95. P. B. Corkum and F. Krausz. Attosecond science. *Nat. Phys.*, 3(6):381–387, 2007.

96. T. Tschentscher, C. Bressler, J. Grünert, et al. Photon beam transport and scientific instruments at the European XFEL. *Appl. Sci.*, 7(6):592, 2017.

97. C. T. Hebeisen, G. Sciaini, M. Harb, et al. Grating enhanced ponderomotive scattering for visualization and full characterization of femtosecond electron pulses. *Opt. Express*, 16(5):3334–3341, 2008.

98. T. L. Gilton, J. P. Cowin, G. D. Kubiak, and A. V. Hamza. Intense surface photoemission: Space charge effects and self-acceleration. *J. Appl. Phys.*, 68(9):4802–4810, 1990.

99. C. T. Hebeisen, G. Sciaini, M. Harb, et al. Direct visualization of charge distributions during femtosecond laser ablation of a Si (100) surface. *Phys. Rev. B*, 78(8):081403, 2008.

100. J. G. Fujimoto, J. M. Liu, E. P. Ippen, and N. Bloembergen. Femtosecond laser interaction with metallic tungsten and nonequilibrium electron and lattice temperatures. *Phys. Rev. Lett.*, 53(19):1837–1840, 1984.

101. J. Wang and C. Guo. Ultrafast dynamics of femtosecond laser-induced periodic surface pattern formation on metals. *Appl. Phys. Lett.*, 87(25):251914, 2005.

102. D. Schick, A. Bojahr, M. Herzog, et al. udkm1Dsim – A simulation toolkit for 1D ultrafast dynamics in condensed matter. *Comput. Phys. Commun.*, 185(2):651–660, 2014.

103. D. Schick. udkm1dsim. https://github.com/dschick/udkm1Dsim. Accessed: 2016-08-19.

104. J. P. Colombier, P. Combis, R. Stoian, and E. Audouard. High shock release in ultrafast laser irradiated metals: Scenario for material ejection. *Phys. Rev. B*, 75(10):104105, 2007.

105. P. M. Leguay, A. Lévy, B. Chimier, et al. Ultrafast short-range disordering of femtosecond-laser-heated warm dense aluminum. *Phys. Rev. Lett.*, 111(24):245004, 2013.

106. J. P. Colombier, P. Combis, F. Bonneau, et al. Hydrodynamic simulations of metal ablation by femtosecond laser irradiation. *Phys. Rev. B*, 71(16):165406, 2005.

107. K. Sokolowski-Tinten, S. Kudryashov, V. Temnov, et al. Femtosecond laser-induced ablation of graphite. In *International Conference on Ultrafast Phenomena*, page ThB5. Optical Society of America, 2000.

108. M. Harb. Diffraction. https://github.com/maherharb/Diffraction. Accessed: 2017-06-23.

109. J. Červenka and C. F. J. Flipse. Structural and electronic properties of grain boundaries in graphite: planes of periodically distributed point defects. *Phys. Rev. B*, 79(19):195429, 2009.

110. T. Saito, O. Matsuda, and O. B. Wright. Picosecond acoustic phonon pulse generation in nickel and chromium. *Phys. Rev. B*, 67(20):205421, 2003.

111. C. Guo, G. Rodriguez, A. Lobad, and A. J. Taylor. Structural phase transition of aluminum induced by electronic excitation. *Phys. Rev. Lett.*, 84:4493–4496, May 2000.

112. M. Kandyla, T. Shih, and E. Mazur. Femtosecond dynamics of the laser-induced solid-to-liquid phase transition in aluminum. *Phys. Rev. B*, 75:214107, Jun 2007.

113. S. A. Stepanov. X-ray server: an online resource for simulations of X-ray diffraction and scattering. *Proc. SPIE*, 5536:16–26, 2004.

114. O. Madelung, U. Rössler, and M. Schulz, editors. *Indium antimonide (InSb) bulk modulus*. Landolt-Börnstein - Group III Condensed Matter · Volume 41A1α. Springer-Verlag Berlin Heidelberg, 2001.

115. S. C. Costa, P. S. Pizani, and J. P. Rino. Structural phase transformation in InSb: A molecular dynamics simulation. *Phys. Rev. B*, 66:214111, Dec 2002.

116. R. W. Lynch and H. G. Drickamer. Effect of high pressure on the lattice parameters of diamond, graphite, and hexagonal boron nitride. *J. Chem. Phys.*, 44(1):181–184, 1966.

117. S. W. Epp, M. Hada, Y. Zhong, et al. Time zero determination for FEL pump-probe studies based on ultrafast melting of bismuth. *Struct. Dyn.*, 4(5):054308, 2017.

118. M. Harmand, R. Coffee, M. R. Bionta, et al. Achieving few-femtosecond time-sorting at hard X-ray free-electron lasers. *Nat. Photon.*, 7(3):215–218, 2013.

119. S. Wall, S. Yang, L. Vidas, et al. Ultrafast disordering of vanadium dimers in photoexcited VO_2. *Science*, 362(6414):572–576, 2018.

120. A. Cavalleri, S. Wall, C. Simpson, et al. Tracking the motion of charges in a terahertz light field by femtosecond X-ray diffraction. *Nature*, 442(7103):664–666, 2006.

121. M. C. Hoffmann and M. E. Kozina. Terahertz-pump experiments on complex solids at X-ray FELs. In *Terahertz Emitters, Receivers, and Applications IX*, volume 10756, page 107560D. International Society for Optics and Photonics, 2018.

122. M. Kozina, T. van Driel, M. Chollet, et al. Ultrafast X-ray diffraction probe of terahertz field-driven soft mode dynamics in $SrTiO_3$. *Struct. Dyn.*, 4(5):054301, 2017.

123. M. Kozina, M. Fechner, P. Marsik, et al. Terahertz-driven phonon upconversion in $SrTiO_3$. *Nat. Phys.*, 15:387–392, 2019.

Printed by Media-Tryck, Lund 2019 NORDIC SWAN ECOLABEL 3041 0903

LUND UNIVERSITY
Faculty of Engineering, LTH
Department of Physics
Division of Atomic Physics

ISBN: 978-91-7895-125-3 (print)
ISBN: 978-91-7895-126-0 (pdf)
ISSN: 0281-2762
Lund Reports on Atomic Physics, LRAP 558 (2019)